Growth of thin Pd, Fe, Co and Ag films on A1 single crystal surfaces
by Nagarajah Rajamohan Shivaparan

A thesis submitted in partial fulfillment of the requirements for the degree of Doctor of Philosophy in Physics
Montana State University

Abstract:
The objective of this study was to investigate the formation of intermetallic compounds at the interface between surfaces of Al single crystals and various metal overlayers; also, to identify the fundamental physical parameters which determine the atomic structure of these interfaces.

The growth of thin Pd, Fe, Co and Ag films on Al(001) and Al(110) surfaces at room temperature was studied using high-energy ion scattering (HEIS), x-ray photoelectron spectroscopy (XPS) and low-energy electron diffraction (LEED). For Pd deposited on Al(110) surfaces, a strong Pd-Al mixing occurs at the Pd-Al interface. The interface mixing was observed to continue up to about 10 monolayers (ML) of Pd coverage, at which point the intermixing stops. XPS measurements of the Pd 3d photopeaks show a chemical shift that is consistent with the formation of an Pd-Al like compound at the interface and the growth of Pd metal thereafter.

Similar results were observed in the cases of Fe and Co on Al(001) and Al(110) surfaces. Deposited Fe atoms seem to intermix with the substrate Al atoms up to about 5 ML and 9 ML coverages of Fe on Al(001) and Al(001) surfaces respectively. A Volmer-Weber type growth model was used to identify the phases formed at the interfaces for both surfaces. On the other hand, Co atoms deposited on Al(001) and Al(110) surfaces. seem to displace the substrate Al atoms up to about 3ML and 5ML respectively. Based on the XPS intensity analysis we conclude that the CoAl phase was formed at the interface with near "surface" dechanneling at the interface. On the Al(001) surface, a very diffuse LEED pattern with high background intensity was observed after a deposition of 7.6 ML of Co coverage. The LEED pattern never came back on the Al(110) surface even after 15 ML of Co deposition.

In contrast to the above mentioned transition metals, Ag deposited on the Al(001) and Al(110) surface seemed to grow in an epitaxial overlayer at room temperature. XPS intensity curves and LEED strongly support the idea that the growth mode of Ag atoms on the Al(001) surface cannot be simply layer-by-layer but rather a formation of clusters of Ag atoms. On the other hand, deposited Ag atoms seem to grow layer-by-layer on the Al(110) surface.

Finally, it has been observed that the growth mode of deposited metal atoms on Al surfaces is not correctly predicted by the aluminide formation energy or the lattice mismatch. Instead, using a model for surface strain in forming the surface alloy, we found that the size of the overlayer atom compared to the substrate Al atom correlates well with the growth behavior for metals on Al surfaces.

GROWTH OF THIN Pd, Fe, Co AND Ag FILMS ON Al SINGLE CRYSTAL SURFACES

by

Nagarajah Rajamohan Shivaparan

A thesis submitted in partial fulfillment
of the requirements for the degree

of

Doctor of Philosophy

in

Physics

MONTANA STATE UNIVERSITY-BOZEMAN
Bozeman, Montana

November 1996

APPROVAL

of a thesis submitted by

Nagarajah R. Shivaparan

This thesis has been read by each member of the thesis committee, and has been found to be satisfactory regarding content, English usage, format, citations, bibliographic style, and consistency, and is ready for submission to the College of Graduate Studies.

Richard J. Smith — Richard J Smith (Signature) — 11-27-96 Date

Approved for the Department of Physics

John C. Hermanson — J Herm (Signature) — 11-27-96 Date

Approved for the College of Graduate Studies

Robert L. Brown — R L Brown (Signature) — 12/3/96 Date

STATEMENT OF PERMISSION TO USE

In presenting this thesis in partial fulfillment of the requirements for a doctoral degree at Montana State University-Bozeman, I agree that the Library shall make it available to borrowers under rules of the Library. I further agree that copying of this thesis is allowable only for scholarly purposes, consistent with "fair use" as prescribed in the U.S Copyright Law. Requests for extensive copying or reproduction of this thesis should be referred to University Microfilms International, 300 North Zeeb Road, Ann Arbor, Michigan 48106, to whom I have granted "the exclusive right to reproduce and distribute my dissertation in and from microfilm along with the non-exclusive right to reproduce and distribute my abstract in any format in whole or in part".

Signature N. R. Bly

Date 11/27/96

To my late grandfather ***Karthigesu Sinnathurai***,

and

To my **parents** and **family members**, who have given their unqualified love, understanding, and support throughout my life.....

ACKNOWLEDGEMENTS

It is my pleasure to acknowledge the persons who have helped me complete this endeavor. First and foremost, I wish to thank my adviser, Prof. Richard J. Smith, for his great care and patience, gentle nudging and nurturing, and his boundless, infectious enthusiasm. Truly, it has been "fun".

I also wish to express my sincere gratitude to Eric Anderson and Norm Williams for their patience and invaluable help in carrying out various aspects of this work. I really owe them a big one.

Special thanks go to Prof. Gerald J. Lapeyre and Asst. Prof. Lisa D. Peterson for their valuable advice and continuous assistance throughout my research.

In addition, several of my colleagues helped immeasurably. Adli A. Saleh, V. Shutthanandan, Volker Krasemann, Marcus Teter, and many others contributed in countless ways.

I gratefully acknowledge the support of the Physics Department and the National Science Foundation throughout my stay here.

Finally, to my parents, brothers, and sisters, go the greatest praise. They supported me in so many ways. Financially, emotionally, spiritually. I know it was hard to put up with my prolonged absences, both physical and mental. To them go my utmost heartfelt thanks and love.

N.R.Shivaparan, November, 1996.

TABLE OF CONTENTS

LIST OF TABLES

LIST OF FIGURES

ABSTRACT

The objective of this study was to investigate the formation of intermetallic compounds at the interface between surfaces of Al single crystals and various metal overlayers; also, to identify the fundamental physical parameters which determine the atomic structure of these interfaces.

The growth of thin Pd, Fe, Co and Ag films on Al(001) and Al(110) surfaces at room temperature was studied using high-energy ion scattering (HEIS), x-ray photoelectron spectroscopy (XPS) and low-energy electron diffraction (LEED). For Pd deposited on Al(110) surfaces, a strong Pd-Al mixing occurs at the Pd-Al interface. The interface mixing was observed to continue up to about 10 monolayers (ML) of Pd coverage, at which point the intermixing stops. XPS measurements of the Pd 3d photopeaks show a chemical shift that is consistent with the formation of an Pd-Al like compound at the interface and the growth of Pd metal thereafter.

Similar results were observed in the cases of Fe and Co on Al(001) and Al(110) surfaces. Deposited Fe atoms seem to intermix with the substrate Al atoms up to about 5 ML and 9 ML coverages of Fe on Al(001) and Al(110) surfaces respectively. A Volmer-Weber type growth model was used to identify the phases formed at the interfaces for both surfaces. On the other hand, Co atoms deposited on Al(001) and Al(110) surfaces seem to displace the substrate Al atoms up to about 3ML and 5ML respectively. Based on the XPS intensity analysis we conclude that the CoAl phase was formed at the interface with near "surface" dechanneling at the interface. On the Al(001) surface, a very diffuse LEED pattern with high background intensity was observed after a deposition of 7.6 ML of Co coverage. The LEED pattern never came back on the Al(110) surface even after 15 ML of Co deposition.

In contrast to the above mentioned transition metals, Ag deposited on the Al(001) and Al(110) surface seemed to grow in an epitaxial overlayer at room temperature. XPS intensity curves and LEED strongly support the idea that the growth mode of Ag atoms on the Al(001) surface cannot be simply layer-by-layer but rather a formation of clusters of Ag atoms. On the other hand, deposited Ag atoms seem to grow layer-by-layer on the Al(110) surface.

Finally, it has been observed that the growth mode of deposited metal atoms on Al surfaces is not correctly predicted by the aluminide formation energy or the lattice mismatch. Instead, using a model for surface strain in forming the surface alloy, we found that the size of the overlayer atom compared to the substrate Al atom correlates well with the growth behavior for metals on Al surfaces.

CHAPTER 1

INTRODUCTION

The behavior of the outer atomic layer of a surface and its interaction with atoms or molecules of adsorbates is the cornerstone of surface science. A complete understanding, at the atomic level, of these fundamental interactions would have important technological spin-offs, since they are crucial to all surface chemical reactions, catalysis and thin film nucleation[1]. It is important not only to determine the elements of species involved, but also their molecular structure and orientation. At this level, highly specific experiments are required using techniques dedicated to the full characterization of a model system, usually comprising a single crystal substrate and a well defined adsorbate species. This has become more practical with improvements in our capabilities using ultrahigh vacuum technology. Yet, we are still lacking a comprehensive model which can be used to predict the atomic structure at a metal-metal interface.

We have focused our investigations on transition-metal-aluminum (TM-Al) bilayers, and formation of transition-metal aluminides because of the technological importance of these materials. In particular, several of the TM-aluminides have potential applications as metallization layers in III-V semiconductor devices, as demonstrated recently for CoAl and NiAl on GaAs[2,3] and FeAl on InP[4]. Another technology that will benefit from studies of the TM-Al interface is concerned with the fabrication of thin-film magnets, where controlling the atomic structure could be important for designing the magnetic properties of the film. Also, thin films of transition metal aluminides may have

different physical properties than those of the bulk material since the electronic and atomic structures in the overlayer may also be modified. Palladium, for example, shows an enhanced magnetic susceptibility associated with the expansion of the Pd unit cell in the Au-Pd-Au epitaxial structure.[5] Finally, we expect that the models developed during our investigations for predicting and characterizing epitaxial growth and surface alloy formation will be generally applicable to the case of metal-on-metal growth.

At this point it is useful to spend some time in understanding the factors which determine the epitaxial growth of one material on another. First of all, the term "*epitaxy*" (Greek) means the "*growth of crystals on a crystalline substrate that determines their orientation*". Until about 1960, most theoretical approaches to the problem were based on the concept of a small misfit (lattice mismatch). Royer, who coined the term epitaxy[6], used x-ray diffraction to demonstrate that such oriented growth requires that lattice planes in both materials have similar structure. He concluded that epitaxial growth requires a misfit ε ($\varepsilon = |b-a|/a$, where a and b are the in-plane lattice constants of substrate and overlayer) of not more than about 15%. However, there are many important cases where the epitaxial layer has a totally different crystal structure (e.g., silicon on sapphire[7], CdTe on sapphire[8]). For such systems, the above criterion of lattice match is no longer applicable. Therefore a good lattice match is never a sufficient condition for epitaxial growth. We may hope, however, that the converse is true, namely that certain film faces will not grow as single crystals on a given substrate because of a poor lattice match.

Some other important parameters involved in determining epitaxial growth are substrate temperature, substrate orientation, deposition rate of adatoms, heat of formation, size of the adatom and the strain introduced by the overlayer. In general, the quantity which determines the growth mode may be written in simplified form as $\Delta = \sigma_f + \sigma_i - \sigma_s$, where σ_f and σ_s are the specific surface free energies of film and substrate, respectively, and σ_i the specific free interfacial energy[9]. Three modes of thin film growth are frequently observed, namely, the Volmer-Weber mode (3D crystals) results when $\Delta > 0$, and the Frank- van der Merwe (FM) and the Stranski-Krastanov (SK) modes when $\Delta \leq 0$. For the FM (monolayer by monolayer) mode to occur, the condition $\Delta \leq 0$ must be fulfilled for each layer h: $\Delta_h \leq 0$. In general, the condition $\Delta \leq 0$ can be fulfilled for only one or a few monolayers so that the SK mode (3D crystals on top of one or a few monolayers) will prevail. Depending upon the variation of Δ_h with h and of σ_i with the size and shape of the island in the h^{th} layer, transitions between the two modes may occur.

This thesis work is part of an ongoing investigation to understand the fundamentals which we discussed above to determine the growth modes of ultrathin transition metal films deposited on Al single crystal surfaces at room temperature. From our previous studies of Ti on Al(110) and Al(001) surfaces[10], we found that Ti films grow epitaxially up to a critical thickness, after which the growth mode changes in character. On the other hand, Ni films mix with the Al surface to form a surface alloy[11].

In this thesis work we explored the growth of ultrathin Pd films on Al(110) surfaces, and Fe, Co and Ag films on Al(001) and Al(110) surfaces. During the growth

process, the atomic structures of the overlayer and the substrate were monitored using different surface science techniques. In summary, we found that neither the aluminide formation energy, nor the lattice mismatch alone serve as useful parameters to predict epitaxial growth. Instead the relative size of the adatoms correlates well with the growth behavior for transition metals (Ti, Ni, Pd, Co and Fe) on Al surfaces as discussed in the summary section. The adatom size dependence was further tested using Ag which has a larger atomic diameter than the Al substrate atom.

In Chapter 2, the basic theory of the techniques that we used is briefly reviewed. The experimental setups and procedures are discussed in detail in Chapter 3. A combination of complementary surface science techniques was used to verify the initial state of the clean and ordered Al surfaces. These techniques were also used to monitor the growth of the deposited films at various stages of the experiment. The primary technique, high energy ion scattering (HEIS), along with x-ray photoelectron spectroscopy (XPS), and low energy electron diffraction (LEED) were used in this thesis work. In chapters 4, 5, 6 and 7, the results of ultrathin Pd, Fe, Co and Ag films deposited on Al surfaces are reported. The results of Chapters 4 and 5 have been published in Surface Science[12,13]. The results of Chapters 6 and 7 will be submitted for publication in the near future.

The following is a list of acronyms frequently used in this thesis:

AES	Auger electron spectroscopy
FAT	Fixed-analyzer transmission
FM	Frank-van der Merwe

FWHM	Full width at half maximum
HA	Hemispherical analyzer
HEIS	High energy ion scattering
LEED	Low energy electron diffraction
MC	Monte Carlo
MCA	Multichannel analyzer
MCS	Multichannel scaling
ML	Monolayer
PIPS	Passivated, implanted, planner silicon detector
PHA	Pulse height analysis
RBS	Rutherford backscattering spectrometry
RGA	Residual gas analyzer
SPA	Surface peak area
SK	Stranski-Krastanov
UHV	Ultra high vacuum
VEGAS	Ion scattering simulation program
VW	Volmer-Weber
XPS	X-ray photoelectron spectroscopy
XPD	X-ray photoelectron diffraction

REFERENCES

1. Surface Science techniques, edited by J. M. Walls and R. Smith, Pergamon, Elsevier Science, Inc., New York, 1994.

2. M. Tanaka, N. Ikarashi, H. Sakaibara, K. Ishida and T. Nishinaga, Appl. Phys. Lett. 60, (1992) 835.

3. S. A. Chambers, J. Vac. Sci. Technol. B 7, (1989) 737.

4. A. M. Wowchak, J. N. Kuznia and P. I. Cohen, J. Vac. Sci. Technol. B 7, (1989) 733.

5. M. B. Brodsky and A. J. Freeman, Phys. Rev. Lett. 45, (1980) 133.

6. L. Royer, Bull. Soc. Fr. Mineral. Crist. 51 (1928) 7.

7. G. W. Cullen, in Heteroepitaxial Semiconductors for Electronic Devices, edited by G. W. Cullen and C. C. Wang (Springer, New York, 1978).

8. T. H. Myers, Y. Cheng, R. N. Bicknell, and J. F. Schetzina, Appl. Phys. Lett. 42, (1983) 247.

9. E. Bauer, Appl. of. Surf. Sci., 11/12, (1982) 479.

10. Adli A. Saleh, Ph.D Thesis, Montana State University, 1994.

11. V. Shutthanandan, Ph.D Thesis, Montana State University, 1994.

12. N. R. Shivaparan, V. Shutthanandan, V. Krasemann and R. J. Smith, Surf. Science, in press.

13. N. R. Shivaparan, V. Krasemann, V. Shutthanandan and R. J. Smith, Surf. Sci., 365, (1996) 78.

CHAPTER 2

SHORT REVIEW OF THEORIES

Introduction

The experimental techniques used in this thesis work are high-energy ion scattering (HEIS), channeling, X-ray photoelectron spectroscopy (XPS), and low energy electron diffraction (LEED). The primary work has been measurement of the surface peak area (SPA) of the substrate (Al) and the adsorbate (Pd, Fe, Co, and Ag) in HEIS at different adsorbate coverages in order to investigate the behavior and growth modes of ultrathin transition metal films deposited on Al-single crystal surfaces. Furthermore, HEIS was used to measure the actual coverage of the adsorbate. In addition, XPS measurements have been performed to identify the chemical state of the reacted transition metal-Al interface during the adsorbate deposition. Also, LEED measurements have been used to perform surface crystallography including the atomic structure, epitaxial growth, the periodicity of atoms, and the overall symmetry of the surface, but not the detailed atomic positions. In this chapter we give a brief description of physical concepts and the theory behind these powerful surface science techniques. In the next chapter we will discuss the instrumentation and the experimental details of these techniques.

High-energy Ion Scattering and Channeling

It is well known that many chemical and electronic properties of surfaces and interfaces are related to the atomic structure at the surface or interfaces such that investigations of the surface and interface structure become more and more important. Rutherford Backscattering Spectroscopy (RBS) is a commonly used, non-destructive, surface analysis probe for structure determination in modern physics.[1,2,3] RBS has also proved to be a useful tool for in-depth analysis of thin film composition and structure. RBS spectra are straightforward to interpret because of the simple, classical nature of the ion-solid interaction. Considerable surface sensitivity is achieved when the incident ion beam is aligned along a low index crystal axis.

For MeV He^+ ions, the de Broglie wavelength is of the order of 10^{-12} cm; thus the crystal lattice is not viewed as a diffraction grating but rather as an array of rows and sheets of nuclei that collimate and steer the beam. When the ion beam is aligned along a crystal axis, on the scale of interatomic distances the ion is simply a point probe weaving through the channels provided by the rows and planes of atoms. Hence, this particular RBS technique is called high-energy ion scattering/channeling.

A hypothetical RBS spectrum from a single-element target is shown in Figure 2.1. The beam of energetic He^+ ions with energy E_o, mass M_1, and charge Z_1 strikes the sample (with atomic mass M_2 and charge Z_2) at normal incidence, and backscattered ions are detected at a scattering angle θ. While a small fraction of the beam scatters from the

surface atoms, additional scattering occurs from the atoms just below the surface. In moving through a sample before the scattering is encounter and passing back out through the sample after the scattering event, the ions continuously lose energy. The ions scattered from surface atoms will reach the detector with energy KE_o, where K is a constant less than unity. The ions scattered from the atoms which are below the surface will scatter at energies less than KE_o, as shown in Figure 2.1.

In the sections that follow, the four basic physical parameters that govern the RBS process: kinematic factor, differential scattering cross section, stopping cross section and energy straggling.

Kinematic factor K

For scattering at the sample surface the only energy loss mechanism is via momentum transfer to the target atom. Figure 2.1 illustrates the scattering of energetic ions from a single-element target. The energy of the ions backscattered from the surface atoms can be related to the incident energy via the kinematic factor K:

$$E_1 = K E_o, \tag{2.1}$$

where K is given by

$$K = \left[\frac{M_1 \cos\theta + (M_2^2 - M_1^2 \sin^2\theta)^{1/2}}{(M_1 + M_2)} \right]^2 \tag{2.2}$$

Equation 2.2 shows that the kinematic factor depends only on the masses M_1 and M_2, and the scattering angle θ.[1]

Differential scattering cross section $d\sigma/d\Omega$

The relative number of particles backscattered from a target atom into a given solid angle Ω for a given number of incident particles is related to the differential scattering cross section. The probability for the scattering event to occur as illustrated in Figure 2.1 depends on the average scattering cross section σ. For a small Ω, the average scattering cross section can be approximated using the differential scattering cross section $d\sigma/d\Omega$. Moreover, if the interaction between the ions and the atoms is specified by the Moliere potential,[4] then the differential scattering cross section is given by[5]

$$\frac{d\sigma}{d\Omega} = F\left[\frac{Z_1 Z_2 e^2}{2E_o \sin^2\theta}\right]^2 \frac{\left[\left(1-\left[\frac{M_1}{M_2}\sin\theta\right]^2\right)^{1/2}+\cos\theta\right]^2}{\left[1-\left[\frac{M_1}{M_2}\sin\theta\right]^2\right]^{1/2}} \qquad (2.3)$$

where F is a screening correction factor

$$F = 1 - \frac{0.042 Z_1 Z_2{}^{4/3}}{E(keV)} \qquad (2.4)$$

Stopping cross section

Only a small fraction of the incident He ions undergo a close encounter with an atomic nucleus and are backscattered out of the sample. The vast majority of the incident He atoms end up implanted in the sample. When probing particles penetrate to some depth in a dense medium, the projectile energy dissipates due to interactions with

electrons and to glancing collisions with the nuclei of target atoms. This means that a particle which backscatters from an element at some depth in a sample will have measurably less energy than a particle which backscatters from the same element on the sample surface. The majority of energy loss is caused by electronic stopping which behaves like friction between the probing particles and the electron clouds of the target atoms. If we consider these energy losses in the solid for the ingoing and outcoming ions, then ΔE, the energy difference between ions scattered from the surface and ions scattered at a depth x from the surface, is given by[1]

$$\Delta E = x \left[\frac{K}{\cos\theta_1} \frac{dE}{dx} \Big|_{E_0} + \frac{1}{\cos\theta_2} \frac{dE}{dx} \Big|_{KE_o} \right] \tag{2.5}$$

θ_1 is defined as the angle between the surface normal of the sample and the direction of the incident ions, and θ_2 is defined as the angle between the normal direction and the direction of backscattered ions. For normal incidence, $\theta_1 = 0^\circ$ and $\theta_2 = 180^\circ - \theta$, where θ is the scattering angle in the laboratory. Energy loss dE/dx is related to the stopping cross section ε by the following equation

$$\frac{dE}{dx} = \varepsilon N, \tag{2.6}$$

where N is the atomic density of the target atoms.

Using equation 2.5 and 2.6, we can convert the energy-difference equation into a depth equation[1], i.e.,

$$\Delta E = N \, x \, [\varepsilon] \tag{2.7}$$

with

$$[\varepsilon] = \left[\frac{K}{\cos\theta_1}\varepsilon(E_o) + \frac{1}{\cos\theta_2}\varepsilon(KE_o)\right] \tag{2.8}$$

$\varepsilon(E_o)$ and $\varepsilon(KE_o)$ are evaluated at energy E_o and KE_o, respectively.

Energy straggling

After passing through a target with a finite thickness the probing He atoms will not only lose energy, but they will also no longer be monoenergetic. Instead, they will have a distribution of energies which is predicted by energy loss calculations. The process through which a probing He atom loses energy involves a large number of interactions with individual atoms along its trajectory through the sample. The trajectories differ from one particle to the next so that identical energetic particles, with the same initial velocity do not have exactly the same energy after passing through a solid medium. The variation in energy loss is called energy straggling. Furthermore, straggling sets a fundamental limit on the depth resolution possible with ion beam energy loss techniques. The majority of energy loss occurs through interaction with electrons. As a result, energy straggling increases with the atomic number of the target element, since atomic number also reflects the number of electrons present. Energy straggling causes the low energy edge of peaks to broaden. For thick, high Z materials this effect can be quite pronounced. The accuracy of depth resolution depends on how accurately the contribution of straggling can be calculated.

Scattering Yield

In backscattering measurements the total number of detected particles, or yield Y, from a thin layer of atoms, Δt, is given by

$$Y = Q\,N\,\Delta t\,\frac{d\sigma}{d\Omega}\Omega, \tag{2.9}$$

Q is the measured number of incident particles at the target,

$N\Delta t$ is the number of target atoms/cm^2 in the layer of thickness Δt with atomic density N (atoms/cm^3),

$d\sigma/d\Omega$ is the differential scattering cross section and

Ω is the solid angle subtended by the detector.

For the example illustrated in Figure 2.1, the ion scattering yield in the surface region of the sample is equal to the height H_o of the spectrum. Using equation 2.9 and 2.6, H_o

$$H_o = \frac{d\sigma(E)}{d\Omega}\Omega Q\frac{\delta E}{[\varepsilon]}, \tag{2.10}$$

where δE is the energy loss associated with thickness Δt of the sample, and is typically the energy width of a single channel in the energy distribution spectrum. The other parameters are the same as before.

Channeling

The principle of channeling can be illustrated by Figure 2.2. When a beam of ions is incident parallel to a major crystallographic axis or plane, the average electric field of the columns or planes of atoms acts to gently guide the ions down the center of the channel. The ions spiral down the axis where the electron density is at its lowest with a characteristic wavelength of a few tens of nm. The rate of energy loss is therefore less for channeled ions than for non-channeled ions, and the ions seldom come close enough to the lattice nuclei to suffer a large angle scattering event. A small fraction of the incident ions will collide with nuclei in the top plane of atoms and be scattered. However, subsequent crystal atoms will be in the shadow of the top atom and cannot contribute to the RBS yield. This is illustrated in Figure 2.3 which shows the surface interactions between the incident beam and a single crystal target. In a static representation, i.e., no thermal motion, the flux distribution of ions has a distance of closest approach to the second atom, R, within which there are no ions. Thus the small-angle forward scattered ions form a "shadow cone" with radius R_c, that extends into the solid (see Figure 2.3). For Coulomb scattering,

$$R_c = 2\sqrt{\frac{Z_1 Z_2 e^2 d}{E}} \tag{2.11}$$

For helium ions channeled down a major crystallographic axis, the RBS yield from atoms behind the first layer can be as low as 1% of that from an amorphous sample of the same material. If the ion beam is gradually directed away from the crystal axis, an angle will be

reached, known as the critical angle Ψ_c, at which the steering effect can no longer channel the beam and the RBS yield will increase. Such an angular yield curve (yield of ions as a function of the angle, Ψ, between the incident ion beam and symmetry direction of the crystal) is illustrated in Figure 2.4. For helium ions, the width of the angular yield curve $\Psi_{1/2}$ lies typically within the range 0.3 to 1.2°. It can be calculated using the following equation:[7]

$$\Psi_{1/2} = 0.8 F_{RS}(\xi)\Psi_1 \tag{2.12}$$

where

$$\psi_1 = 0.307\ (Z_1\ Z_2/E\ d)^{1/2}\ \text{(degrees)} \tag{2.13}$$

The incident energy E is in MeV, ξ = 1.2 ρ/a (ρ is the one dimensional rms vibration amplitude and a is the Thomas-Fermi screening radius), d = 0.707 a, and F_{RS} = square root of the dimensionless string potential obtained using Moliere's screening function. For 1 MeV He^+ ions incident along the [001] direction of Al, R_C = 0.055 Å. Since the bulk value of ρ is 0.105 Å (at room temperature), the shadowing is not big enough to cover the second atom.

The reduction in the yield of backscattered ions on an Al(001) crystal is shown graphically in Figure 2.5 by comparing the spectrum for the channeled yield or aligned yield with that for the random yield. Roughly 95% of the incident He^+ ions are channeled through the crystal. Note that it is this suppression of the scattering from the bulk in the aligned spectrum that permits measurement of the surface peak and hence provides information on the surface structure. Due to the limitations of depth resolution, the

aligned yield will show a small *surface peak* (SP), spread over the first few channels of the spectrum. Random spectra can be collected when the crystal axes are tilted away from the incident beam direction so that incident particles are not channeled, and encounter nearly all of the target atoms. The yield collected in the random direction is referred to as the *random yield.*

The surface peak is a measure of surface order, while the minimum yield behind the surface peak (Figure 2.5) is a measure of the bulk crystal perfection. In addition, a measure of the channeling effect is the quantity $\chi_{min,}=Y_A/Y_R$, defined as the ratio of the aligned to random yield. This minimum yield can be calculated from the relation[7]

$$\chi_{\min} = Nd\pi(2u_1^2 + a^2) \qquad (2.14)$$

where N is the atomic density, u_1 is the atomic one dimensional thermal vibrational amplitude, d is the interatomic distance along the row, and a is the Thomas-Fermi screening radius. Values of χ_{min} are typically between 1% and 4%. The value of χ_{min} from Fig. 2.5 is 3.6%.

In Figure 2.5 the surface peak area (SPA) is a direct measure of how many surface atoms are visible to the incident ion beam. Thus if we know the SPA (yield Y), Q, Ω and the differential scattering cross section, then by using Equation 2.9 we can calculate the product NΔt, the number of atoms per unit area visible to the incident beam.

Ion channeling is also well suited to study overlayer/substrate interactions[1]. Figure 2.6 demonstrates five simple cases of how this technique can be utilized in surface studies and shows the corresponding surface peak spectra. Fig. 2.6(a) represents

the scattering yield from a crystal with an ideal surface for the case where the thermal vibration amplitude ρ is much less than the shadow cone radius R_c. This is the condition that assures that the surface peak intensity corresponds to one atom/row in this ideal case. Fig. 2.6(b), represents a situation where the second atom is not shadowed. The surface peak intensity in this case is twice that of the ideal crystal. In a number of crystals, the inter-layer separation between the surface layer and the second layer differs from the bulk layer separation. This effect is called surface relaxation. To test for relaxation, one must also use a nonnormal incidence direction, so that the shadow cone established by the surface atoms is not aligned with the atomic rows in the bulk. The normal incidence yield would still give a surface peak intensity equivalent to approximately one monolayer. These two measurements, at normal and oblique incidence, would reveal the presence of relaxation. In Fig. 2.6(d) an adsorbate atom is positioned exactly over the surface atoms (e.g in epitaxial growth) and hence shadows the surface atoms and reduces the substrate surface peak. Examples of epitaxial systems are Ti on Al[9] and Ag on Al (Chapter 7). On the other hand, an increase in the substrate peak area as a function of overlayer thickness, where the ion beam is aligned with the substrate, is indicative of mixing where the substrate atoms are displaced from their equilibrium positions as shown in Fig 2.6(e). Examples of mixing are explained in detail in Chapters 4[10] ,5[11] and 6[12]. Note that the coverage of adsorbate atoms on the surface is determined directly from the area of the surface peak for the adsorbate (shaded peaks in Fig. 5).

X-ray Photoelectron Spectroscopy

The interaction of an X-ray photon with a sample may lead to the ejection of photoelectrons, as shown schematically in Figure 2.7. This diagram illustrates the X-ray photon interacting with an electron in the K-shell, causing the emission of a 1s photoelectron. The resulting K shell vacancy is filled by an electron from a higher energy level, which can lead to either X-ray fluorescence or the radiationless de-excitation process of Auger emission. The determination of the kinetic energy of the outgoing photoelectron is the cornerstone of experimental XPS. The kinetic energy (E_k) of the ejected photoelectron is related to the electron binding energy (E_B), the parameter that defines both the element and atomic level from which it emanated, and other instrumental terms in the following manner.[8]

$$E_k = h\nu - E_B - E_R - \phi \qquad (2.15)$$

E_R is the recoil energy, a minor component of the calculation (0.1-0.01eV), which is less than other uncertainties within the expression and is generally ignored. The sample work function is represented by ϕ. As the photon energy of the X-rays ($h\nu$) and ϕ are known and E_k is determined experimentally, E_B can be determined.

A typical X-ray photoelectron spectrum is illustrated in Figure 2.8 and the various components that contribute to it are clearly evident. From the energetic positions, intensities, and in some cases the shapes of the various peaks, one can extract valuable information about the sample. Conventionally, the origin of the energy scale is taken at

the Fermi level E_F of the solid (for metals), and the energetic separation of the different peaks is denoted by their binding energies E_B. The characteristic XPS core level peaks are superimposed on a background of inelastically scattered electrons.

Element identification

X-ray photoelectron spectroscopy is a straightforward and useful technique for the identification of atomic species at the surface of a solid. From the XPS spectrum shown in Figure 2.8, we are able to identify the elements present in the surface region of the sample. Since the binding energies of each element are well defined, the peak identification of the elements in XPS spectra is straightforward. Other important information beyond simple binding energy data and element identification can also be gleaned from an XPS spectrum. For example, the spin orbit splitting can be seen in Figure 2.9, where an XPS spectrum for the Pd 3d core-level is shown.

Chemical Shifts

The concept of chemical shifts is based on the idea that the inner shell electrons feel an alteration in binding energy due to a change in the valence shell contribution to the potential, as a result of the outer electron chemical bonding. In the simplest picture, valence electrons are drawn away from or toward the nucleus depending on the type of bond. The greater the electronegativity of the surrounding atoms, the more the displacement of electronic charge from the atom and the higher the observed binding

energies of the core electrons. An example of the shift in the Al 2p XPS spectrum as a result of formation of Al_2O_3 is shown in Figure 2.10. Here the shift in the Al signal represents 2.1 eV for the transformation from Al to Al_2O_3.

Quantitative Analysis

One of the major advantages of XPS is the ease with which quantitative data can be routinely obtained. This is usually performed by determining the area under the peak (intensity) in question. The intensity of a given line depends on a number of factors including the photoelectric cross section σ, the electron escape depth λ, the spectrometer transmission, surface roughness or inhomogeneities, as well as the presence of satellite structure. A photoelectron which originates at a certain depth below the surface will lose energy through inelastic scattering events involving other electrons. Due to this energy loss, not all the photoelectrons excited from a given subshell contribute to the photopeak. The number of electrons that can escape from a solid without undergoing an elastic collision decreases with the depth x as $\exp(-x/\lambda)$, where λ is the mean free-path. Alternatively, the intensity of photoelectrons unscattered after traveling through a material of thickness x is given by the following equation.

$$I(x) = I_o \exp\left[\frac{-x}{\lambda(E_k).\cos\Theta}\right] \qquad (2.16)$$

where I_o is the photoelectron intensity at depth x, and Θ is the angle of emission with respect to the surface normal. In order to calculate the emission intensity, a proper

background subtraction should be performed in any of the original XPS spectra. There are different forms by which background can be removed, namely linear, Tougaard, and polynomial. In Appendix, the curve fitting routines used for background subtraction, and the different line shapes of the XPS peaks in this thesis work are discussed in more detail.

Low Energy Electron Diffraction

In our LEED measurements, an electron with a wavelength λ (energy 20 to 500 eV) impinges perpendicular to a periodic row of atoms with interatomic spacing *a*. Constructive interference will occur when the electron wavelets scattering from one atom are in phase with waves scattered from adjacent atoms. This situation is shown schematically in Figure 2.11.[4] In 1-D, there will be cones around the axis of the row where constructive interference can occur and where we will have a finite probability of finding the electron. A two-dimensional periodic arrangement with primitive atomic spacing *a* and *b* will generate two sets of diffraction conditions which must be met simultaneously, namely

$$n_a\lambda_a = a \sin\theta_a \qquad n_b\lambda_b = b \sin\theta_b \tag{2.17}$$

As both conditions must be met simultaneously, the only regions where we may find the electron are in the intersections of these cones. It is obvious that the intersection of two cones with a common origin will result in a set of lines. If we set a detection device

across this set of lines, we will perceive them as spots or points which are called LEED patterns. The experimental details of LEED shall be discussed in the next chapter.

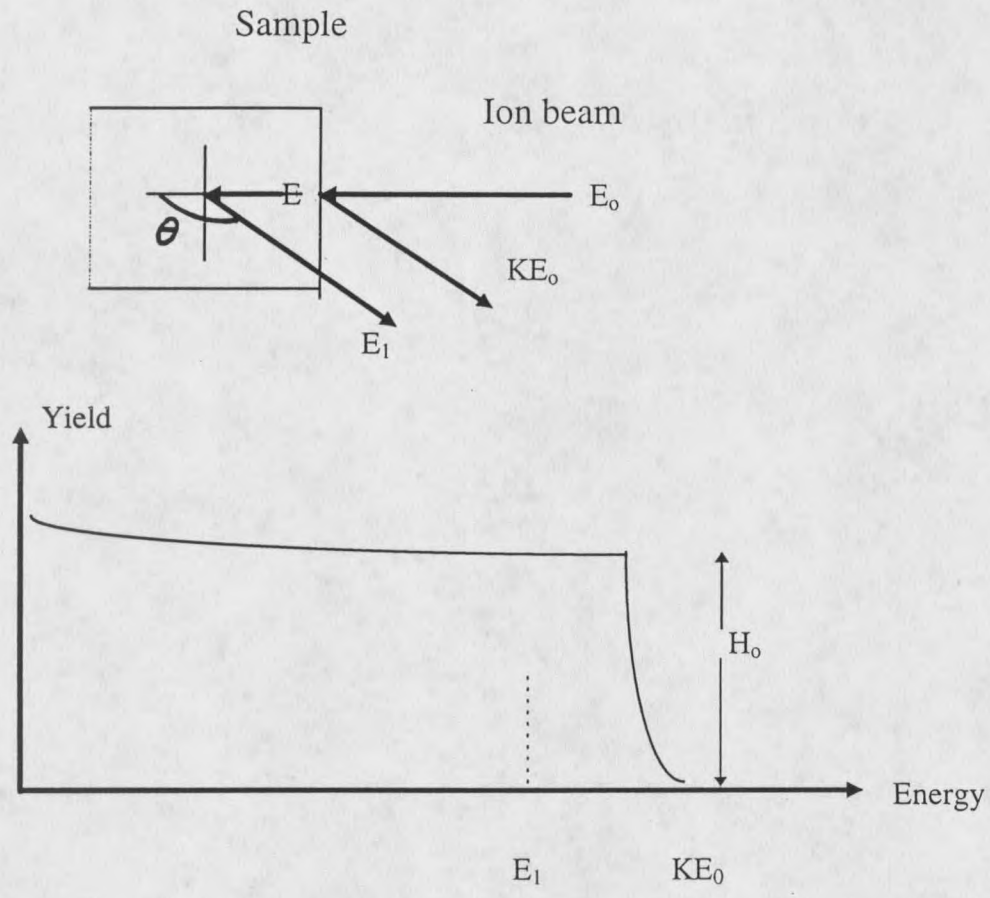

Figure 2.1: Schematic of Rutherford backscattering spectroscopy (RBS)

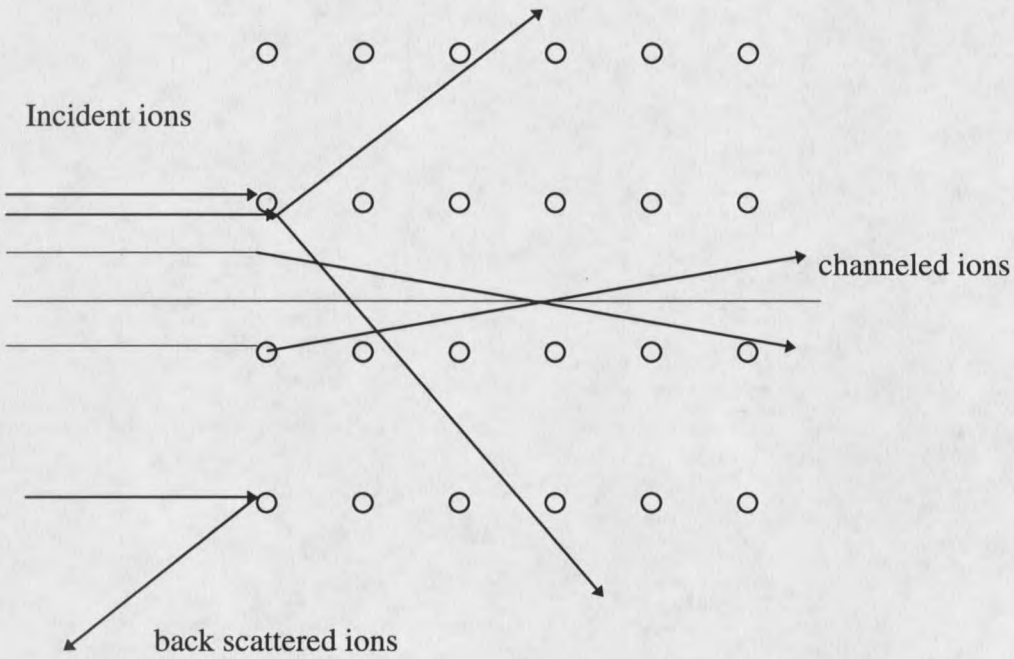

Figure 2.2: A schematic representation of possible particle paths for a beam of ions incident parallel to a crystal axis or plane.

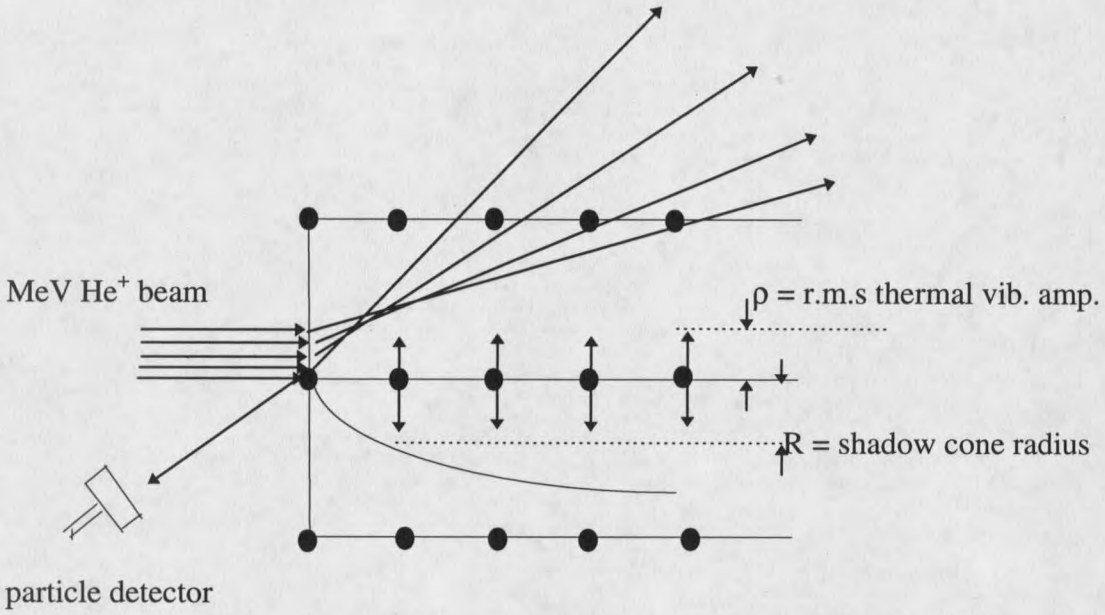

Figure 2.3: Ion trajectories near the surface of an aligned single crystal and the formation of the shadow cone.

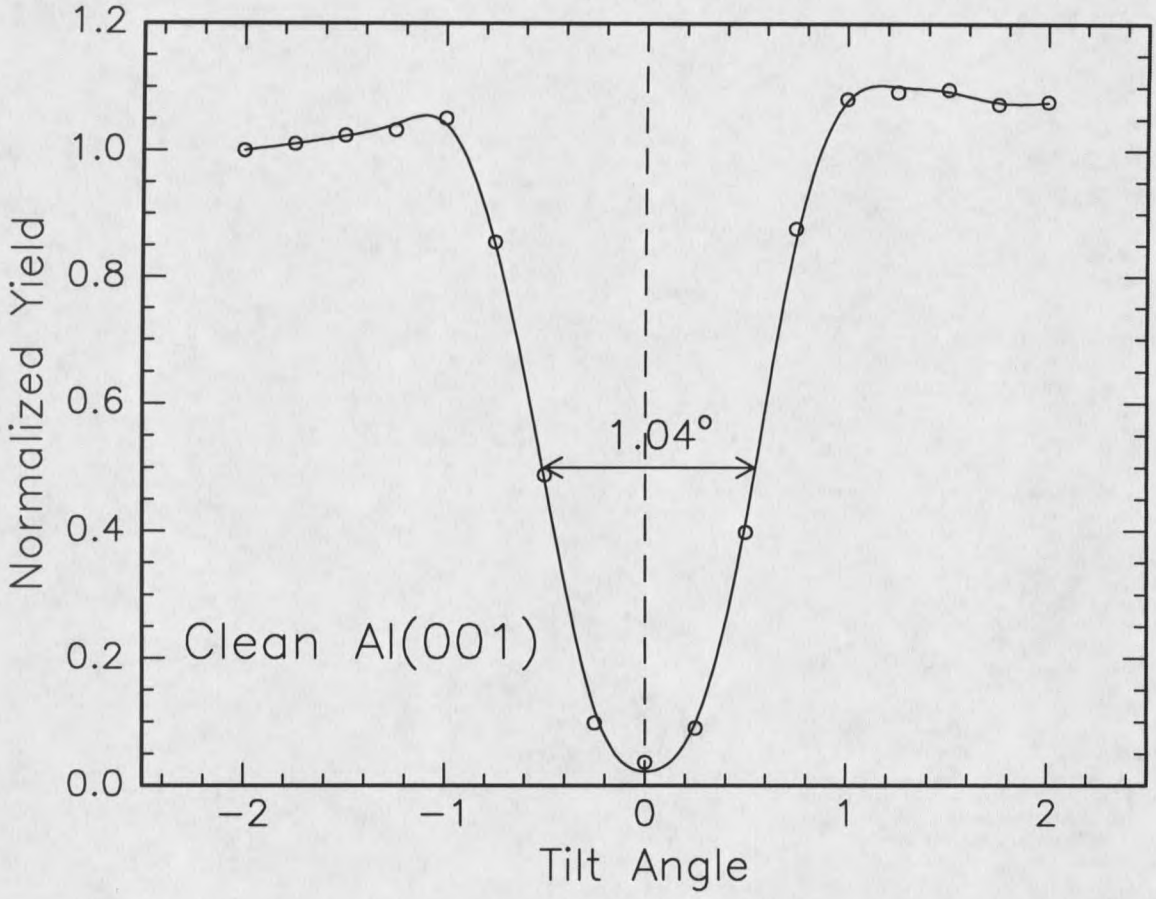

Figure 2.4: A plot of the ratio of the channeled to random RBS yield as an Al(001) crystal is tilted relative to a channeling axis.

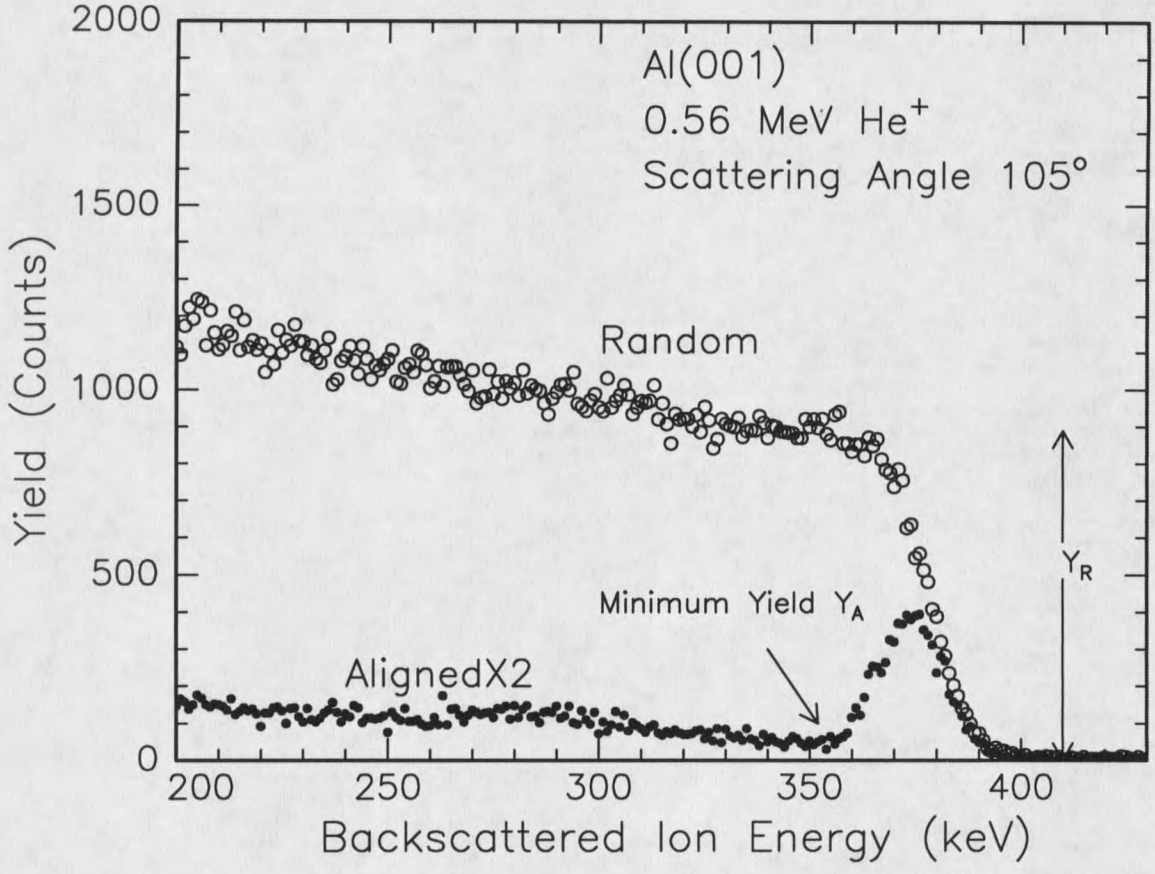

Figure 2.5: Comparison between the channeling/aligned spectrum (closed circles) and the random spectrum (open circles) for He^+ ions backscattering from the Al(001) surface.

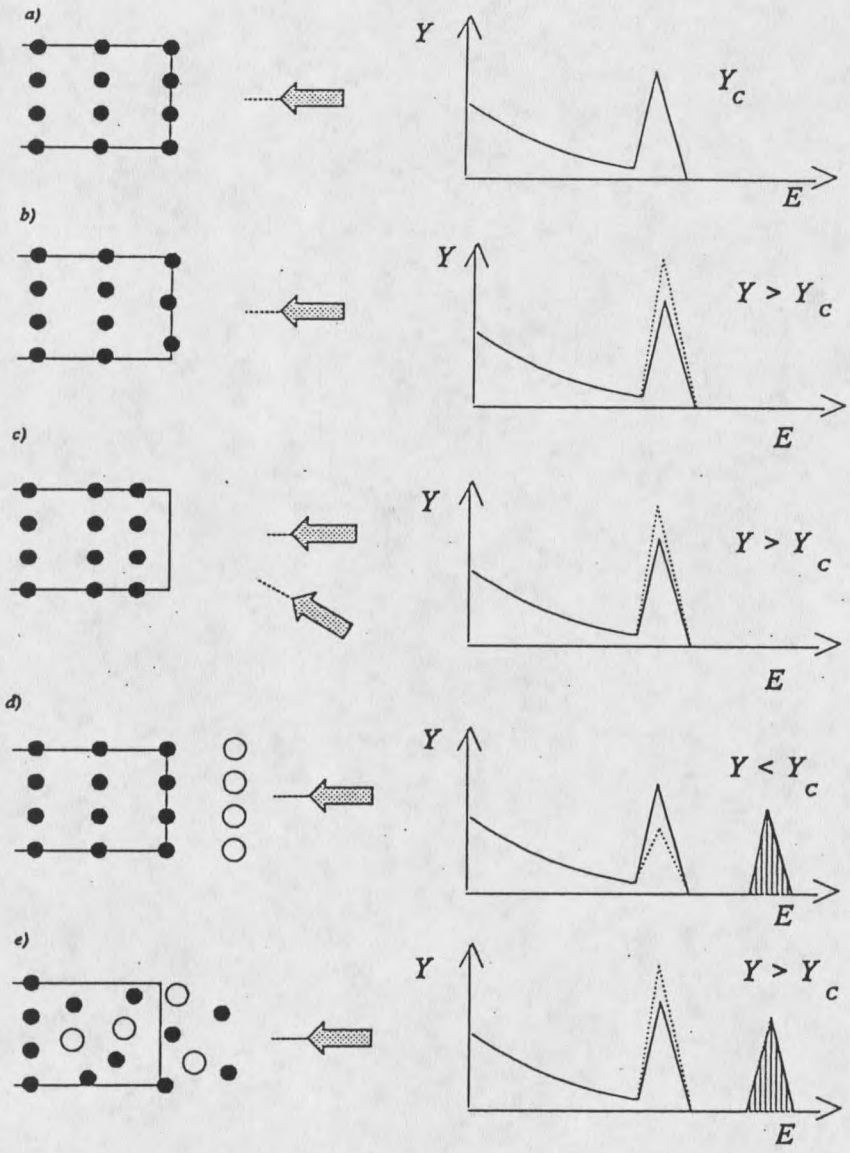

Figure 2.6: Representations of different surfaces on a single cubic crystal. (a) bulk terminated clean surface (b) reconstructed surface (c) relaxed surface (d) epitaxially ordered overlayer (e) mixed interface.

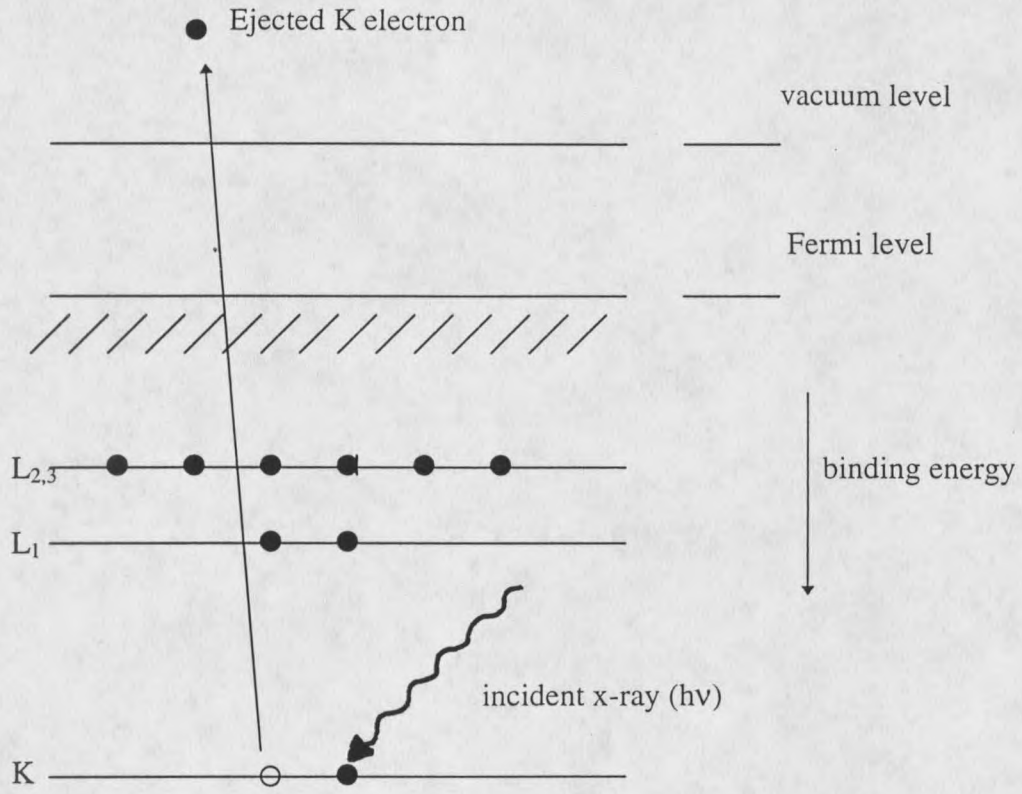

Figure 2.7: Schematic of the photoemission process.

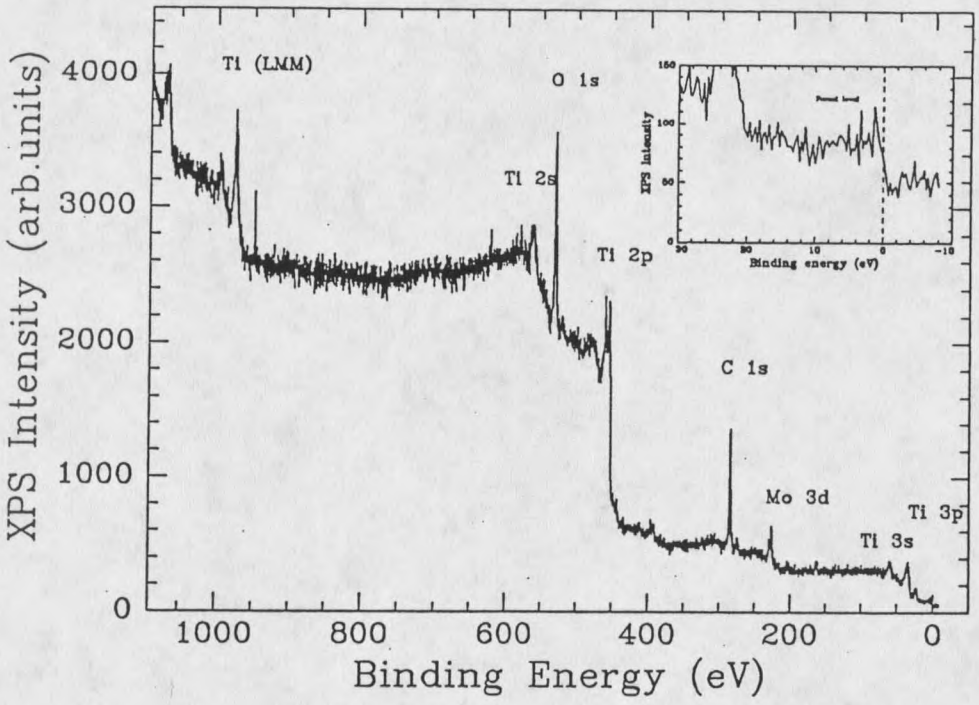

Figure 2.8: XPS spectrum from a titanium alloy. For clarity, the region near the Fermi level is shown in the insert.

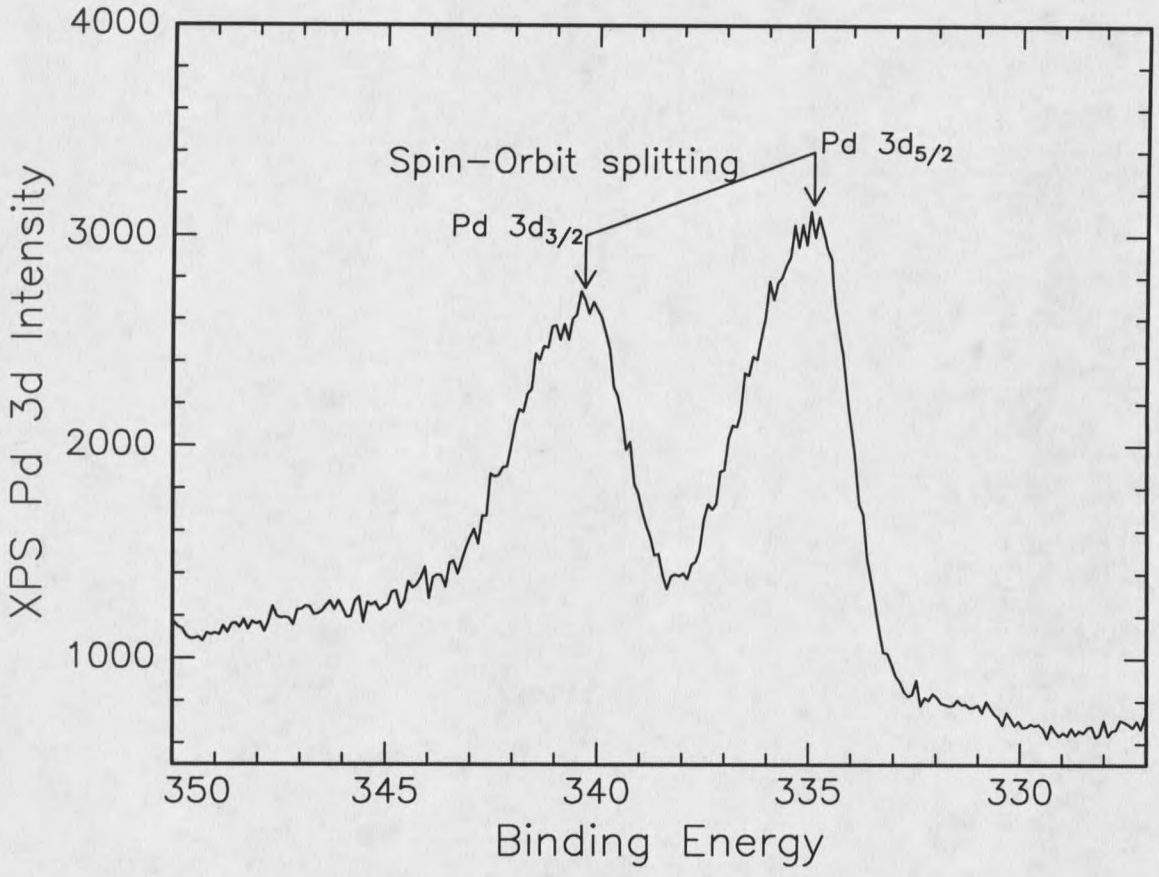

Figure 2.9: XPS spectrum for an 8 ML Pd film deposited on the Al(110) surface. Spin-orbit splitting is shown in the figure.

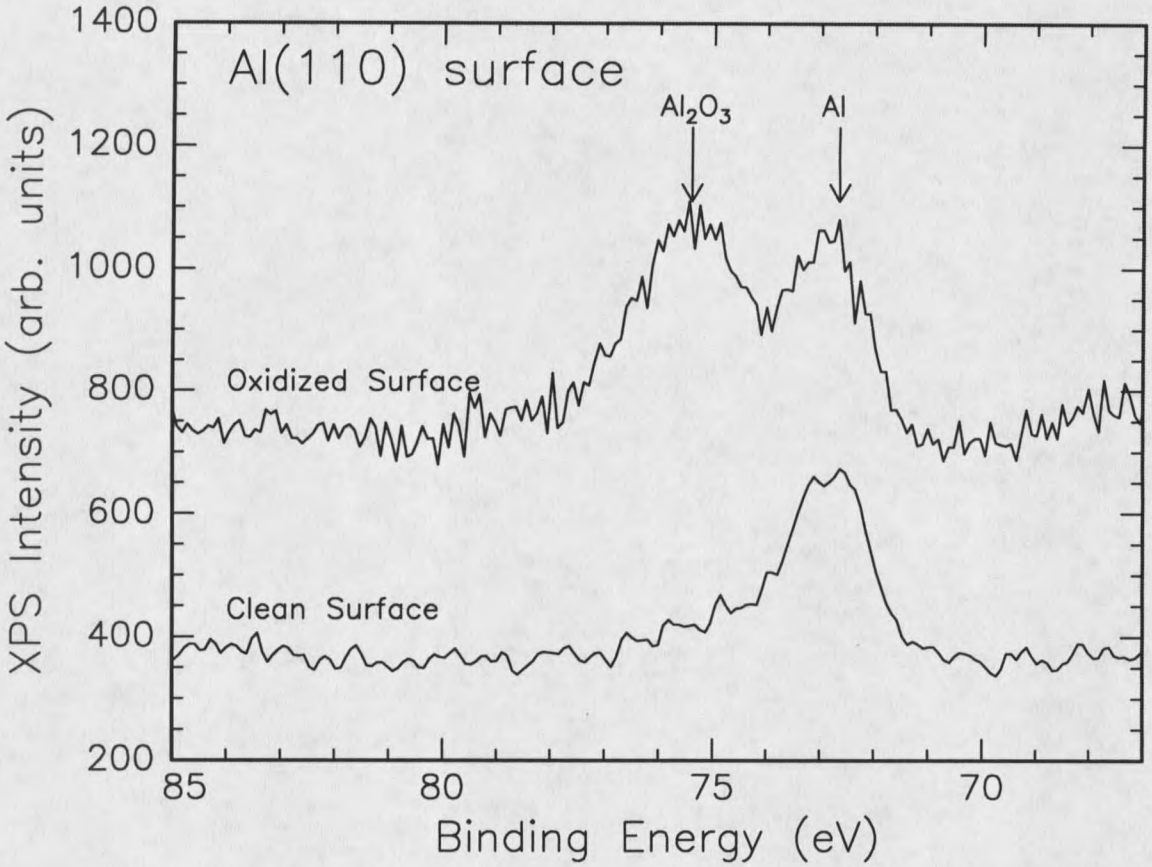

Figure 2.10: Al 2p XPS spectrum for an uncleaned (dirty) Al(110) surface. The arrows in the figure indicate the binding energy positions of the Al_2O_3 and the Al photopeaks.

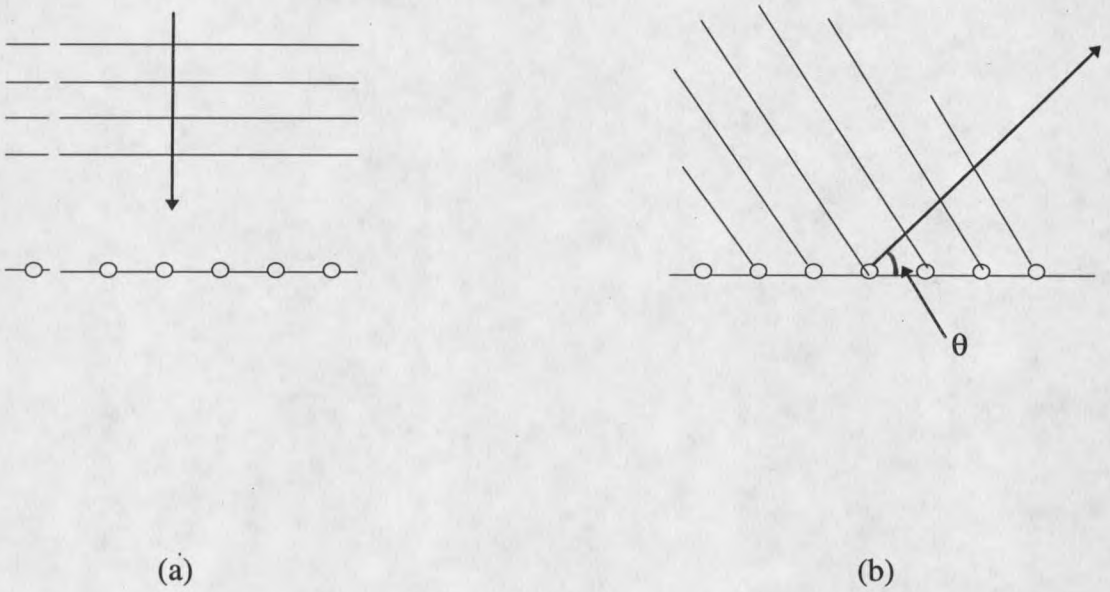

(a) (b)

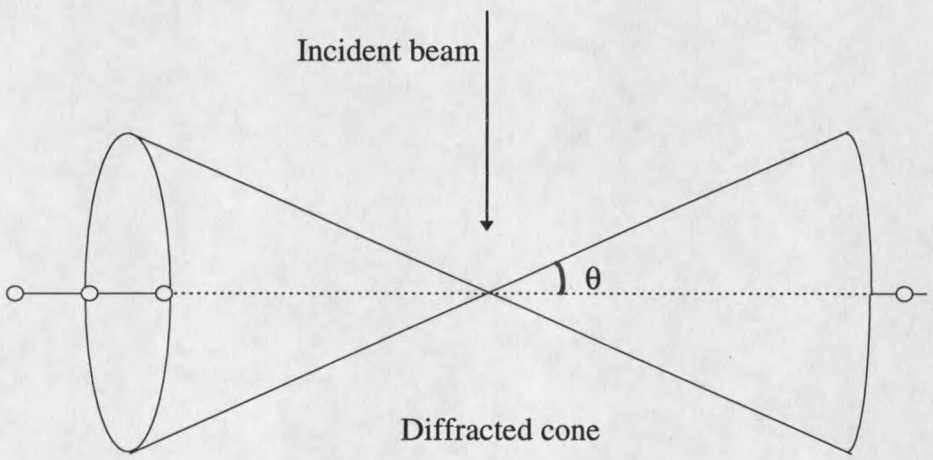

(c)

Figure 2.11: Diffraction of a particle from a row of scattering centers: (a) Incident plane wave (b) Scattered wave front (c) Cone of constructive interference.

REFERENCES

1. L. C. Feldman, J. W. Mayer, and S. T. Picraux, *Materials Analysis by Ion Channeling* (Academic Press, New York, 1982).
2. W. K. Chu, J. W. Mayer, and M. A. Nicholet, *Backscattering Spectrometry* (Academic Press, New York, 1978).
3. J. F. van der Veen, Surf. Sci. Reports, Vol. 15, 199 (1985).
4. L. C. Feldman, and J. W. Mayer, *Fundamentals of Surface and Thin Film Analysis* (North-Holland, New York, 1986).
5. Xu Mingde, Ph.D Thesis, Montana State University (1990).
6. RBS Theory, Charles Evans & Associates Home Page, *www.cea.com.*
7. J. W. Mayer, and E. Rimini, *Ion Beam Handbook for Materials Analysis* (Academic Press, New York, 1977).
8. *Surface Science Techniques*, Edited by J. M. Walls, and R. Smith (Pergamon, New York, 1994).
9. Adli A. Saleh, V. Shutthanandan, and R. J. Smith, Phys. Rev. B49, 4908(1994).
10. N. R. Shivaparan, V. Shutthanandan, V. Krasemann, and R. J. Smith, in press Surf. Sci.
11. N. R. Shivaparan, V. Krasemann, V. Shutthanandan, and R. J. Smith, Surf. Sci., 365, 78(1996).
12. N. R. Shivaparan, V. Krasemann, and R. J. Smith, (to be submitted to Surf. Sci.).

CHAPTER 3

EXPERIMENTAL TECHNIQUES AND PROCEDURES

Introduction

Modern surface science methods over the last four decades have been dominated by requiring ultrahigh vacuum (UHV) chambers in which to carry out the analyses[1]. Because of the susceptibility of surfaces to contamination in an atmospheric environment, ultrahigh vacuum is of course required by those techniques utilizing beams of particles and higher energy radiation so that the beams may be generated and travel undisturbed until intercepting the surface. The requirement for UHV ($\leq 10^{-10}$ Torr) is fundamental to surface analysis when those beams are employed. This arises due to the flux of residual gas molecules striking the surface i.e. the number of molecules per unit area per unit time, which is responsible for the pressure that those gas molecules exert upon the surface. For a typical surface, a calculation of the areal atomic density yields a value of 10^{15} atoms/cm^2. A computation for the rate at which contamination takes place leads to the result that the whole surface would be completely contaminated one second after exposing the sample to a pressure of 10^{-6} Torr for one second. In this case, the sticking coefficient is assumed to be unity. When the pressure is maintained at about 10^{-10} Torr, a time period of about 10^4 seconds is available to carry out the experiments before the surface is seriously contaminated. Furthermore, all ion- and electron beam surface

science techniques require high vacuum environments because the mean-free-path associated with ions and electrons is very short at atmospheric pressures. Also with x-ray sources, lens elements, and electron multipliers in electrostatic analyzers, high vacuum is necessary to avoid any low break-down voltage of gases at intermediate pressures. In addition, hot elements like wire filaments are also severely affected by poor vacua, leading to very short lifetimes.

All of our experiments were performed in an UHV chamber which is equipped with facilities for HEIS, XPS, LEED, Ar-ion sputtering, residual gas analysis, and thin film depositions as shown in Figure 3.1 and 3.2[2]. The 2 MV Van de Graaff accelerator is connected to the chamber via a differentially pumped beam line which is also shown in Figure 3.2 and Figure 3.3[2]. In this chapter, a description of the experimental setup is presented in detail.

Ultrahigh vacuum chamber

Figures 3.1 and 3.2 are schematic drawings of the side view and the top view of the UHV chamber, respectively. The UHV chamber is fabricated from stainless steel and the inside of it is lined with μ-metal to provide magnetic shielding. All the view ports on the chamber are pointing towards the sample in Figure 3.2. A pressure in the low 10^{-10} Torr range is achieved using a Balzers TPH 230 turbo-molecular pump (11), Varian ion-getter pumps (8,9), and the titanium sublimation pump (7). A roughing pump (12) with a foreline trap is connected to the chamber through the turbo pump for the initial vacuation

of the chamber. An initial pressure of 10^{-8} Torr is attained using the turbo and ion pumps. Total pressure measurement in the chamber is made with the aid of an ionization gauge (29). A Dycor Electronics M100M quadrupole residual gas analyzer (RGA) (20) is mounted to monitor the composition of the gas present in the chamber. The RGA can also be used to find leaks in the vacuum system using helium as a trace gas. The entire vacuum chamber and the beam line are normally baked at 150° C for one to two days to remove water vapors, oil vapors and promote outgassing of adsorbed species. During the bake out, temperatures of the sample (1), ion detector (2), and the ion pump (8) are continuously monitored in order to avoid any excessive heating. After the baking, a pressure of high 10^{-10} Torr is obtained inside the chamber. By using the RGA we find that the main contribution to the total pressure is the residual hydrogen. Then after using the titanium sublimation pump (TSP) in which a freshly evaporated Ti surface develops high pumping rates of hydrogen in the lower pressure ranges, the best vacuum (low 10^{-10} Torr) is reached. Argon is admitted to the vacuum chamber through bakeable leak valves (24, 25) which allow controlled inlet rates into UHV directly from atmospheric pressure. These leak valves (24, 25) and the argon gas bottle are connected to the chamber through a separate vacuum system which contains two sorption pumps (10) and a reservoir (26) as shown in Figure 3.2. The reservoir is evacuated by using the sorption pumps prior to filling with argon gas.

High-energy Ion Scattering

van de Graaff Accelerator

Figure 3.3 shows a line drawing of the Van de Graaff accelerator (32), UHV beam line (17) and the UHV chamber (41)[2]. The high-energy ion which we used in these experiments are extracted from the Van de Graaff accelerator. It is used as a variable flux source of well focused and collimated H^+ and He^+ beams. Primarily, the accelerator consists of an ion source and an evacuated column (10^{-6} Torr) with a strong potential gradient of about 10^6 V/m. It is connected to a field free evacuated beam pipe that leads to a strong analyzing magnet and then to the chamber. He or H gas is leaked into the ion source where an *rf* field is used to ionize the gas. Ionization is enhanced by means of a quadrupole magnet located around the ionization vessel. A potential gradient is established and maintained along the column by continuous charging of the positive terminal (a shiny dome-shaped steel overlay). This is accomplished using a highly insulated belt that transfers positive charges from a (0-30) kV spray charge power supply to the high-potential end of the column. The column includes a large number of equipotential electrodes, connected in series with a string of resistors between the high potential terminal and ground.

During the operation of the accelerator, a delicate balance between charge deposited on the terminal and charge leakage to ground through different channels is maintained. An important channel is the one in which charge is transferred to a collection of sharp pointed needles positioned directly above the terminal. These are referred to as

corona points, while the charge transfer is known as the corona current. The corona points are brought closer to the terminal to lower the terminal potential, and are retracted away from the terminal to increase the potential. This control mechanism allows the fine adjustment of the potential gradient, while the course adjustment is obtained using the variable spray charge power supply. The corona points are also essential in the voltage stabilization circuit. The stabilization is accomplished via the outcoming ion beam and analysis magnet. A small perturbation in the potential gradient is translated into a deviation in the kinetic energy of ions accelerated down the column. The switching magnetic field deflects the ions with the desired energy into the scattering chamber. An ion beam with higher kinetic energy will have a smaller deflection, while ions with lower kinetic energy will have a larger deflection. Two collector slits, horizontally positioned inside the beam line a few millimeters apart, are used to measure a portion of the current associated with the ion beam. These slits are part of a feed-back circuit where an appropriate voltage, proportional to the measured difference in the slit current, is applied to the corona points to reduce or increase the corona current, affecting the charge balance on the accelerator terminal and thus stabilizing the ion energy. The desired energy of the ions is usually selected from the accelerator control unit. Usually, these energies are calibrated by using nuclear reaction methods such as $^{27}Al(p,\gamma)^{28}Si$ and $^{19}F(p,\alpha)^{16}O$, since these reactions occur at well known beam energies[3]. These calibrations are only used as a guideline to get the desired beam energy. However, the exact beam energy is found by using the measured energy of the surface peak and the backscattering spectrum for a

random incident direction on a known sample. Energy calibration is also checked using a pulse generator calibrated against a radioactive ^{210}Po alpha emitter.

In order to preserve the UHV vacuum conditions in the analyzing chamber while we are operating the accelerator, the beam line is differentially pumped using one ion pump (9) and two 1 mm diameter apertures (6), as shown in Figure 3.3. These apertures also serve as the collimators of the ion beam, since a well collimated ion beam is necessary in the ion channeling experiments[4].

Ion beam detection

A silicon surface barrier detector (2) is used for ion beam detection. This semiconductor is a large-area diode consisting of an extremely thin p-type layer on the sensitive face of a high-purity, n-type silicon wafer. When a charged particle enters this detector it creates free electron-hole pairs over a certain length (typically 5μm for 1 MeV ions)[5] by losing energy at a rate of 3.6 eV/electron-hole pair. If ε is the energy for creating an electron-hole pair, and if the particle energy is E, then the number of carriers created in this process is equal to 2E/ε. The rate of charge carrier formation is nearly independent of particle type over a wide range of energies, provided the sensitive depth of the detector (W) exceeds the range of the particle, and provided also that the electric field in the sensitive region is sufficiently large to separate the charge carriers before they recombine. These created carriers are then collected by a biased (usually with 50 Volts) gold electrode on the semiconductor surface to give an output pulse, where the amplitude of

the pulse is proportional to the energy of the incident ion. The number of pulses at this amplitude gives the number of ions at that energy. Hence, the amplitude of the pulse and the number of carriers created with this amplitude will define the energy spectrum. The detector (2) is mounted 3″ from the sample, and can be positioned at a desired scattering angle. In all our channeling experiments the detector was positioned so as to give a scattering angle of 105°. The angular spread of the beam at the detector is reduced by mounting a small circular aperture of diameter 0.193″ in front of the detector. The area of the aperture and the distance from the sample to the detector will define the solid angle subtended by the detector which is equal to 0.00306 steradian is our case.

Total number of incident ions

For all channeling measurements, it is necessary to measure the number of incident ions which are striking the surface during the data collection time. The usual way to do this is to measure the incident beam current at the sample and to integrate the current over the time of the spectrum collection. This can be handled nicely by using a current meter and integrator. The number of incident ions is equal to the total integrated charge divided by the charge on one ion. However, the incident high energy ions are capable of producing secondary electron emission from the sample. These outgoing electrons will then be added to the actual beam current. Because of their low kinetic energy (order of 100 eV), emission of these electrons can be suppressed by biasing the sample with a 157 Volt battery as shown in Figure 3.4. Typically our sample mounting

will have a resistance between the sample and ground on the order of 10^5 MΩ. This leads to a leakage current on the order of 10^{-9} A. A typical ion beam current used in these experiments is about $1x10^{-8}$A so an auxiliary circuit, shown in Figure 3.4, is used to correct for the leakage current.

Multichannel analyzer: PHA and MCS modes

Multichannel analyzers provide a variety of functions, including data acquisition, storage, display, and analysis. MCA's are typically used in either of two distinct data analysis modes, the pulse-height-analysis (PHA) mode or the multichannel scaling (MCS) mode. In the PHA mode, a spectrum (histogram) of the frequency distributions of the pulse heights is accumulated from a sequence of input pulses. The desired spectrum is accumulated by 'measuring' the amplitude of each input event, converting it to a number called the 'channel number' that is proportional to the pulse height, and storing the event as a count in a memory composed of individual channels. That is , the x-axis of the screen is proportional to the backscattered ion energy, and the y-axis is proportional to the number of ions backscattered at that energy. The x-axis of the MCA is routinely calibrated by using a calibrated pulse generator. This is done by centering the output pulse for a particular energy, e.g. 1 MeV, at a desired channel number, e.g. 1000. With these settings each channel in the MCA will correspond to 1 keV. The 5.3 MeV alpha particles emitted from a polonium (^{210}Po) radiation source, together with the PIPS detector and the MCA, are utilized to calibrate the pulse generator.

In the MCS mode, individual incoming pulses are counted for a predetermined time interval and placed in a single channel. During subsequent time intervals counting is transferred to the next channel. This mode of operation is used in the alignment of the crystal for the channeling experiments. The XPS spectrum is also collected using this mode.

Goniometer and Sample holder

The sample holder consisted of a Mo block fastened to a three-axis goniometer which also allows for two independent translations[6]. The angular rotations of the sample are controlled using three accurate feed-through shafts with an angular precision of about 0.1°. As discussed before, this high precision goniometer is very important to find the channeling direction precisely and efficiently. The sample holder includes a W filament (0.25mm diameter, 12 turns) for sample heating, a 0.25mm diameter W wire for sample current measurements, and a Pt resistor to monitor the sample temperature during annealing procedure. The Mo block is electrically insulated from the goniometer using quartz rods to allow charge integration during ion scattering experiments. The Al single crystal is mounted on the Mo block such that the rotation and tilt axes are approximately in the plane of the sample surface.

X-ray Photoemission Facility

The components to be considered in our XPS facility include a primary source of X-rays, a sample, an electron analyzer and a detector, all contained within an UHV enclosure and, a computer for data acquisition. In the following sections these components will be described briefly, emphasis being placed on their mode of operation rather than construction.

X-ray source

The choice of anode material for an X-ray source will depend on the energy of the photons required and, to lesser extent, the natural width of the X-ray spectrum. The energy must be high enough to excite an intense photoelectron peak from all elements, but the linewidth must not be so large as to broaden the resultant peak excessively[7]. In practice the materials of choice are aluminum and magnesium. Our XPS facility is fitted with a twin anode x-ray source (VSW TA10) incorporating both aluminum (Al K_α 1486.6 eV) and magnesium (Mg K_α 1253.6 eV) anodes. There are two reasons to use twin anodes in XPS. One, in order to get better energy resolution the magnesium line is preferred. The other reason is that in any x-ray excited electron spectrum both photoelectron and Auger peaks appear, and confusion may result[8]. The Auger electron energy is independent of the X-ray energy, whereas the photoelectron energy depends on the X-ray energy through the following equation:

$$\overline{E}_{kin} = h\nu - E_B . \qquad (3.1)$$

Hence the XPS peak positions will shift by 233 eV (the difference between the Al and Mg binding energies) upon switching the sources enabling the two processes to be differentiated. Water cooling is necessary to prevent the anode from heating up. Furthermore, a small Al window is placed between the sample and the anode to prevent stray electrons from reaching the sample, to reduce the heating effect and to avoid any possible contamination originating in the source region.

Electron energy analyzer

The cornerstone of XPS is the accurate determination of electron binding energies in order to elucidate chemical state information. As the chemical shifts involved may be small (< 0.5 eV), the requirement for an analyzer resolution of this order is self evident. We use a hemispherical analyzer, VSW HA100. The basic idea of operation in this analyzer is that the deflecting electrostatic fields disperse the electron at different energies so that, for any given field, only those energies in a certain narrow range are detected by the detector.

In XPS, it is the spectral resolution that is of paramount importance and it is for this reason that the hemispherical analyzer is operated in the fixed analyzer transmission (FAT) mode. This is achieved by applying a constant voltage across the hemispheres, and accelerating or retarding electrons of a particular energy to the transmission energy. Thus, the resolution is constant across the entire energy range. Pass energies of 10, 25, 50 and 125 eV, and retard ratios of 5, 10, 50 and 100 are allowed. Typically a pass energy of

50 eV is used. A number of scanning rates are also allowed during the measurements. A scan rate of 0.1 eV/sec is used to scan individual peaks, while larger rates are used to scan wider kinetic energy ranges. In addition, the analyzer can be operated with fixed retardation ratio (FRR) throughout the spectrum to maintain a fixed sample area being imaged by the analyzer. The FRR mode is useful when scanning a wide energy range of the spectrum.

Electron detection (channeltron)

The channel electron multiplier (channeltron) is employed for detection of the photoelectrons as shown in Figure 3.5. The channeltron is made out of a curved tube, with a length-to-diameter ratio of about 100:1. The tube is coated with high resistance material, and the surface becomes a continuous dynode. Electrons entering the low potential end of the multiplier cause secondary electrons to be emitted from the tube walls. These electrons are accelerated along the tube causing more secondaries to be emitted. Due to this avalanching process, a large number of electrons is produced at the high potential end of the multiplier. A gain of about 10^8 is obtained. These pulses are then further amplified by a pre-amplifier and transmitted to the multichannel analyzer. The MCS mode is used to record the output signal by collecting the total number of electron pulses in a predetermined time interval. To obtain yield versus energy scans, the XPS control unit is triggered to start, and the PC based acquisition system is set to acquire data simultaneously. The time-to-energy conversion is obtained from the width

of the energy window and the scan rate, both of which are set by the XPS analyzer control unit.

Rear view LEED optics

LEED is the most commonly used technique in the study of single crystal surfaces. Because low energy electrons do not penetrate very far into the surface, i.e., they have a short mean free path, LEED measurements provide information concerning primarily the top layer or two of atoms at the surface. LEED probes the long-range order of a periodic surface structure and also yields valuable information on the disorder and symmetry of the surface structure.

The LEED apparatus (PRI Model RVL 8-120) that we used is shown schematically in Figure 3.6. It consists of four spherical grids which are mounted in front of a spherical collector. The collector is coated with a luminescent layer to display the incoming electrons. A number of diffracted beams emerge in various directions with various intensities from the sample surface and traverse the field free region between the sample and the grounded first grid. The inner two grids act like a high pass filter and allow only the diffracted electrons which have sufficient kinetic energy by their nature to pass through the grids. The advantage of two grids at retarding voltages over one is to smear out inhomogeneities in the electric field produced from the mesh. Double grids give superior energy resolution. The electrons that pass through the grounded fourth grid are then accelerated by the potential on the collector screen. The grounded fourth grid

acts as a shield between the two suppresser grids and the collector screen. The accelerated electrons strike the collector screen and cause phosphorescence which results in the visible LEED pattern. In the PRI Reverse view LEED optics this pattern is viewed from behind the collector screen through a viewport in the center of the mounting flange. It is obscured only by the shadow of the miniature electron gun.

Sample Preparation

Crystal polishing and Orientation

When a particular surface plane of a single crystal, such as the (110) plane of Al, is to be studied it is important that the sample be cut , aligned and polished until the surface is of the desired plane and is shinny and smooth. The as-received, roughly oriented, Al crystal was mechanically polished several times using 400 grit size coated abrasive sheets until the desired orientation was achieved. The Laue diffraction method was used to orient the surface of the crystal with respect to the desired crystallographic direction. The Laue spots from the well oriented Al(110) crystal surface are shown in Figure 3.7.

After the crystal surface is oriented in the desired surface plane, the sample surface is further polished to obtain a smooth, shiny surface. For this fine polishing, solutions (Buehler alpha micropolish alumina) with decreasing particle size were used, starting with 5 micron and finishing with 0.05 micron particle size. Usually the sample is cleaned in deionized water, and chemically etched using a solution containing HCl, HF, and HNO_3, with concentrations of 1.5%, 1.5%, and 2.5% respectively, for 15 seconds.

The chemical etching after polishing removes any damage associated with the mechanical polishing and yields a the shiny, smooth surface before it is mounted into the UHV chamber. To obtain a surface free from any foreign species, the sample must then be cleaned *in situ*.

Crystal cleaning

The samples were cleaned in vacuum by repeated cycles of Ar^+ ion bombardment for several hours with the sample at room temperature, followed by annealing the sample at 520°C for about 15 minutes. A 5keV sputter gun with a raster control unit is used for this purpose. High purity argon gas is slowly leaked into the UHV chamber through a leak valve (25), where these Ar gas molecules are ionized by electron impact. The 1.5kV argon ion beam used in the cleaning cycles was rastered over the entire sample surface. The XPS spectrum of the sample before cleaning exhibited an Al 2p line with a second component corresponding to the oxide (Al_2O_3) at higher binding energy. The two peaks are separated by 2.05eV as shown in Figure 2.11. This is a classic example of the chemical shift that can be observed using XPS. The cleaning procedure was repeated until the photopeak associated with the oxide was completely removed from the spectrum. The O 1*s* photopeak could not be used to monitor the Al surface oxide since the spherical analyzer also samples part of the Mo sample holder. The cleanliness of the sample is confirmed by measuring a surface peak area, in a channeling spectrum, that

agrees with the calculated surface peak area for Al obtained from Monte Carlo simulations of the ion scattering experiment. Details of these simulations and the code (VEGAS) that is used to calculate the surface peak area are described in Ref. 6. Furthermore, LEED was used to confirm the quality and the cleanliness of the sample surface. The clean sharp Al(110) LEED pattern is showed in Figure 3.8.

Locating the channeling direction

The next step after obtaining a clean sample surface is to locate the low index crystallographic directions of the sample. As we discussed in Chapter 2, when the ion beam is aligned along the desired crystallographic direction, the backscattered ion yield from the sample is reduced by about 95% relative to the yield for a random direction of incidence. When the sample is held approximately normal to the ion beam, a small region of interest (ROI) is defined just behind the surface peak in the backscattered ion spectrum. While the incident ion beam is maintained at a constant value, the sample is rotated by about $\pm 5^{\circ}$ with respect to the normal, and the counts from the ROI in the MCS mode of the multi-channel analyzer are monitored simultaneously. The count rate will go through a minimum during this rotation. At this minimum value the ion beam is nearly aligned with the desired low index direction. Then the sample is held at this minimum value and tilted back and forth ($\pm 4^{\circ}$) until the count rate in the ROI passes through another minimum. This procedure is repeated iteratively until the desired channeling direction is established. Most of our experiments were done at normal incidence. In

addition, after we installed the LEED it was helpful to orient the sample azimuthally prior to any channeling location procedure.

Film deposition

For the deposition of thin metallic films, Pd on Al (Chapter 4), Fe on Al (Chapter 5), and Co on Al (Chapter 6), resistive heating was used. Typically three strands of 0.25mm diameter metal wires (99.99% purity) were twisted together and wound into small filaments. A stable DC current supply was used to pass current (about 4 amps) through the wires. The Ag films on Al (Chapter 7) were deposited by heating Ag wire wrapped around a tungsten wire. A higher current of 10 amps was needed to obtain a desirable silver evaporation. The evaporators are far enough away from the sample so that a uniform deposition of material on the sample is obtained. Ion backscattering was used to measure the total metal coverage at different stages of the experiments. Furthermore, during evaporation the chamber pressure increased slightly and analysis of the residual gas showed that this pressure increase was primarily due to residual hydrogen. The sample temperature was also monitored during film deposition using a calibrated Pt resistor. No rise in the sample temperature was seen during deposition of metals. The sample temperature remained at 297K.

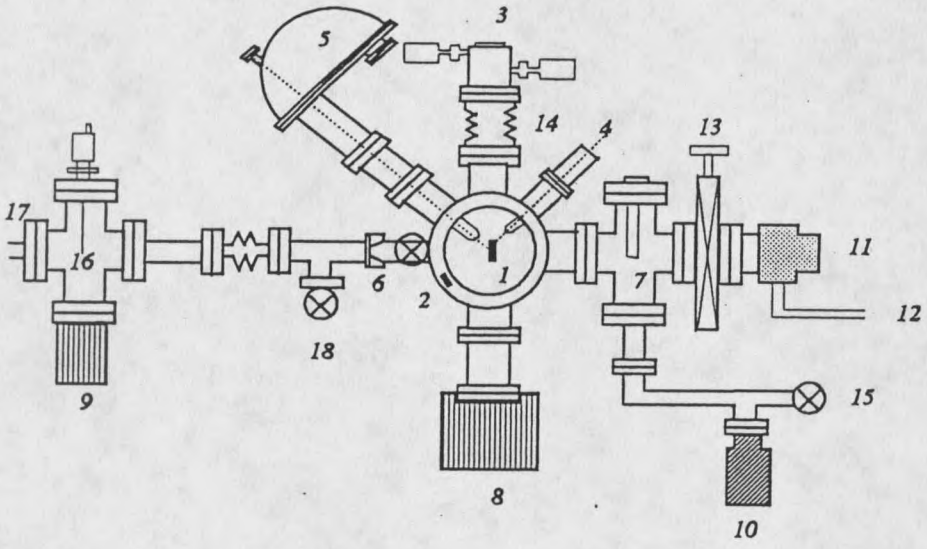

Figure 3.1: Side view of the UHV chamber.

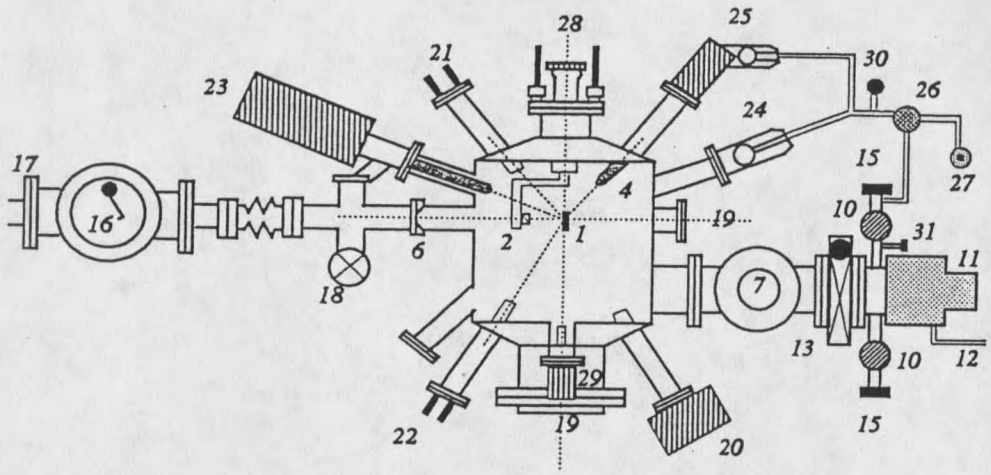

Figure 3.2: Top view of the UHV chamber.

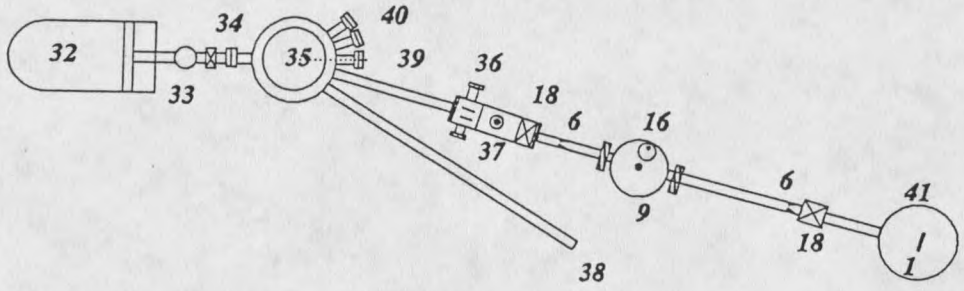

1. *Sample*
2. *Detector*
3. *Goniometer*
4. *Ion (sputtering) Gun*
5. *Hemispherical Analyzer*
6. *Collimating Slits*
7. *Ti Sublimation pump*
8. *Ion pump - Chamber*
9. *Ion pump - Beam line*
10. *Sorption pump*
11. *Turbo pump*
12. *Forline pump*
13. *Gate Valve*
14. *Bellows*
15. *Leak line Valve*
16. *Beam Blocker*
17. *Ion beam line*
18. *Valves*
19. *Glass Window*
20. *Residual Gas Analyzer*
21. *Ni Filament*
22. *Pd Filament*
23. *X-ray Gun*
24. *Leak Valve*
25. *Ion Gun Leak Valve*
26. *Gas Reservoir*
27. *Ar/H/O Gass Bottles*
28. *Detector Arm*
29. *Nude Ion Gauge*
30. *Valves*
31. *Vent Valve*
32. *Accelerator*
33. *Diffusion pump*
34. *Gate Valve*
35. *Bending Magnet*
36. *Stabilizing Slits*
37. *Ion Beam Viewer*
38. *RBS Beam line*
39. *Stright through Blocker*
40. *Extra Beam lines*
41. *UHV Chamber*

Figure 3.3: Schematic drawing of the Van de Graaff accelerator, beam line setup, and the UHV chamber.

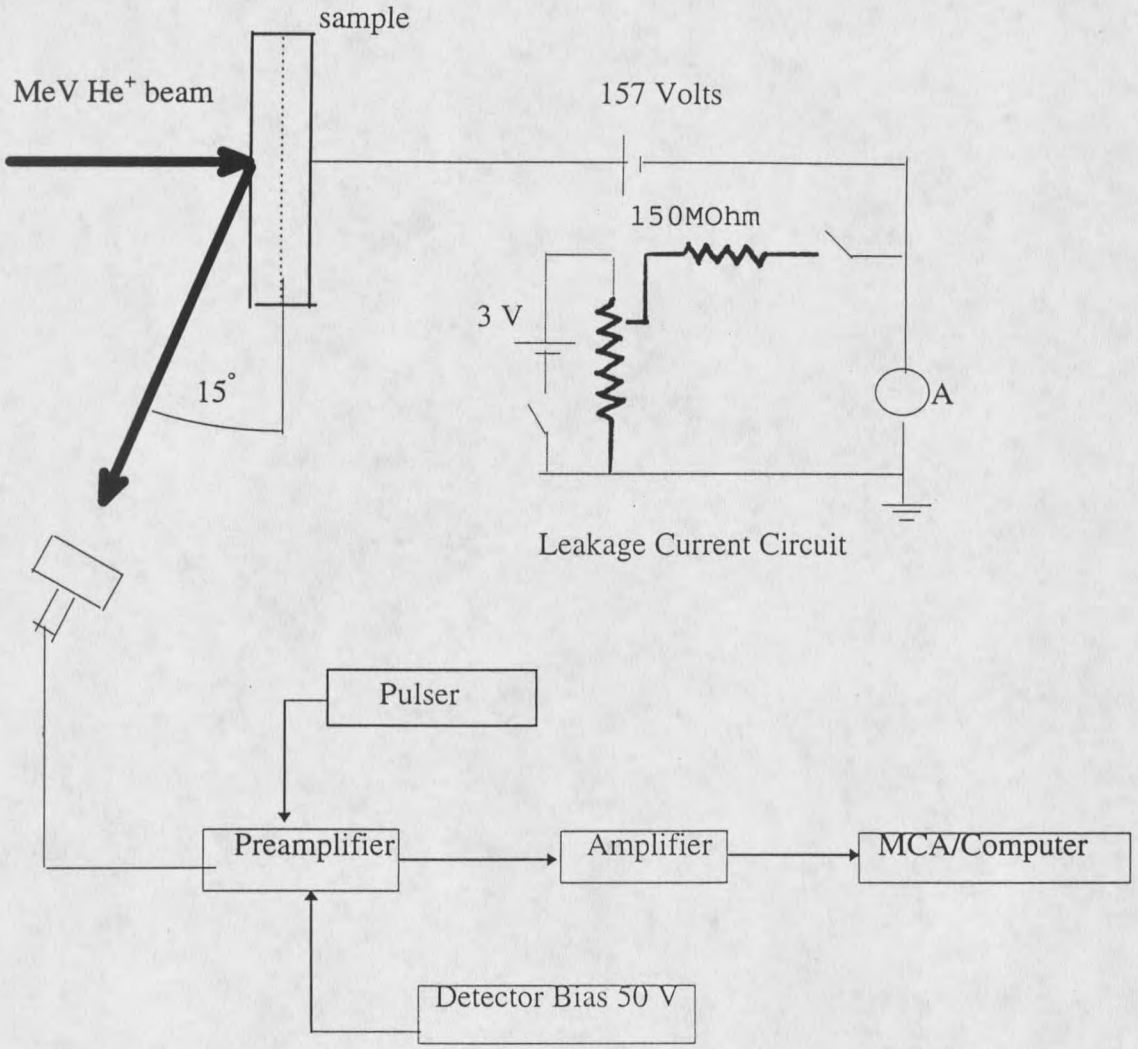

Figure 3.4: Schematic diagram of the HEIS/RBS data acquisition including - secondary electron suppression circuit, and the leakage current compensation circuit.

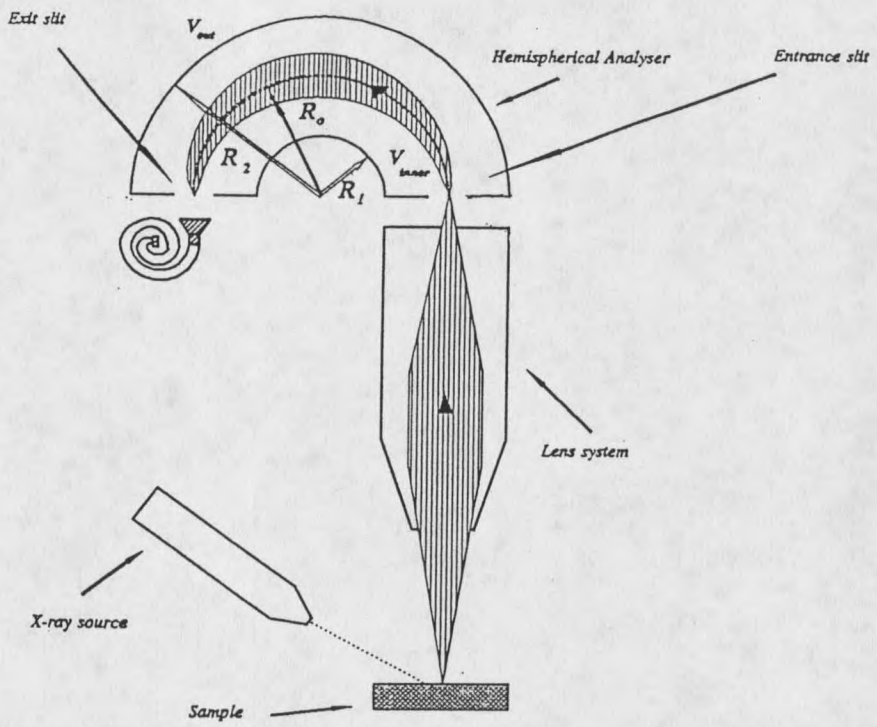

Figure 3.5: Schematic of X-ray photoelectron spectroscopy. Incoming x-rays excite the bound electrons in the sample. A hemispherical analyzer is used to measure the electron kinetic energy. The potential difference between the outer and inner sphere is related to the kinetic energy of the detected electrons (E_k).

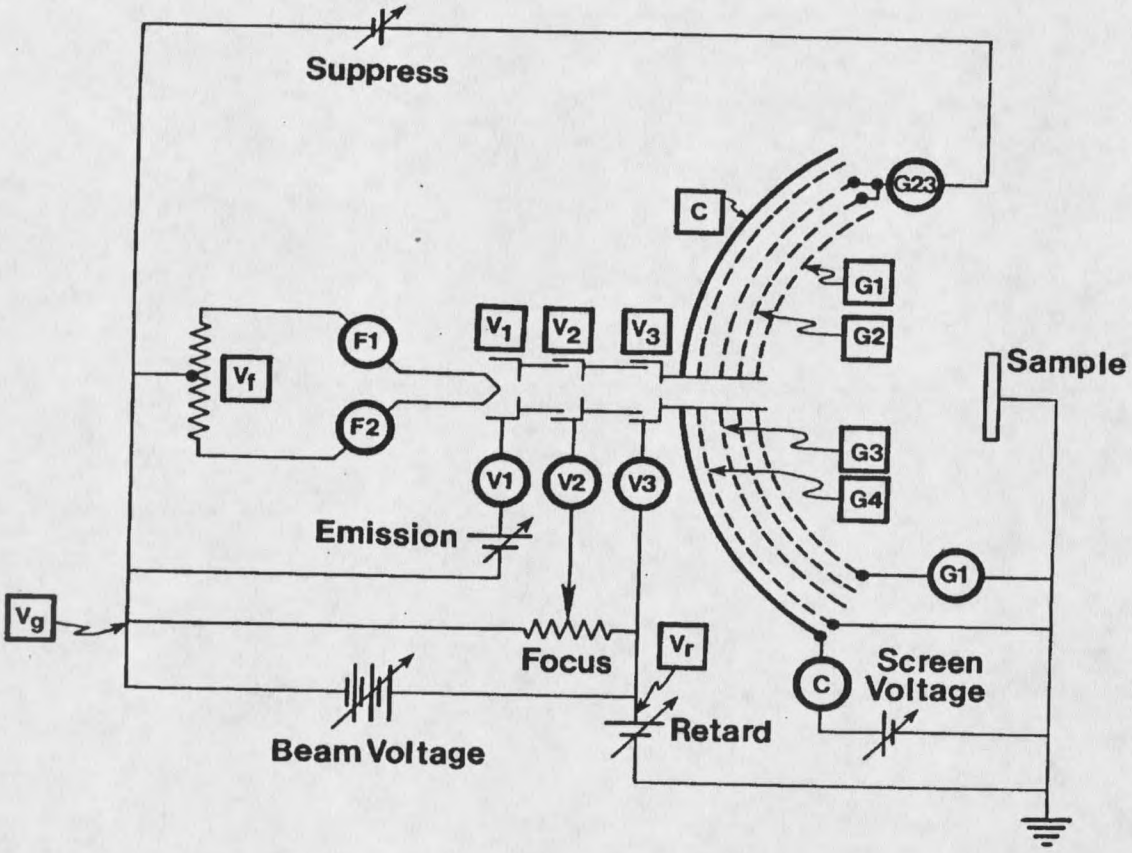

Figure 3.6: Schematic of LEED apparatus.

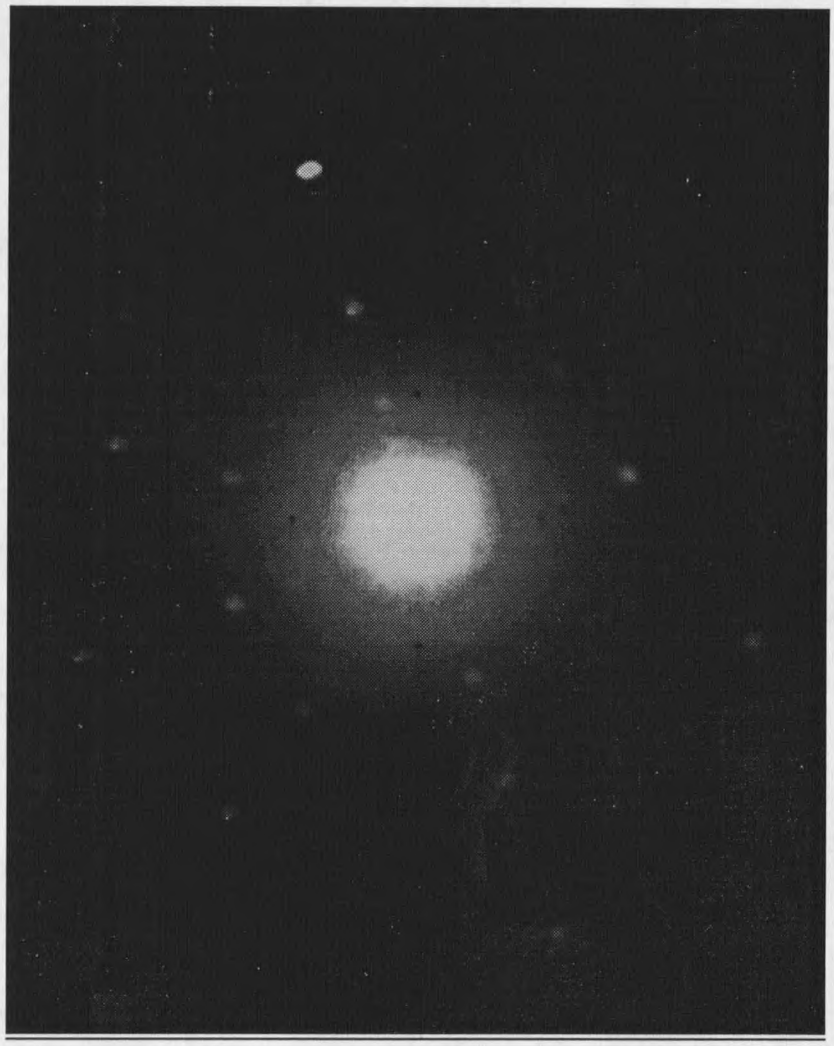

Figure 3.7: The Laue diffraction pattern from Al(110) single crystal surface.

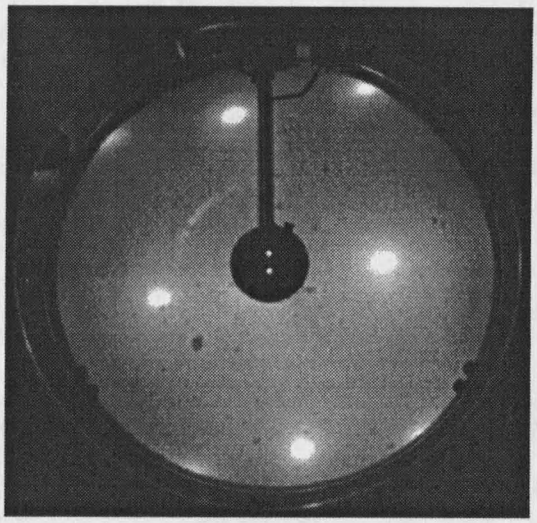

Figure 3.8: LEED image of the clean Al(110) single crystal surface taken at 46.8eV incident electron beam.

REFERENCES

1. *Surface Analysis Methods in Materials Science*, Edited by D.J. O'Connor, B.A. Sexton, R.St. C. Smart, Springer Series in Surface Sciences 23, 1992.
2. R.J. Smith, C.N. Whang, Xu Mingde, M. Worthington, C. Hennnesy, M. Kim, and N. Holland, Rev. Sci. Instrum., 58, (12), 2284(1987).
3. J.W. Mayer, and E. Rimini, Ion Beam Hand Book for Material Analysis (Academic Press, New York, 1977).
4. L.C Feldman, J.W. Mayer, and S.T.Picraux, Materials Analysis by Ion Channeling (Academic Press, New York, 1982).
5. L.C. Feldman, and J.W. Mayer, Fundamentals of Surface and Thin Films Analysis (North-Holland, Amsterdam, 1986).
6. V. Shutthanandan, Ph.D Thesis, Montana State University, 1994.
7. *Surface Science Techniques*, Edited by J.M. Walls, and R.Smith (Pergamon, New York, 1994).
8. C.D. Wagner, W.M. Riggs, L.E. Davis, J.F. Moulder, and G.E. Muilenbergr, Hand Book of X-ray Photoemission Spectroscopy.
9. J.M. Walls, Methods of Surface Analysis (Cambridge University Press, New York, 1990).
10. J.W. Franken, R.M. Tromp, and J.F. van der Veen, NIM, B17, 334(1986).

CHAPTER 4

ROOM TEMPERATURE GROWTH OF THIN Pd FILMS ON Al(110) SURFACES

Introduction

Understanding the formation of the solid-solid interface between thin films of transition metals and aluminum has been an important goal of surface science in recent years because of the potential use of the transition metal aluminides in applications ranging from light-weight high-temperature structural materials[1], to metallization layers on III-V semiconductors[2], to modified catalytic properties of supported thin films[3]. In particular, the modified electronic properties of supported thin Pd films on a variety of metal substrates have been studied to determine the role of the substrate electronic structure in modifying the properties of the overlayer[4].

Using medium energy ion scattering (MEIS), Smith and coworkers[5] have shown that alloy formation occurs when Pd films are deposited on Al(111) surfaces. Their results suggest that an AlPd compound grows on the substrate up to a coverage of about 5 monolayers (ML). There is no long-range order in this alloy, based on the fact that the low energy electron diffraction (LEED) pattern vanishes after only 0.5 ML of Pd deposition. However, a poorly developed Pd(111) LEED pattern, epitaxially aligned with the Al(111)

substrate, does return after 8 ML of Pd deposition, suggesting that there is sufficient short-range order in the AlPd alloy to grow Pd(111) on the surface of the alloy. Shutthanandan and coworkers recently reported a study of Pd film growth on Al(100) surfaces[6]. Using high energy ion scattering (HEIS) they observed a strong intermixing of Pd and Al atoms which continued up to about 5 ML in the form of AlPd before Pd metal started growing on the interface. In these experiments x-ray photoemission spectroscopy (XPS) was used to identify the formation of the AlPd-like alloy based on the chemical shift of the Pd 3d core electrons. Since we are interested in how film growth might depend on substrate orientation, it is interesting to consider Pd film growth on the Al(110) surface. Some early measurements by Smith and coworkers[5] used MEIS to characterize Pd growth on Al(110). While the growth of AlPd is observed for both (100) and (111) Al surfaces, with termination of alloy growth around 5 ML of Pd coverage, the early MEIS results suggested that a different stoichiometry was occurring in the growth on (110) surfaces, possibly Al_2Pd[5]. The (110) surface is more open than the other two surfaces, so more intermixing might be anticipated, leading to a more Al-rich compound. Thus it seemed appropriate to study the Pd-Al(110) system with HEIS and XPS to better characterize the alloy formed on this surface.

In this chapter we report the results of high energy ion backscattering and channeling experiments which show substantial disruption of the Al(110) single crystal surface following deposition of Pd atoms. X-ray photoemission measurements confirm a

large chemical shift of the Pd 3d core level, consistent with the formation of an AlPd-like compound. The intermixing at room temperature stops when approximately 10 ML of Pd have been deposited on the surface, and Pd metal grows on the alloy at the interface.

Experimental setup

The experiments were performed in an ultrahigh vacuum (UHV) surface analysis chamber which included facilities for Rutherford backscattering spectroscopy and x-ray photoelectron spectroscopy. The chamber is connected to a 2-MV Van de Graaff accelerator through a differentially pumped beam line[7]. After baking the chamber, a pressure of 8×10^{-11} Torr was obtained using a turbomolecular pump, an ion pump and a Ti sublimation pump. The chamber is equipped with a quadrupole gas analyzer to monitor residual gas composition during the experiment. A bakeable solid state detector, installed on a rotatable arm 3.0" away from the sample, was used to collect the backscattered He^+ ions. The detector was positioned at a scattering angle of 105°. The sample holder consisted of a Mo block fastened to a three-axis goniometer, and included an integral tungsten filament for heating the Mo block and sample, and a Pt resistor mounted in the Mo block for monitoring the sample temperature. The Mo block is electrically insulated from the sample goniometer for the purpose of measuring beam currents during the experiments. Charge integration during channeling measurements was accomplished using a +157 V sample potential relative to the chamber (ground potential) to suppress the emission of most

of the secondary electrons. All channeling measurements were made with the sample at room temperature.

The Al single crystal used in this study was cut with its surface approximately parallel to the (110) plane. This surface was then mechanically polished and oriented using the Laue x-ray method. This procedure was repeated until the finished shiny, smooth surface was within 0.5° of the (110) orientation. The samples were then chemically etched for 15 seconds and mounted in the UHV system. The samples were cleaned in UHV using Ar^+ ion beam bombardment. The surfaces were sputtered with 1500 eV ions for several hours, followed by annealing at 520° C for 20 minutes. This cleaning procedure was repeated until the oxide component in the Al 2p XPS photopeak was removed from the spectrum. The Pd films were evaporated onto the Al($\bar{1}$10) surfaces at room temperature using a wire evaporation source. The source consisted of a twisted, triple strand of 0.25 mm diameter Pd wire (99.997% purity), and a regulated direct current power supply.

A collimated beam of 0.96 MeV He^+ ions passing through a 1 mm diameter aperture was used to carry out the high energy ion scattering experiments. The samples were aligned for channeling by using the ion beam and minimizing the backscattered ion yield behind the Al surface peak. A backscattering measurement with the ion beam aligned along the (110) direction was made after each Pd deposition. A total integrated charge of 3 μC (1.56×10^{15} ions/cm^2) was used to collect each spectrum. A deposition rate of about 0.5 ML/min was obtained by maintaining a direct current of 4.25 A through the Pd wire. A random

alignment ion backscattering spectrum was also measured occasionally to verify that no Pd-Pd shadowing was affecting the measured total Pd coverage at the different stages of the experiment. The uncertainty in the HEIS results presented here is estimated to be 5.6%, with the largest contribution to the uncertainty coming from the determination of the detector solid angle, and a smaller contribution coming from the uncertainties in the integrated charge, the scattering angle, and the determination of the surface peak area of the backscattered ion spectra.

The XPS spectra were recorded using a 100 mm hemispherical analyzer in a fixed-analyzer-transmission mode with a pass energy of 50 eV, and a scan rate of 0.1 eV/sec. A Mg K_α (1253.6 eV) X-ray source with 200 W power was used to generate x-rays. For XPS measurements the sample was kept in the channeling alignment, and the photoelectrons entered the analyzer with a polar angle of 30° from the sample normal.

Results

High-energy ion scattering

Fig. 4.1 shows the energy distribution of backscattered ions in the regions of the Al and Pd surface peaks for several Pd coverages. Each curve in the figure is identified by the Pd coverage as determined by ion scattering. One monolayer (ML) here is equivalent to the atomic density of the Al(110) plane, 0.8622×10^{15} atoms/cm^2. The arrows and the dashed lines in the figure indicate the energetic positions of the surface Al and Pd atoms. It can be

seen from the figure that the Al surface peak area increases with Pd coverage. This suggests that more Al atoms are visible to the incoming ion beam when Pd atoms are present on the surface. That is, surface Al atoms have moved from their initial equilibrium positions and have reduced the shadowing of substrate Al atoms. On the other hand, if Pd atoms formed a commensurate overlayer directly above the Al atoms then we would expect the Al surface peak area to be reduced because of Pd shadowing of Al atoms, as seen for Ti deposition on Al(110)[8]. If Pd atoms formed an incommensurate overlayer the Al surface peak area would remain constant as the Pd coverage increased, similar to the behavior reported for Ni deposition on W(110)[9]. In Fig. 4.2 we plot the number of Al atoms/cm^2 visible to the incident ion beam, obtained from the Al surface peak area, as a function of Pd coverage, determined by the Pd surface peak area. The Al(110) surface density of 0.8622×10^{15} atoms/cm^2 per monolayer was used to convert the Pd coverage into equivalent Al(110) monolayers. Such plots can be useful for developing reasonable models for the mixed interfaces, as demonstrated by us and others[10,11,12]. As shown in Fig. 4.2, there appear to be two distinct growth regimes. First, the Al surface peak area increases with an approximate slope of 1.2 Al atoms per deposited Pd atom, up to about 10 ML of Pd coverage. At this coverage there is an apparent saturation point beyond which the Al surface peak area remains unchanged. To check for possible shadowing of surface Pd atoms, the ion beam was made incident in a random direction, slightly away from the normal channeling direction.

Fig 4.3 is a plot of the number of Pd atoms visible to the ion beam in the channeling direction (open circles) versus the actual Pd coverage, obtained from the measurement for a random direction of incidence (solid circles). We did not see any significant reduction in the number of visible Pd atoms, indicating that there is no Pd-Pd or Al-Pd alignment normal to the Al(110) surface.

X-ray photoelectron spectroscopy

Fig. 4.4 is a plot of the x-ray photoelectron energy distribution curves, after background subtraction, for the Pd $3d_{5/2}$ and Pd $3d_{3/2}$ photopeaks for three different coverages of Pd on Al(110). The solid curves through the data are the results from the peak shape analysis discussed in the appendix. The arrows in the figure indicate the photopeak positions for the AlPd alloy and Pd metal from Ref. 13. The spectra have been shifted vertically in order to compare the energy distribution curves. It is clear in the figure that the line shape of the Pd peaks change as the Pd coverage increases.

Discussion

The results of Figs. 4.1 and 4.2 show that more and more Al atoms become visible to the incident ion beam as the Pd coverage increases up to 10 ML. This suggests that Pd atoms are mixing with Al atoms on the Al(110) surface. In a standard interpretation of these results, the slope for ion scattering yield versus Pd coverage is used to determine the

average stoichiometry of the mixed interface. In this case, the slope of 1.2:1 could indicate that AlPd is forming, somewhat rich in Al. That is, approximately one Al atom is displaced for every Pd atom that stays on the surface. This interpretation is not always reliable as we illustrated in the case of Ni on Al(110), where a contribution to the slope was attributed to near-surface dechanneling[14]. However, with the additional information obtained from XPS, as discussed below, we conclude that an AlPd compound is forming on the surface up to about 10 ML of Pd coverage. It is reasonable to think that AlPd will be the first phase to form at the Al-Pd interface. Since AlPd has a very large heat of formation, -92 kJ/mol, it is the most stable phase in the Al-Pd phase diagram, and it has the relatively simple CsCl structure[15]. In previous studies of Pd on Al(111)[5], and Pd on Al(100)[6], the authors reported that an AlPd-like compound is the initial reaction product on those surfaces. For Al(110), the authors of Ref. 5 reported a slope of 1.8 Al atoms per deposited Pd atom, measured with medium energy ion scattering. While the differences in measured slopes might be attributed to various energy dependent mechanisms, there is agreement among these studies that all three surfaces exhibit considerable Al-Pd mixing.

For Pd coverages larger than 10 ML in Fig. 4.2, the zero slope of Al backscattered ion yield versus Pd coverage suggests that additional deposited Pd atoms do not affect the position of Al atoms. This can be taken as an indication that after 10 ML of Pd coverage the intermixing at the interface stops and a Pd metal film is forming on the surface. The results of Fig. 4.3 indicate that there is no significant Pd-Pd or Al-Pd shadowing, so the

AlPd overlayer and Pd metal film are apparently not well aligned, even if they are ordered with respect to the Al(110) substrate. Furthermore, our observations are not consistent with a Stranski-Krastanov growth mode for Pd on Al(110)[4] since this would result in Pd-Pd shadowing as the islands of Pd grow on the surface, and fewer Al atom displacements.

The channeling results by themselves are not sufficient to justify our suggestion of the formation of AlPd at the interface so we look at the XPS results. Fuggle and co-workers have studied in detail the chemical shifts of the Pd 3d photopeaks in various Al-Pd bulk alloys[13]. They observed a large chemical shift of the Pd 3d photopeak, on the order of 2 eV towards higher binding energies, in the alloys. We have used their observations to characterize the chemical environment of the Pd atoms at the Al-Pd interface. Fig. 4.4 shows a detailed peak shape analysis of the Pd 3d XPS photopeaks at three different Pd coverages. More details about the fitting procedure can be found in Ref. 6. Briefly, a cubic background is subtracted from the original spectra. Then two pairs of Gaussian line shapes, with the same peak width, were fit to the photopeaks, one pair attributed to Pd metal and the other to the Al-Pd mixture. We allowed the peak amplitudes and positions to vary in the fitting procedure. The dashed lines and the dotted lines are the results of the curve fitting.

Fig. 4.4 shows the evolution of the Pd photopeak shape as a function of Pd coverage on the Al(110) surface. At 1.18 ML of Pd coverage, the Pd $3d_{5/2}$ and Pd $3d_{3/2}$ peaks are centered near 336 eV and 341 eV, respectively. However, at 12.18 ML of Pd coverage, the spectra displays peaks near 335 eV and 340 eV, respectively. These shifts in the Pd peak

are caused by the change in the chemical environment at the interface as the Pd coverage increases. The peaks for 1.2 ML of Pd are attributed to Pd photoelectrons coming from Pd atoms in AlPd, based on the similarities of binding energies to those reported in Ref. 13, and summarized in Table 1. Photopeaks characteristic of elemental Pd metal are seen for the larger Pd coverages. In fact, even at the low Pd coverages the fitting suggests that there is a small Pd peak which can be attributed to Pd metal. This occurs because our photoelectron analyzer is imaging a portion of our Mo sample holder as well as the Al crystal. During Pd deposition, elemental Pd is deposited on the Mo holder also, resulting in the metallic Pd XPS signal. The Pd metal on the Mo sample holder appears to have little or no chemical shift relative to Pd metal.

The results from Ref. 13 are summarized and compared with our results in Table 1. We see very good agreement for the values of the separation of the Pd $3d_{5/2}$ and Pd $3d_{3/2}$ peaks, and for the values of the chemical shift between the Pd 3d peaks in the mixture of AlPd and Pd metal. In our case the chemical shift is about 1.8 eV whereas Ref. 13 gives a value of 1.9 eV. Furthermore, the possibility of forming Al_3Pd can be ruled out because of the large (2.5 eV) chemical shift which differs significantly from our value of 1.83 eV. In Ref. 13 the XPS spectra were collected from bulk Al-Pd alloys, while our results are for very thin films of AlPd. This may explain some of the differences in Table 1 since the amount of charge transfer from Pd to Al may be slightly different for these thin films than for a homogeneous bulk alloy.

In Figure 4.5 we plot the area of the fitted XPS Pd $3d_{5/2}$ peaks as a function of Pd coverage, measured using ion scattering. The open circles denote the emission intensities presumed to originate from the AlPd mixture while the solid circles denote the emission for elemental Pd. Initially, the intensity originating from the alloy increases smoothly with increasing coverage up to about 8 ML. Then the photoemission intensity begins to decrease. At the same time, the Pd metal photoemission intensity increases linearly with Pd coverage up to about 7 ML, and then begins to increase more rapidly. From these observations it is clear that there is a change in the character of the film beginning at about 7 ML of Pd coverage. The initial increase that we see in the Pd metal intensity up to about 7 ML of Pd coverage is attributed to the Pd signal coming from the Pd deposited on the Mo sample holder. On the other hand, the increase seen in the Pd signal originating from AlPd is attributed solely to Pd on the Al crystal. Since the ion scattering results show that there are no further displacements of Al atoms after 10 ML of Pd coverage, we conclude that the interface mixing has completely stopped after 10 ML, and metallic Pd continues to grow on the mixed interface. This is consistent with the rapid increase observed in the Pd metal XPS intensity, as well as the attenuation observed for the XPS intensity from the AlPd mixture.

To better characterize the photoemission signals originating from the sample, we have attempted to subtract out the contribution to the XPS signal originating from the sample holder. We assumed that the intensity from the sample holder has not saturated

during the experiment and instead increases linearly with the Pd coverage. This assumption seems reasonable since the amount of Pd deposited in these experiments is small, and the attenuation length for photoelectrons with kinetic energies around 1000 eV is quite large. Figure 4.6 shows the corrected XPS intensities from the Pd and the mixture of AlPd after subtracting the linear increase in the Pd intensity from the total Pd metal intensity. This subtraction process has no effect on the mixed AlPd since this signal is coming only from the mixed phase on the Al(110) surface. A similar analysis was done for the Pd $3d_{3/2}$ peak as well. Hence, the XPS peak shape analysis supports the growth model suggested by the ion scattering results. Based on the above observations, we conclude that a mixture of AlPd is formed at the Pd-Al(110) interface, and is gradually covered by Pd metal.

Three final points can be made regarding the ion scattering results in Fig. 4.1. First, we note that the energy of the Al surface peak does not change for Pd coverages up to 3 ML. However, there is an apparent shift of the peak in the spectrum for 8 ML. We attribute this apparent shift to the increased number of visible Al atoms within the thickness of the AlPd interface. This additional backscattering below the surface broadens the surface peak on the low-energy side, and gives the appearance of a peak shift. Note that the leading edge of the Al surface peak has not shifted significantly.

The second point concerns the amount of diffusion of Pd into the Al(110) surface at room temperature. The spectrum for 8 ML of Pd in Fig. 4.1 shows a significant amount of backscattering yield trailing off to the low energy side of the peak. These counts represent

the backscattered ion yield from Pd atoms which have diffused into the surface. Even for 3 ML of Pd there is a small amount of diffusion observed. The tail seen for the 8 ML spectrum in Fig. 4.1 corresponds to approximately 1.4 ML of Pd distributed over a depth of about 630 A. This relatively large amount of diffusion was *not* observed in the case of Pd on Al(100)[6]. The diffusion may be a consequence of the fact that the Al(110) surface is more open than that of Al(100). The 8 ML spectrum in Fig. 4.1 also shows that the minimum yield behind the Al surface peak has increased relative to the value at lower coverages. This may be a consequence of the disordered AlPd at the interface as well as the diffused Pd, both of which lead to dechanneling of the incoming He ions and increased backscattered ion yield.

A final point concerns the Pd coverage at which the displacement of substrate atoms ceases for the two Al surfaces which we have studied. We observed that for room temperature deposition of Pd on Al(110) the Al-Pd intermixing terminates at a coverage of 8.62×10^{15} atoms/cm^2, while for Pd on Al(100) the interface mixing ceases at the lower coverage of 6.7×10^{15} at/cm^2. These areal densities correspond to 10 Al(110) ML and 5.5 Al(100) ML, respectively. A very similar behavior was observed for Fe deposition on these two Al surfaces as well[11](see Chapter 5). The differences for the two surfaces may be associated with the more open structure of the (110) surface, or with the relatively high surface energy of the (110) surface, which could contribute to the driving force for diffusion.

Conclusion

We have performed an ion scattering investigation, combined with x-ray photoelectron spectroscopy, of Pd films deposited on Al(110) surfaces at room temperature. The results are not consistent with the layered growth models reported previously for this system[4]. Instead we observe the continued displacement of substrate Al atoms for depositions up to about 8.62×10^{15} atoms/cm^2 (10 ML), indicating a strong intermixing at the surface, followed by the growth of a Pd metal film on the mixed interface. Also a significant amount of Pd diffuses into the Al substrate at room temperature. XPS measurements of the Pd 3d photopeaks show a chemical shift that is consistent with the formation of an AlPd-like compound during the initial growth regime, and Pd metal thereafter. The measured XPS intensity variations support this two-stage growth model.

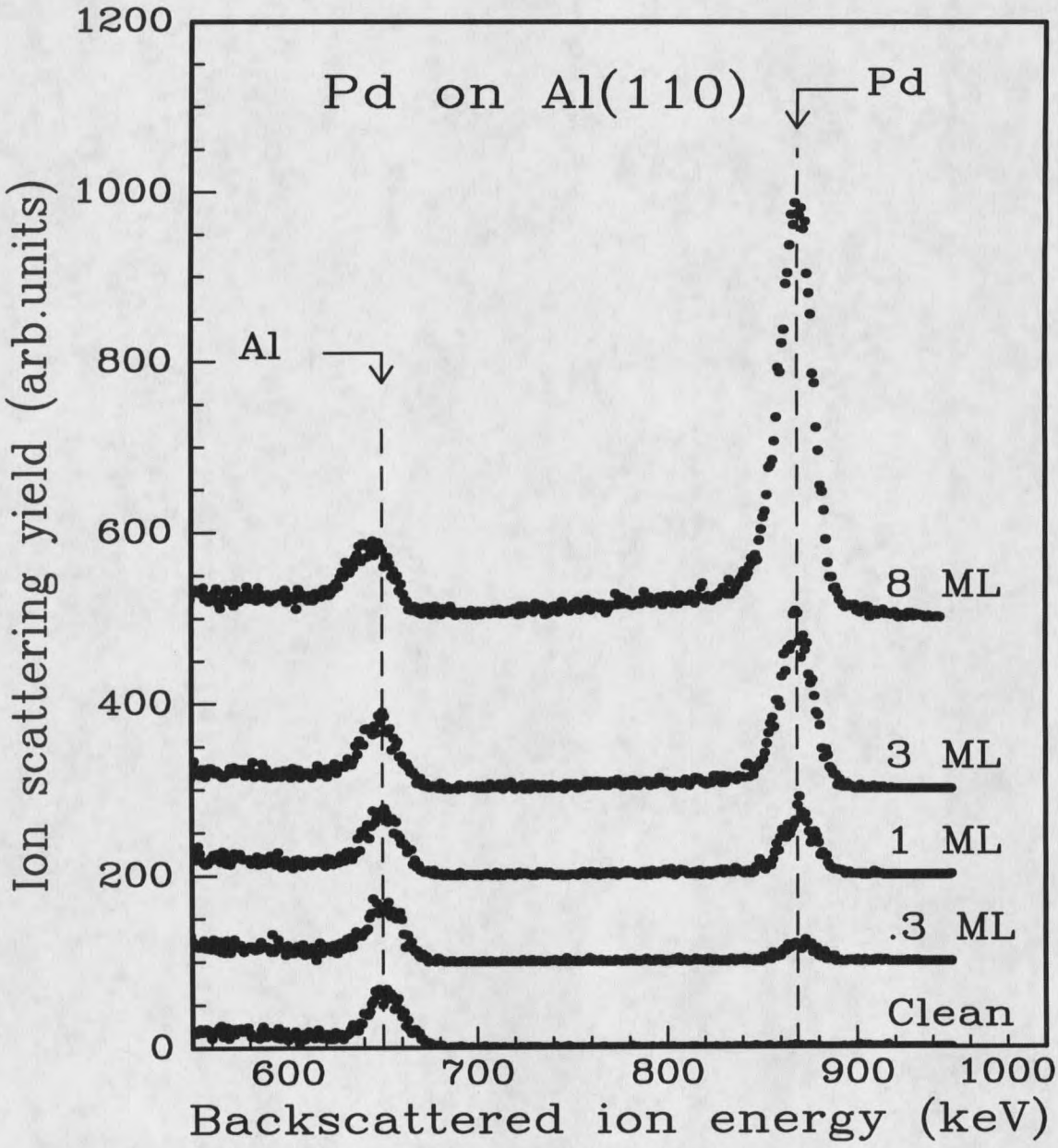

Fig. 4.1: Backscattered ion spectra for 0.96 MeV He^+ ions incident on Pd + Al(110) for different Pd coverages as indicated in the figure. The energetic positions of the Al and Pd surface peaks are indicated by the arrows and the dashed lines.

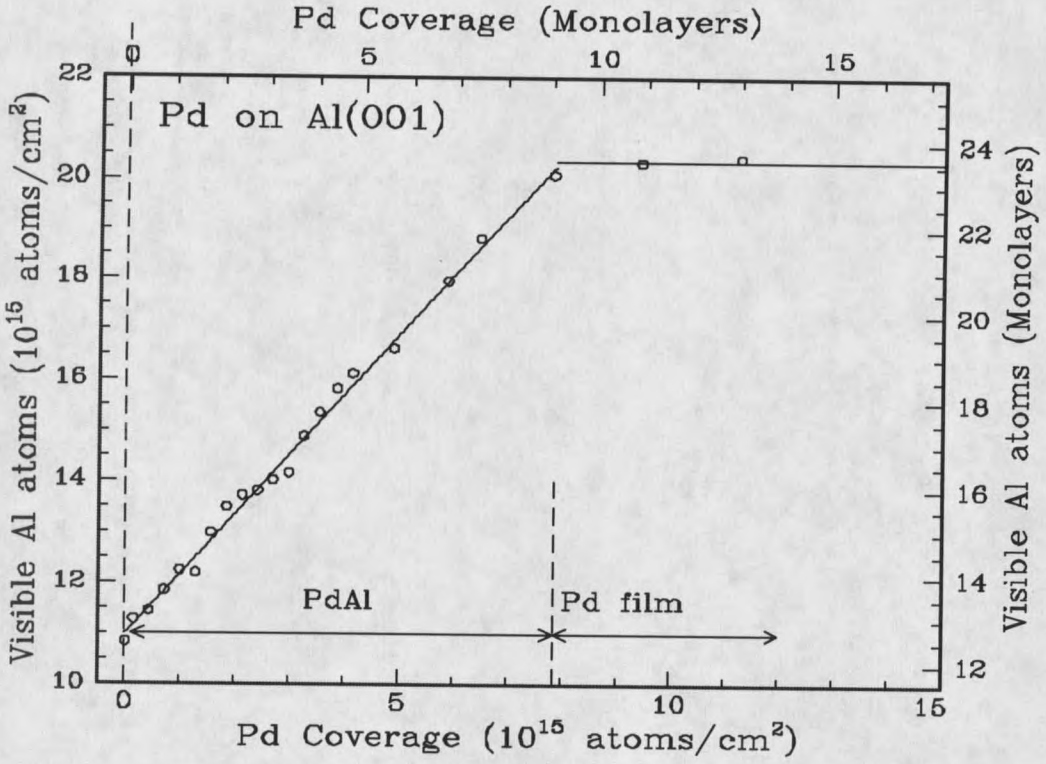

Fig. 4.2: Number of Al atoms visible to the incident ion beam as a function of Pd coverage on the Al(110) surface. The solid lines are the least-squares fit to the data points in two regions. Two stages of film growth are indicated.

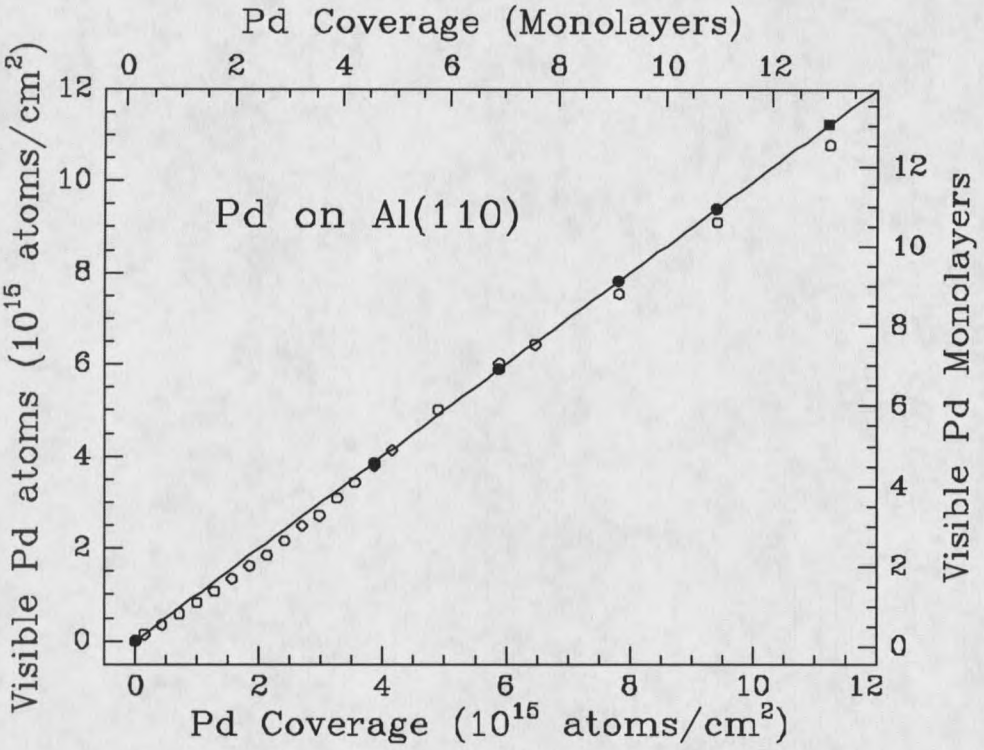

Fig. 4.3: Number of Pd atoms visible to the incident ion beam as a function of Pd coverage. The solid circles are for a random ion incidence direction, while the open circles are for the [110] channeling direction. The solid line is the least-squares fit to the random incidence direction data.

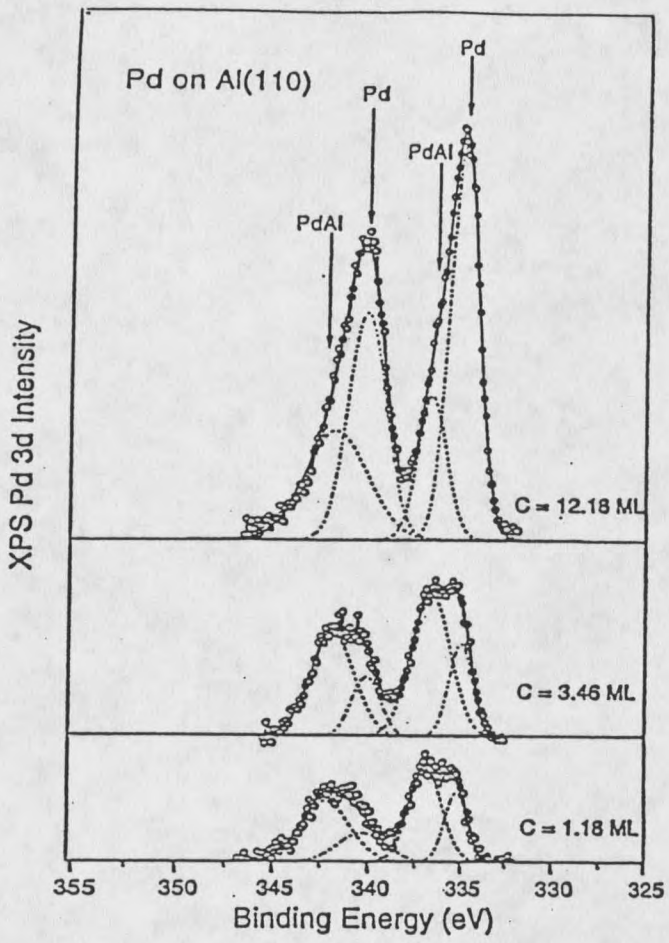

Fig. 4.4: Pd 3d XPS spectra from Pd films deposited at room temperature on the Al(110) surface for three different Pd coverages. The solid curves are the results of the XPS peak fittings. The dashed lines represent Pd photoelectrons coming out from the interface mixture of AlPd, while the dotted lines represent the Pd photoelectron coming from Pd metal. Expected peak positions for the AlPd mixture and for Pd metal are indicated by the arrows.

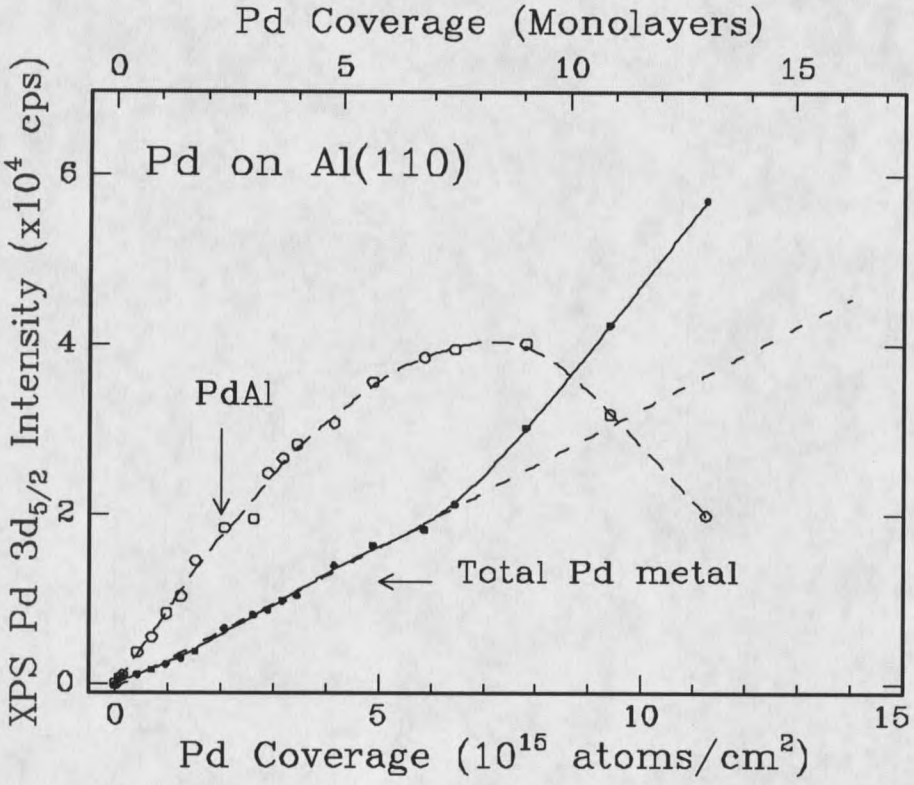

Fig. 4.5: Measured XPS intensity for the Pd $3d_{5/2}$ photopeak as a function of Pd coverage. The open circles (dashed line) show the intensity of the Pd photoelectrons originating within the AlPd mixture. The solid circles (solid line) show the intensity of the Pd photoelectrons originating from both the sample and the sample holder. The extrapolated background Pd metal signal attributed to Pd metal on the sample holder is shown by the dash-dot line. The lines are provided to guide the eye.

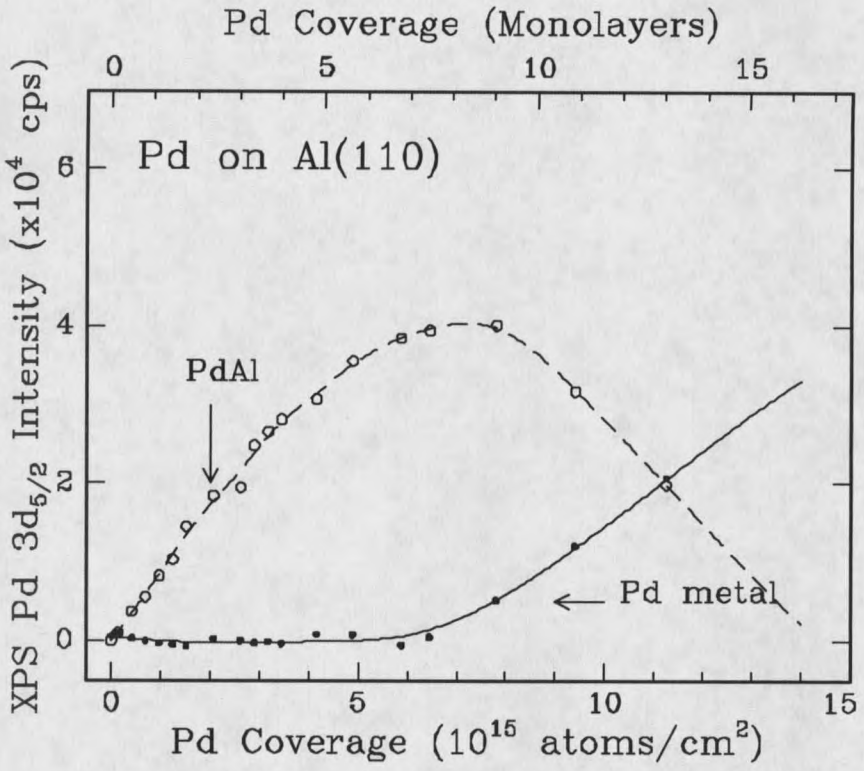

Fig. 4.6: Measured XPS intensity from Pd $3d_{5/2}$ peak as a function of Pd coverage. The open circles (dashed line) show the intensity of the Pd photoelectrons coming out from the mixture of AlPd. The solid circles (solid line) show the emission intensity of the Pd metal photoelectrons originating *only* from the sample.

Table 1

Compound	**Binding Energy 3 d $_{5/2}$ (eV)**	**Binding Energy 3 d $_{3/2}$ (eV)**	**Chemical Shift (eV)**	**Separation between 3 d $_{5/2}$ - 3 d $_{3/2}$ (eV)**
Pd metal (Ref.13)	335.2	340.45	--	5.25
Pd metal (this work)	335.03	340.23	--	5.20
AlPd (Ref 13)	337.05	342.35	1.90	5.30
AlPd (this work)	336.83	342.03	1.80	5.20
Al_3Pd (Ref 13)	337.70	342.90	2.50	5.20

Comparison of binding energies , chemical shifts and peak separation for the Pd $3d_{5/2}$ and $3d_{3/2}$ photopeaks in different Al-Pd alloys. The chemical shifts are averaged over both 3d lines for the purpose of comparing with Ref. [13].

REFERENCES

1. C. C. Koch, C. T. Liu and N. S. Stoloff, Eds., High-Temperature Ordered Intermetallic Alloys, Materials Research Society Symposium Proceedings, Vol 39, MRS, Pittsburgh, PA, 1985.
2. J. P. Harbison, T. Sands, N. Tabatabaie, W. K. Chen, L. T. Florez and V. G. Keramidas, Appl. Phys. Letters 53 (1988) 1717.
3. D. M. Zehner and D. W. Goodman, Physical and Chemical Properties of Thin Metal Overlayers and Alloy Surfaces, Materials Research Society Symposium Proceedings, Vol 83, MRS, Pittsburgh, PA, 1985.
4. M. Xu and R. J. Smith, J. Vac. Sci. Technology, A6 (1988) 736, and references therein.
5. R. J.Smith, A. W. Denier van der Gon and J. F. Van der Veen, Surf. Sci., 233 (1990) 103.
6. V. Shutthanandan, Adli A. Saleh, N. R. Shivaparan, and R. J. Smith, Surf. Sci., 350 (1996) 11.
7. R. J. Smith, C. N. Whang, Xu Mingde, M. Worthington, C. Hennessy, M. Kim, and N. Holland, Rev. Sci. Instrum., 58(12) (1987) 2284.
8. Adli A. Saleh, V. Shutthanandan, and R. J. Smith, Phys. Rev. B 49 (1994) 4908.
9. Xu Mingde and R. J. Smith, J. Vac. Sci. Technol. A9 (1991) 1828.

10. V. Shutthanandan, Adli A. Saleh and R. J. Smith, J.Vac.Sci.Technol, A1 (1993)1780.

11. N. R. Shivaparan, V. Shutthanandan, V. Krasemann and R. J. Smith, in press Surface Science.

12. E. J. van Loenen, M. Iwami, R. M. Tromp, and J. F. van der Veen, Surf. Sci. 137(1984)1: E. J. van Loenen, J. F. van der Veen, and F. K. LeGoues, Surf. Sci. 157(1985) 1.

13. F. Ulrich Hillebrecht, John C. Fuggle, Peter A. Bennett, Zygmunt Zolnierek, and Ch. Freiburg, Phys. Rev. B27 (1983), 2179.

14. V. Shutthanandan, Adli A. Saleh, A.W. Denier van der Gon, and R. J. Smith, Phys Rev B 48(1993) 18292.

15. M. Hansen, Constitution of Binary Alloys, edited by K. Anderko, McGraw-Hill, New York (1958).

CHAPTER 5

THIN Fe FILMS ON Al(001) AND Al(110) SURFACES

Introduction

Over the last few years ultra-thin metal film growth on metal substrates has attracted considerable attention in the surface science community. In part this is because of the desirable properties which the intermetallics offer for potential high-temperature structural applications[1] . For example, the iron aluminide alloys have a low material density, low cost and good oxidation resistance. The magnetic properties of Fe are also important for magnetic recording head applications. Iron exhibits the largest saturation magnetization among all pure metals at room temperature. The soft magnetic properties of Fe films can be further improved by forming multilayer structures[2,3] . A good example of such a system is Fe/Al[4] . Finally, the Fe-Al system has also attracted attention as a possible metallization material on InP because of the good lattice matching and relative stability of the intermetallic on this substrate[5]. For all of these reasons it is useful to study the structure of Fe-Al interfaces. In addition, this work adds to our growing understanding of metal-metal interface structure and metal film growth.

Recently several groups have studied the growth of thin Fe films on various metal substrates, including Rh(001)[6] , W(110) and W(100)[7], and Pd(111), Ag(111) and Al(111)[8]. Begley et al. [8] suggest that the Fe atoms diffuse into the Al surface at low coverages and form an amorphous alloy layer on the substrate surface since the low-energy electron

diffraction (LEED) pattern rapidly disappears for Fe coverages less than one monolayer (ML). For higher Fe coverages the diffuse LEED pattern suggests that a poorly ordered Fe overlayer forms. In early studies of Fe growth on Al(100) substrates using electron diffraction it was suggested that Fe grows epitaxially at substrate temperatures between 275°C and 300°C[9]. However, alloy formation may have been occurring on the surface since at lower substrate temperatures the Fe had no preferred orientation, and at temperatures greater than 300° C extensive alloying occurred between the Fe and the Al. In a more recent study Anderson and Norton[10], using Auger Electron Spectroscopy (AES), angle resolved AES (ARAES), low energy electron diffraction (LEED) and Rutherford backscattering (RBS), observed alloy formation for low coverages of Fe deposited on Al(100) substrates at room temperature. As deposition continued, a poorly ordered, ferromagnetic bcc Fe(100) overlayer was observed for more than 4 ML of Fe coverage.

In the present chapter we report and discuss our observations for the growth of thin Fe films on Al(001) and Al(110) surfaces using high-energy ion backscattering (HEIS) and x-ray photoelectron spectroscopy (XPS). The purpose of this study is to characterize the growth mode of thin Fe films on Al surfaces and to develop a growth model by looking at the possibilities of forming an epitaxial overlayer or an alloy at the surface. Film deposition and all measurements were performed at room temperature. The lattice mismatch for a monolayer of Fe on Al(001) is only 0.3% if the cubic Fe unit cell is rotated 45° with respect to the cubic axes of the substrate. This good lattice match suggests the possibility of epitaxial growth of Fe on Al. In a related study Saleh et al.[11,12] investigated the deposition

of Ti on Al(110) and Al(001) surfaces. They found that Ti grows epitaxially in an fcc structure on both surfaces up to a film thickness of about 5 ML. For coverages greater than 5 ML an undetermined combination of island formation and Ti-Al interdiffusion occurs. Since the surface free energy for Fe is somewhat higher than that for Ti, and the formation energy for the FeAl alloy is only -25 kJ/mol, about one-half that for TiAl, a tendency toward Fe island formation is expected. However, we observe an intermixing of Fe and Al atoms on Al(001) surfaces up to 5 ML of Fe coverage, and on Al(110) surfaces up to about 9 ML of Fe coverage, before Fe metal begins to cover the surface alloy. In both cases the Fe 2p core level XPS intensity variation with Fe coverage supports the conclusion of alloy formation.

Experimental setup

All of the experiments were done in an ultra high vacuum (UHV) chamber at a base pressure of about 1×10^{-10} Torr. The chamber is equipped with facilities for HEIS, XPS, Ar-ion sputtering, residual gas analysis and thin film metal evaporation. The 2MV Van de Graaff accelerator is connected to the UHV chamber via a differentially pumped beam line[13]. The Al crystal was mounted in the chamber on a thick Mo block which is attached to a three-axis goniometer for channeling measurements. The standard dose of incident He^+ ions for one spectrum was about 1.6×10^{15} ions/cm^2. Energy analysis of the backscattered He^+ ions for HEIS was performed using a bakeable, passivated, implanted planar silicon (PIPS) detector installed on a rotatable arm and located 7.5 cm from the sample at a scattering angle of 105°. The XPS spectra were measured using a 100 mm VSW

hemispherical analyzer in a fixed-analyzer transmission mode with a pass energy of 50 eV. A Mg K_α ($h\nu$=1253.6 eV) X-ray source with 300 W power was used to generate X-rays. The sample was kept in the channeling position during film deposition and XPS measurements to eliminate problems with reproducing the ion beam-sample alignment. The photoelectrons entered the analyzer with a polar emission angle of 30° measured from the sample normal.

Initially both crystals were mechanically polished and then chemically etched to remove mechanical damage. The crystals were further cleaned in vacuum by Ar sputtering using a beam of 1500 eV energy and 1 mA current distributed over the 1 cm diameter sample. Cleaning the sample required repeated cycles of several hours of sputtering at room temperature, followed by annealing of the samples at 520° C for 20 minutes. The cleaning procedure was repeated until the photopeak associated with the Al-oxide was completely removed from the XPS spectrum of Al. Because a portion of the Mo sample holder was also imaged by the analyzer, we did not use the oxygen 1s photopeak as a measure of the Al surface composition. Iron was vapor deposited onto the Al substrates from a resistively heated Fe wire. The source consisted of three strands of 0.25 mm diameter Fe wire (99.998% purity) twisted together and then wound into a coiled filament. The typical deposition rate with a filament current of 3.8 Amps was about 0.83 ML/min. After each deposition HEIS and XPS measurements were performed. Iron coverage was determined using the ion backscattering spectrum for a random ion beam incident direction. The uncertainty in the results reported here is estimated to be 5.6%, with the largest

contribution to the uncertainty coming from the determination of the detector solid angle, and smaller contributions coming from uncertainties in the integrated charge, the scattering angle, and the determination of the surface peak area.

Results and Discussion

Fe deposition onto Al(001) surface at room temperature

High-energy ion scattering and channeling:

Figure 5.1 shows two ion scattering spectra collected after sputter-cleaning and annealing the sample. The upper spectrum (open circles) was taken with the 0.56 MeV ion beam incident on the sample in a random direction near normal incidence, while the lower spectrum (solid circles) was taken with the beam incident along the [001] direction, i.e., at normal incidence. The measured value for the normalized minimum yield, χ_{min}, was 3.7% measured just behind the surface peak. The calculated value for χ_{min} is 3.6%, obtained using a one-dimensional rms atomic vibration amplitude of 0.105 A at room temperature, and a crystal lattice constant of 4.05 Å[14]. This good agreement is important since it serves as a measure of the bulk crystal quality. Larger measured values of χ_{min} result from increased ion dechanneling which can be associated with defects resulting from sputtering and sample preparation. The measured surface peak area (SPA) in the aligned spectrum corresponds to 9.14 x 10^{15} atoms/cm^2, or 7.5 monolayers, visible to the incident ion beam. The calculated yield is 8.4 monolayers, obtained using the VEGAS simulation code with

uncorrelated thermal vibrations for the atoms and no enhancement of amplitudes at the surface[15].

In Figure 5.2 we show the Al and Fe surface peaks before and after a deposition of 0.87 ML of Fe. Here one ML corresponds to a surface density of 1.22×10^{15} at/cm^2. From Figure 2 we can see that the Al surface peak area increases after the Fe deposition. This indicates that more Al atoms are visible to the incident ion beam in the presence of Fe atoms at the surface. That is, surface Al atoms have moved from their equilibrium positions and reduced the shadowing of subsurface Al atoms. If Fe atoms formed an ordered overlayer directly above Al atoms, as expected due to the perfect lattice match with Al, then we would expect to see a reduction in the SPA of Al due to the Fe atoms shadowing the Al atoms from the incident He^+ ions. Instead we see an increase in the SPA of Al suggesting that Fe and Al atoms are intermixing at the interface, and Fe atoms are displacing the Al atoms from their equilibrium positions. Since the surface peak of the Al atoms is superimposed on the background signal, it is necessary to remove the background under the surface peak. A triangular background subtraction method was used for this purpose[16]. After this background removal the surface peak areas are used to calculate the number of Al and Fe atoms visible to the ion beam. The Fe SPA gives a direct measure of the surface Fe coverage throughout the experiment.

In Figure 5.3 we plot the number of Al atoms/cm^2 (Al-SPA) visible to the incident He^+ ion beam as a function of Fe coverage (Fe-SPA). Such plots are very useful to develop models for alloy formation at interfaces[17]. From this figure we can immediately see that

more and more Al atoms become visible to the incident ion beam as the Fe coverage increases. There are two main regions to note in this figure. In the first region the number of visible Al atoms increases sharply with the Fe coverage up to about 5 ML. The slope of the curve in this region is 1.15 Al atom per Fe atom, suggesting that approximately one Al atom is displaced for every Fe atom deposited on the surface. Therefore, the average stoichiometry of the mixed interface would be 1:1, i.e., FeAl. This is reasonable since the heat of formation of FeAl is -25 kJ/mol and FeAl is a stable phase in the Fe-Al phase diagram. At larger Fe coverages the curve in Figure 5.3 seems to saturate with a zero slope. These observations suggest that the deposited Fe atoms interact with Al atoms on the Al(001) surface and form a mixture of FeAl at the interface up to about 5 ML, and that an Fe film ultimately covers the mixed surface for larger coverages. This is in good agreement with the results of Anderson and Norton[10] where alloy formation was reported up to about 4 ML of Fe coverage, and growth of an Fe(100) overlayer was seen for higher coverages.

A comparison between the HEIS spectra collected with the ion beam incident in a channeling and a random geometry for 9 ML of Fe coverage reveals a slightly smaller Fe SPA in the aligned geometry, as shown in Figure 5.4. A plot of the number of Fe atoms visible to the incident ion beam in the aligned geometry versus the Fe coverage, as measured with a random incident ion direction, is shown in Figure 5.5. Negligible Fe shadowing was observed for Fe coverages less than 4.5 ML. A small, but measurable amount of Fe shadowing is observed for coverages greater than 5 ML, as seen by the reduction in the Fe yield obtained in the normal direction compared to that obtained in the

random direction. This small difference in the Fe hitting probability indicates that the surface Fe film has some degree of axial alignment with respect to the Al substrate so that Fe atoms are being shadowed by Al or other Fe atoms.

X-ray photoelectron spectroscopy:

Next we consider our XPS results. In Figure 5.6 we plot the XPS intensity for the Fe $2p_{3/2}$ photopeak (binding energy 706.75 eV) as a function of Fe coverage. The intensity of the Fe 2p peak shows a distinct change in slope around 4.5 ML of Fe coverage. A transition region starting near 5 ML is in good agreement with the channeling results, suggesting that there is a change in film composition occurring at around 5 ML of Fe coverage. The Fe photopeak signal is attenuated at a different rate in these two regions. XPS is a technique that can also provide information about the chemical nature of the interface, since the core-level electron binding energies for a certain element are subject to variation (typically a few eV) depending on the chemical state of the atom. Gleason and Strongin[18] have measured the $2p_{3/2}$ binding energies of transition metals in bulk elemental samples and in the corresponding aluminides. For FeAl they did not observe a shift in the Fe $2p_{3/2}$ core level in FeAl. This agrees with our observation of negligible chemical shift as shown in Figure 5.7.

A further attempt was made to characterize the interface structure by using the XPS intensity data and following the analysis by Ossicini et al.[19] on the growth of thin metal films on metal substrates. In view of the linear increase which we observe for the XPS photopeak intensity, we assumed that the deposited Fe atoms aggregate to form three-dimensional

islands on the surface (Volmer-Weber growth). It was assumed that we grow an FeAl-like compound up to about 5 ML and pure Fe thereafter for higher Fe coverages. The VW growth model can be adjusted readily to fit our two stage growth model. Since there is no significant Fe 2p chemical shift in the pure Fe and Fe aluminides, it is not possible to conclude that we are forming an FeAl-like compound at the interface for Fe coverages up to about 5 ML. However, the data presented above clearly suggest that there is some structural change occurring in the overlayer at about 5 ML of Fe coverage, and the slope of the HEIS results suggests a 1:1 average stoichiometry for this region. We did not have the LEED capability in these experiments to check for surface ordering. We summarize here the procedure used to determine the parameters in the VW model calculation. First, we assumed an exponential decay for the intensity of the photoelectrons passing through the successive layers of the surface alloy, with a mean attenuation length, λ, calculated by using the formula $\lambda(\text{Å}) = 1430*E^{-2} + 0.54*E^{1/2}$, where E (eV) is the kinetic energy of the electrons[20]. The values of λ for Al and Fe are 18.6 Å and 12.6 Å, respectively. Next, we assumed an interplanar distance, d, between the layers of Fe atoms depending on the alloy being formed. Since there is some evidence for oriented growth, both from our Fe shadowing and the LEED observations of Anderson and Norton[10], we assumed a (100) orientation of FeAl, with a value of 2.91 Å for d[21]. Then for each Fe adlayer the intensity of the photoelectrons decreases by $w = \exp(-d/\lambda\cos\theta)$. Here the factor of $\cos\theta$ corrects for the non-normal emission direction. The attenuation factors, w, for Al and Fe are 0.835 and 0.766 respectively. Finally, we assumed a planar density of Fe atoms equal to that for the

Fe-Al alloy being formed. The only remaining free parameter in this simple VW model is the constant island height, h. We determined h by forcing the coverage of Fe at the completion of the island growth stage, i.e., when the islands coalesce to cover the surface, to match the coverage measured by ion scattering at the corresponding break point, for example at 5 ML in Figure 5.3. Summing over the number of layers, h, results in the following equation for FeAl growth in Region 1 of Figure 5.6.

$$I(x) = I_o S_A m_1 x (1-w^h)/(1-w) \quad (6.1)$$

Here, I_o is the saturation intensity, S_A is a sensitivity factor for Fe photoemission, and x is the fractional coverage for the islands of FeAl on the surface. The value of I_o is determined by normalization to the experimental data at the final Fe coverage in the experiment, and the value of S_A is adjusted initially to fit the slope for Region 1, and not changed thereafter. Terms similar to Equation 1 are included for subsequent growth regimes. The calculated XPS intensities for this VW model are shown (solid circles) along with the experimental data points (open circles) in Figure 5.6. For these results we used the following parameters: Region 1 (FeAl) d = 2.91 Å, m = 1.18 x 10^{15} at/cm^2, and h = 5 layers; Region 2 (Fe) d = 1.43 Å, m = 1.22 x 10^{15} at/cm^2, and h = 5 layers. Clearly, the simulated intensities show the same behavior as the experiment for Region 1. However, the data for Region 2 do not follow a straight line, in contrast to the model calculation. This could be explained, for example, if the Fe islands forming in Region 2 are increasing in height as well as width, unlike the simple VW model calculation. A limiting factor in this calculation is that the experiment was not continued until the Fe XPS signal reached saturation, unlike the results

shown below for Al(110), so proper normalization of the calculated and measured results is not possible.

Fe deposition on the Al(110) surface at room temperature

We performed analyses similar to those just described for the Al(001) surface as a function of Fe coverage on Al(110) surfaces. For this system it is again clear that strong intermixing occurs at the Fe-Al interface rather than forming a simple Fe overlayer as expected based on the small lattice mismatch. In Figure 5.8 we show the number of Al atoms visible to the incident ion beam plotted as a function of Fe coverage, determined by measuring the peak areas of the Al and Fe surface peaks in the channeling spectra. From this figure we can immediately see that more Al atoms become visible to the incident ion beam as the Fe coverage increases up to about 9 ML (7.76×10^{15} atoms/cm^2). On the Al(110) surface 1 ML is equal to a surface density of 8.622×10^{14} atoms/cm^2. There are three main regions to recognize in this figure. In the first region the number of visible Al atoms increases sharply with the Fe coverage up to 2 ML. The slope of the curve in this region is 3.16 which means that each Fe atom effectively displaces about 3 Al atoms. This is suggestive of forming an $FeAl_3$-like compound in the first region. $FeAl_3$ is also a stable phase in the Fe-Al phase diagram with a formation energy of -28 kJ/mol. In the second region the number of visible Al atoms increases with a lesser slope than in the first region, up to about 9 ML of Fe coverage. In this region the slope is 0.96 Al atom per Fe atom suggesting that an FeAl-like compound is being formed. After 9 ML of Fe coverage the

curve seems to saturate along a line with zero slope. In other words, the displacement of Al atoms has stopped after a coverage of 9 ML, and an Fe metal overlayer begins to form. These observations suggest that Fe atoms are mixing with Al atoms on the Al(110) surface at two different rates, forming a surface alloy at the interface, until an Fe metal film ultimately covers the mixed interface. The mixing continues up to about 9 ML of Fe coverage at room temperature. However, it is important to note that it is difficult to confirm with ion scattering alone the actual stoichiometry of a compound when the layer is thin. There may be some displacements of Al atoms just below the alloy interface. Also, near-surface dechanneling below the interface can occur as a result of ion beam defocussing by near-surface Fe atoms. We have reported this phenomenon previously for Ni films on Al(110)[22].

In Figure 5.9 we show the energy distribution of the backscattered ions in the regions of the Al and Fe surface peaks for several Fe coverages. Each curve is identified by the Fe coverage. The arrows and the dashed lines in the figure indicate the energetic positions of the surface Al and Fe atoms. There is no significant shift in the Al surface peak up to about 4 ML of Fe coverage. However, after this coverage of Fe the position of the Al surface peak starts shifting to lower energies as seen in Figure 5.9. This is because the ion beam loses energy as it passes through the Fe film on the surface.

We did not see any evidence for diffusion of Fe atoms into the Al substrate. Since we did not observe any significant broadening of the Fe surface peak at lower coverages, and continuous displacements of the Al atoms were observed for these lower Fe depositions

(increased Al SPA), we conclude that the deposited Fe atoms are staying near to the surface region, resulting in alloy formation at the surface. A plot of the number of Fe atoms visible to the incident ion beam in the channeling direction versus the actual Fe coverage, obtained from a random incident direction, is shown in Figure 5.10. We did not see any reduction in the number of Fe atoms visible to the ion beam along the channeling direction. This is in contrast with the Al(001) surface where the Fe film apparently has some degree of axial alignment with respect to the Al substrate after about 4.5 ML of Fe deposition (Figure 5.5). Similar behavior has been seen with Pd on these two Al surfaces.

We performed an XPS photopeak intensity analysis of the Fe $2p_{3/2}$ photopeak similar to that discussed for the Al(001) surface. We again assumed that we have a simple Volmer-Weber type growth mode in the corresponding regions. As suggested by the slopes in Figure 5.8, we constructed a model assuming $FeAl_3$ island growth up to about 2 ML of Fe coverage, followed by growth of FeAl islands to about 9 ML, and ending with the growth of Fe islands to the final coverage of the experiment. Again, the interplanar distances and adatom planar densities were based on the values of the corresponding assumed compounds, and the island height was determined by forcing the Fe coverage to agree with that measured by ion scattering at the break points in Figure 5.8, where island coalescence is assumed at the conclusion of each growth region. The results of the model calculation are shown in Figure 5.11 as solid circles, along with the measured XPS intensities (open circles). Both sets of data have been normalized to unity intensity at the conclusion of the experiment where XPS shows only as Fe signal, since the film is

sufficiently thick to completely attenuate the Al XPS signal. This model calculation seems to agree very well with the data, supporting the three stage growth mode suggested by the ion scattering results. The structural parameters used for the fit in Figure 5.11 are: Region 1 ($FeAl_3$) d = 8 A, m = 1.294 x 10^{15} at/cm^2, and h = 2 layers; Region 2 (FeAl) d = 2.06 A, m = 0.836 x 10^{15} at/cm^2, and h = 7 layers; Region 3 (Fe) d = 2.023 A, m = 0.865 x 10^{15} at/cm^2, h = 10 layers. The different growth behavior which we observe for Fe films on these two aluminum surfaces may be attributed to the differences in the surface structure and/or surface energies of the surfaces. The relatively open Al(110) surface has the largest surface energy (0.959 J/m^2) among the three low-index surfaces of Al, while the close-packed Al(111) surface has the lowest (0.824 J/m^2). The surface energy of the Al(001) surface is about 10% less than that of the Al(110) surface[23].

Conclusions

In summary, we have performed an ion scattering investigation, combined with XPS, of thin Fe films deposited on Al(001) and Al(110) surfaces. We observe the continued displacement of substrate atoms for depositions up to 5 ML on the Al(001) surface and up to 9 ML on Al(110). Strong substrate-overlayer intermixing is indicated rather than the layered growth expected from the very good lattice match of Fe with Al. We propose a Volmer-Weber type growth model for these interfaces consisting of the initial growth of a thin mixed layer of dilute Fe alloy, followed by the overgrowth of a more Fe-rich phase on Al(110), until Fe metal starts to cover the surface. On the Al(001) surface Fe metal starts to

grow after 5 ML of Fe coverage, while on the more open Al(110) surface, the mixing continues up to 9 ML of Fe coverage. In neither case was Fe diffusion into the bulk Al substrate observed at room temperature. XPS results show no chemical shift larger than the resolution of our measurements for the Fe 2p core level in Fe-aluminides. Finally, an analysis of the Fe XPS photopeak intensity as a function of Fe coverage, using a Volmer-Weber model, supports a two stage development for Al(001) surfaces, and a three-stage growth model for Al(110) surfaces, although the solution may not be not unique.

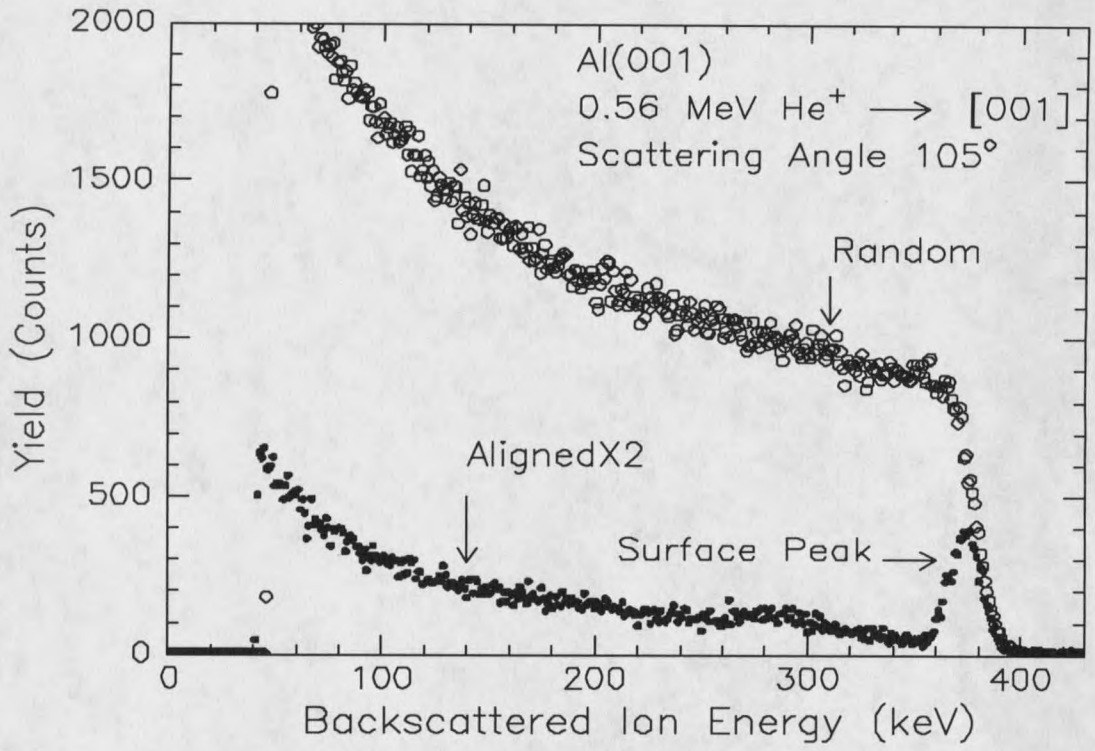

Figure 5.1. Ion scattering spectra for 0.56 MeV He^+ ions incident on the clean Al(001) surface. The open circles show a spectrum taken with a random incident direction for the ion beam, and the solid circles show the data for normal incidence, along the [001] direction.

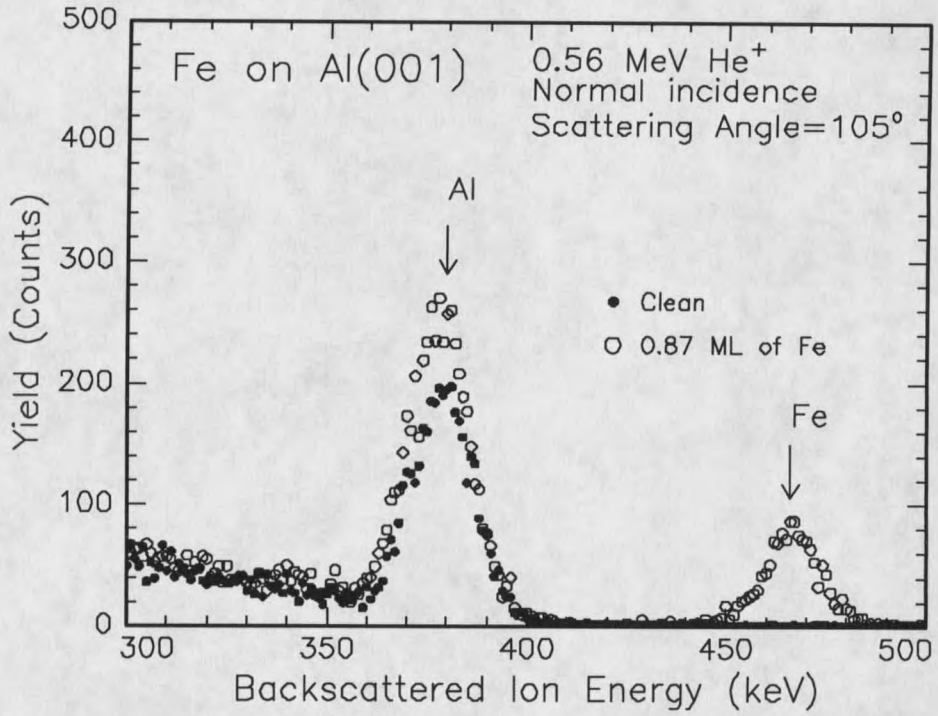

Figure 5.2. Ion scattering spectra for the clean Al(001) surface (solid circles) and for 0.87 ML Fe deposited on the Al(001) surface (open circles). The energies for backscattering from Al and Fe surface atoms are indicated by the rows.

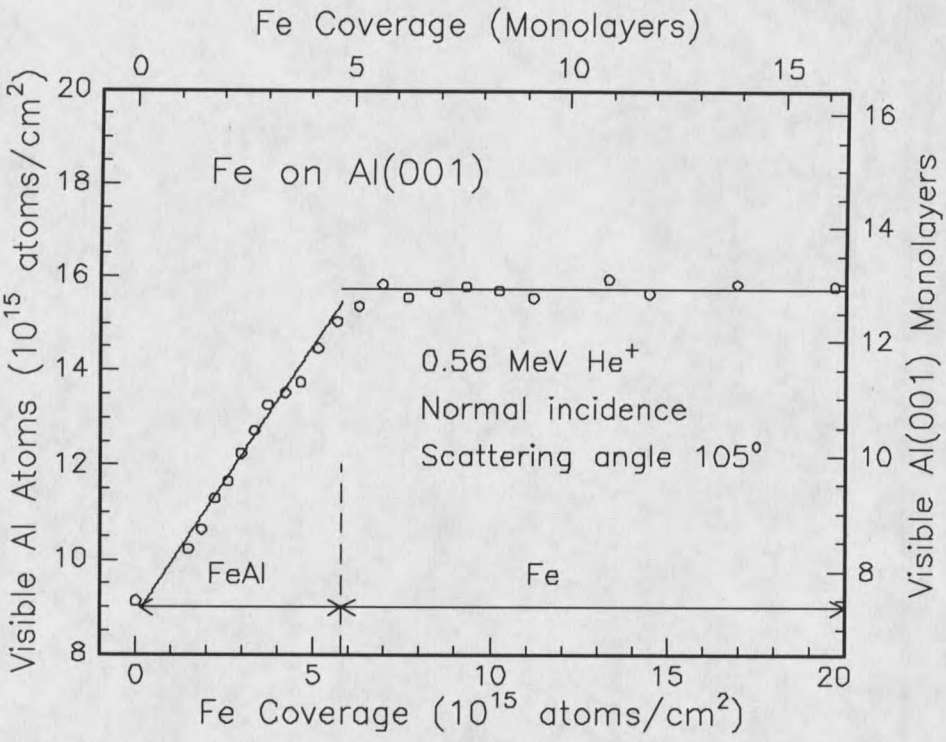

Figure 5.3. Visible Al atoms at 0.56 MeV incident ion energy, as a function of Fe coverage deposited at room temperature on Al(001). Two regions of film growth are indicated. The solid lines are linear fits to the data in the two regions.

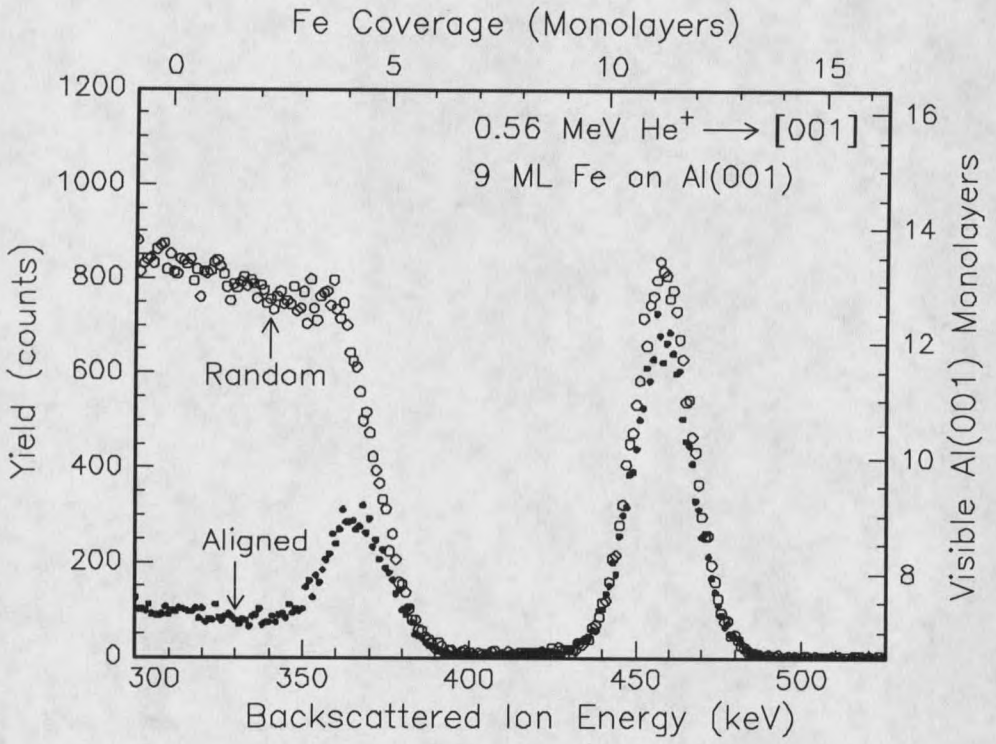

Figure 5.4. He^+ ion scattering spectra at 0.56 MeV incident ion energy after the deposition of 9 ML of Fe. The open circles show the spectrum taken with a random incident direction for the ion beam, while the solid circles show the data for incidence along the [001] direction.

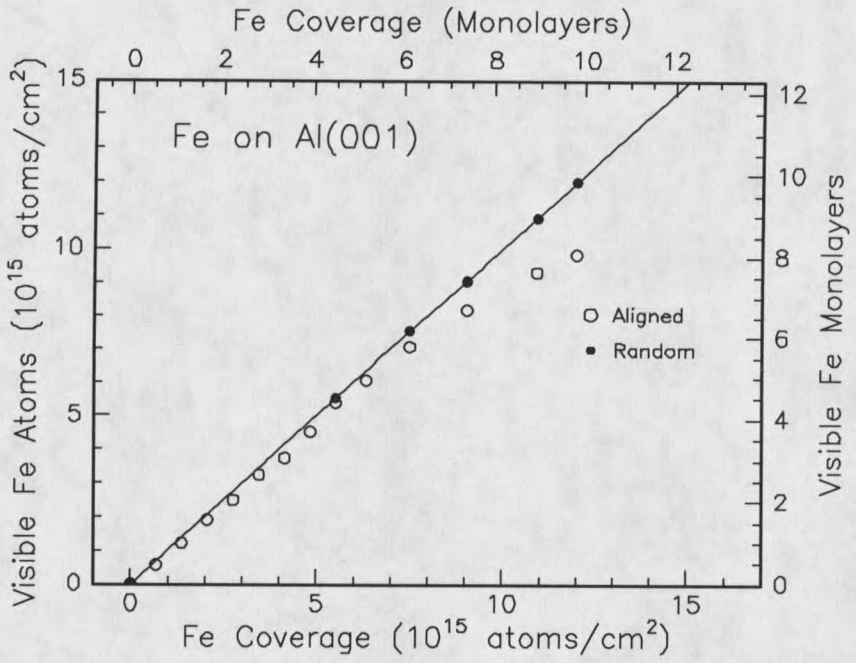

Figure 5.5 Visible Fe atoms at 0.56 MeV incident ion energy, as a function of Fe overlayer coverage. The open circles show the data obtained with the ion beam incident along the [001] direction, and show evidence of Fe shadowing for coverages greater than 4.5 ML. The solid circles and solid line show the yield from Fe atoms measured for the ion beam incident in a random direction.

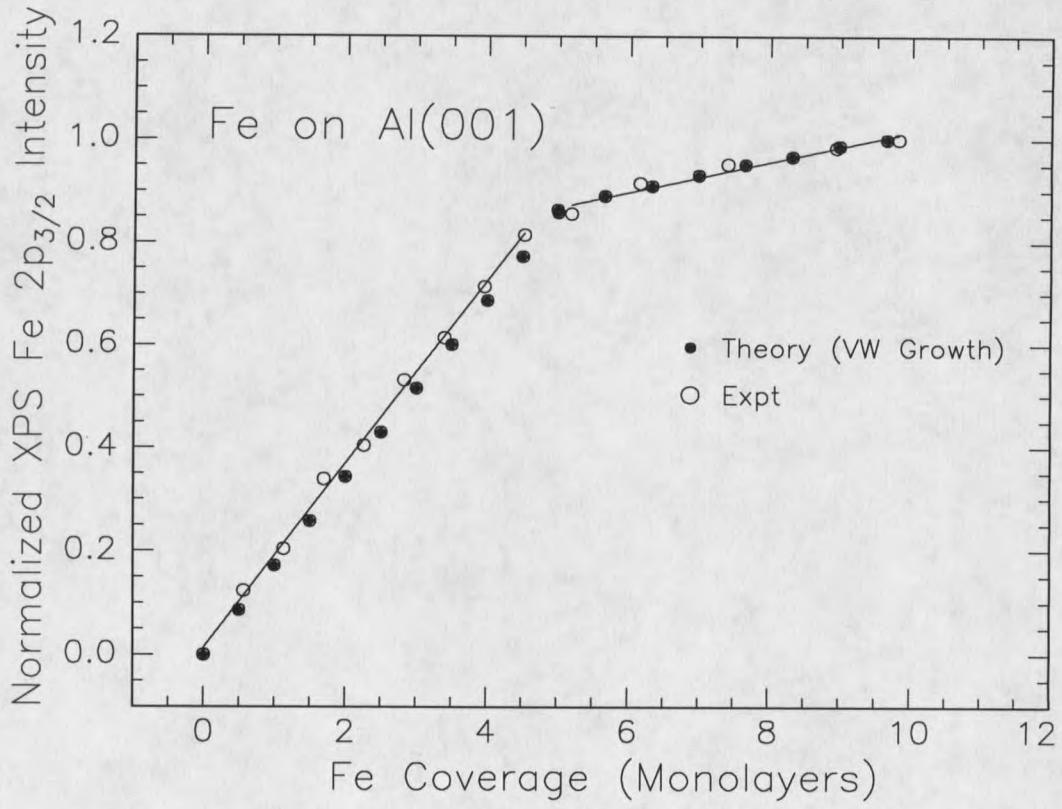

Figure 5.6. Measured XPS intensity for the Fe $2p_{3/2}$ photopeak (open circles) as a function of Fe coverage. The Fe $2p_{3/2}$ intensity has been normalized to its value at the maximum coverage of our experiment (10 ML). The solid circles are the calculated emission intensity for the Volmer-Weber growth model described in the text. Two regions of growth are evident, with a change in film structure around 5 ML of coverage.

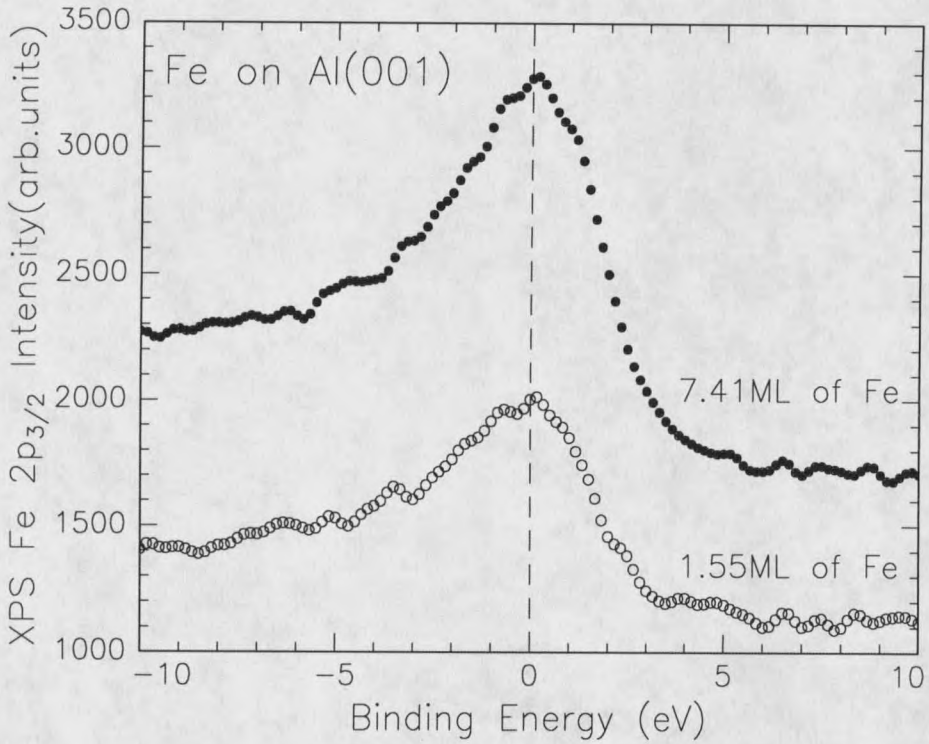

Figure 5.7. XPS measurements of the Fe $2p_{3/2}$ peak at two different coverages of Fe, 1.55 ML and 7.41 ML respectively. The peak in the upper curve is aligned with the zero binding energy marker. No noticeable shift in binding energy is seen for Fe atoms in the low coverage experiment.

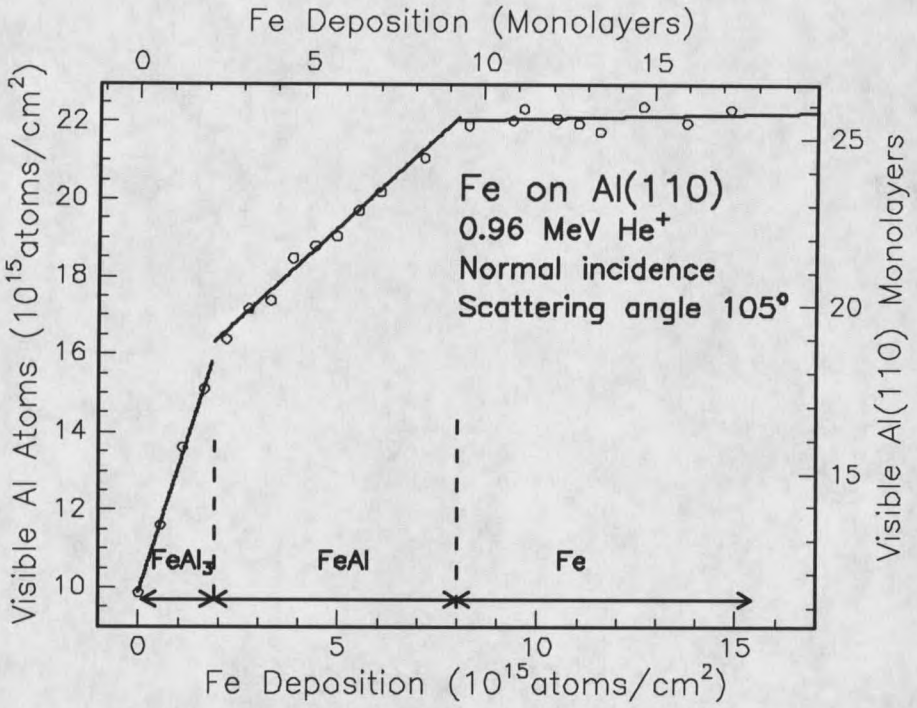

Figure 5.8. Visible Al atoms, at 0.96 MeV incident ion energy, as a function of Fe coverage deposited at room temperature on the Al(110) surface. The solid straight lines are linear fits to the data within the three coverage regimes indicated by the vertical lines.

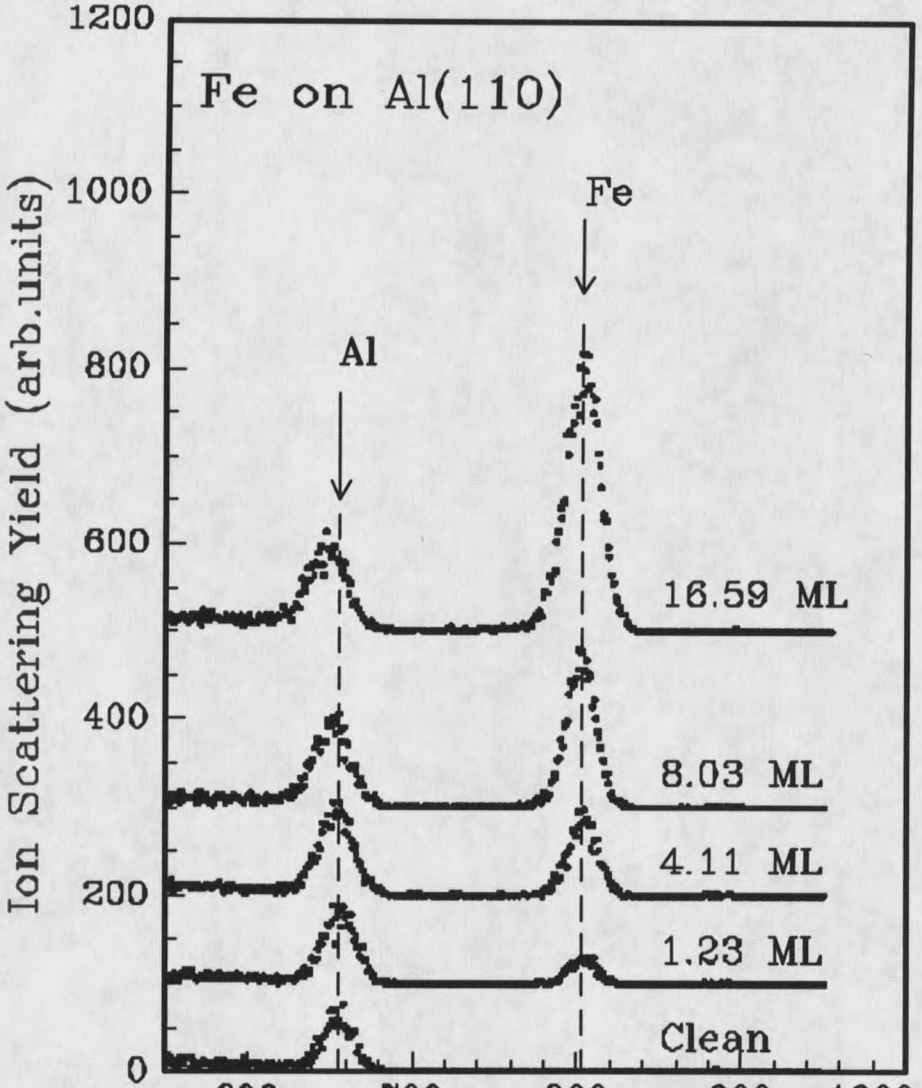

Figure 5.9. Ion scattering spectra for 0.96 MeV He^+ ions on Fe + Al(110) for different Fe coverages as indicated in the figure. The energetic positions of the Al and Fe surface peaks are indicated by the arrows and dashed lines.

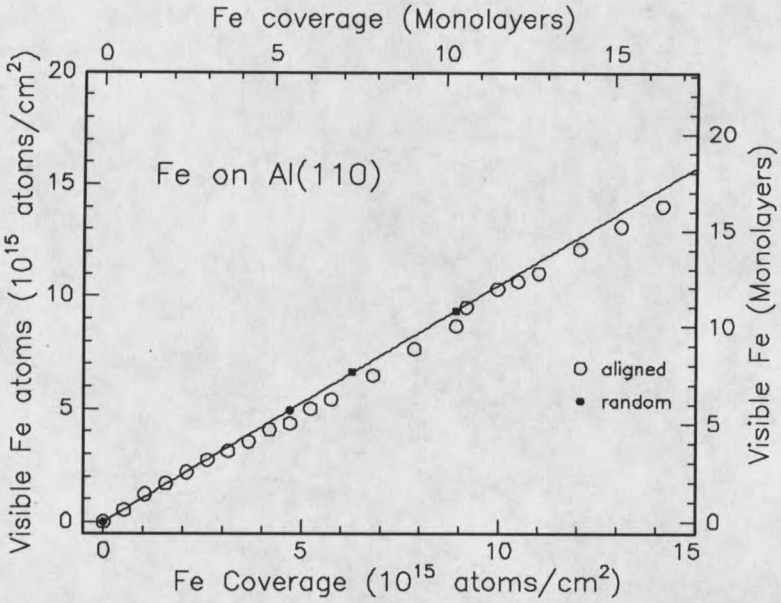

Figure 5.10. Number of Fe atoms visible to the 0.96 MeV He^+ ion beam as a function of Fe coverage. The solid line shows the yield expected for a random direction of incidence.

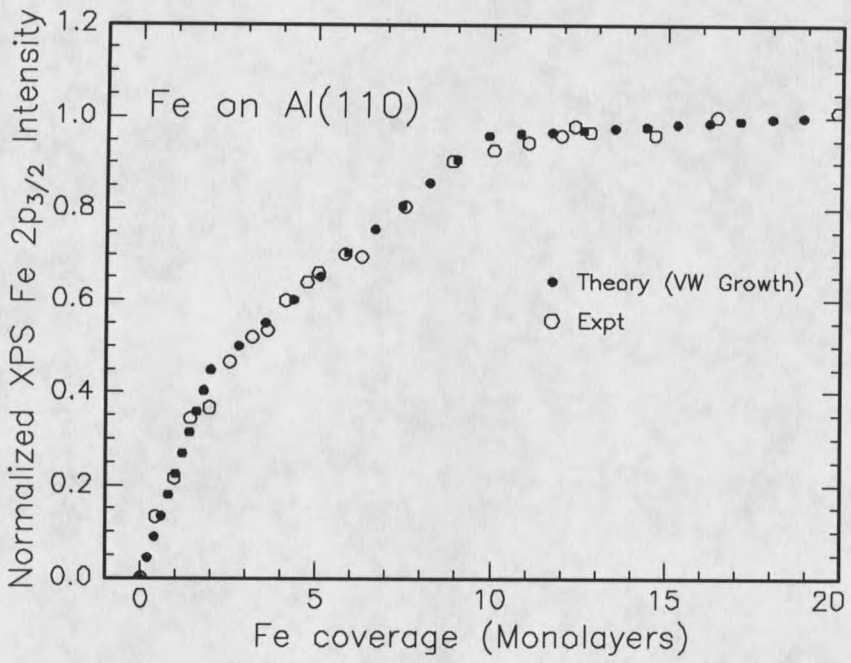

Figure 5.11. Measured (open circles) and calculated (solid circles) XPS intensities of Fe $2p_{3/2}$ as a function of Fe coverage. The solid circles were calculated using the Volmer-Weber growth model discussed in the text with three different growth regimes.

REFERENCES

1. C. C. Koch, C. T. Liu, and N. S. Stoloff, Eds., High-Temperature Ordered Intermetallic Alloys, MRS Symposia Proceedings, 39 (MRS, Pittsburgh, PA) 1985.
2. T. Kobayashi, R. Nakatani, S. Ootomo and N. Kumasaka, J. Appl. Phys. 64 (1988) 3157.
3. M. Senda and Y. Nagai, J. Appl. Phys. 65 (1989) 3157.
4. T. Yamamoto, M. Nagakubo and M. Naoe, J. Appl. Phys. 63 (1988) 5751.
5. A. M. Wowchak, J. N. Kuznia and P. I. Cohen, J. Vac. Sci. Technol. B 7 (1989) 733.
6. C. Egawa, Y. Tezuka, S. Oki and Y. Murata, Surf. Sci. 283 (1993) 338.
7. P. J. Berlowitz, J. W. He and D. W. Goodman, Surf. Sci. 231 (1990) 315.
8. A. M. Begley, D. Tian, F. Jona and P. M. Marcus, Surf. Sci. 280 (1993) 289.
9. D. C. Hothersall, Philos. Mag. 15 (1967) 1023.
10. G. W. Anderson and P. R. Norton, Surf. Sci. 336 (1995) 262.
11. Adli A. Saleh, V. Shutthanandan and R. J. Smith, Phys. Rev B 49 (1994) 4908.
12. Adli A. Saleh, Ph.D Thesis, Montana State University (1994).
13. R. J. Smith, C. N. Whang, Xu Mingde, M. Worthington, C. Hennesy. M. Kim and N. Holland, Rev. Sci. Instrum. 58 (1987) 2284.
14. D. S. Gemmel, Rev. Mod. Phys. 46 (1974) 129.
15. J. W. Frenken, R. M. Tromp and J. F. van der Veen, Nucl. Instrum. Methods B 17 (1986) 334.

16. I. Stensgaard, L. C. Feldman and P. J. Silverman, Surf. Sci. 77 (1978) 513.

17. J. F. Van Loenen, M. Iwami, R. M. Tromp and J. F. van der Veen, Surf. Sci. 137 (1984) 1.

18. N. R. Gleason and D. R. Strongin, Surf. Sci. 295 (1993) 306.

19. S. Ossicini, R. Memeo and F. Ciccacci, J. Vac. Sci. Technol. A 3 (1985) 387.

20. M. P. Seah and W. A. Dench, Sur. Anal. 1 (1979) 2.

21. M. Hansen, Constitution of Binary Alloys, K. Anderko, ed., (McGraw-Hill, New York, NY) 1958.

22. V. Shutthanandan, Adli A. Saleh, A. W. Denier van der Gon and R. J. Smith, Phys. Rev. B48 (1993) 18292.

23. S. P. Chen, A. F. Voter, R. C. Albers, A. M. Boring and P. J. Hays, J. Mat. Res. 5 (1990) 955.

CHAPTER 6

THIN Co FILMS ON Al(001) AND Al(110) SURFACES

Introduction

The correlation between the structure and the properties of ultrathin metal overlayers on single crystal substrates has received considerable attention recently[1,2]. In particular epitaxial growth of metals on metals is currently a widely studied topic, both experimentally and theoretically[3]. However, the evolution (as a function of thickness) of the structure of metal films deposited on other metals is still not understood. In this chapter, a study of the growth of thin Co films on Al(110) and Al(001) surfaces at room temperature is presented. Co assumes a hexagonal, close-packed (hcp) crystal structure in its bulk state at room temperature, with lattice constants a = 2.51 Å and c = 4.07 Å. On the other hand, Al has a face-centered cubic (fcc) crystal structure with a lattice constant of 4.05 Å. Using these values for the lattice constants, a mismatch of 14% in the nearest neighbor distances is obtained. The surface free energy of both Al(110) and Al(001) surfaces is less than half of Co[4], suggesting that an overlayer growth is not possible. Also the surface energy of Co is slightly larger than that for Ti , but less than that of Fe. The formation energy for CoAl is -54 kJ/mole, about the same as for NiAl. Shutthanandan et. al. have studied the growth of Ni films on both Al surfaces in detail[5].

Thus Co and Al have a combination of properties that are quite similar to the case for Ni on Al surfaces. That is, the metal has a large lattice mismatch with the substrate, and the ordered alloy has an intermediate value for the formation energy with excellent lattice matching between the ordered alloy (lattice constant of CoAl is 2.862 Å) and the substrate. Unlike Ni, Co has the hcp structure at room temperature, and transforms to an fcc lattice structure at high temperatures[6]. Like Fe on Al, Co-Al multilayers have been investigated for their magnetic properties[7]. Furthermore Co has been observed to grow both fcc and bcc allotropes on Cu surfaces where the nearest-neighbor distances are better matched between substrate and the overlayer[8].

To better characterize the evolution of the Co/Al interface, we have carried out high-energy ion scattering (HEIS), x-ray photoelectron spectroscopy (XPS), and low energy electron diffraction (LEED) experiments on thin Co films deposited on Al(001) and Al(110) single-crystal surfaces. Structural information obtained in our studies should be valuable for understanding the magnetic properties of Co layers on Al surfaces, and contribute to our understanding of overlayer film growth.

Experimental setup

The use of HEIS-channeling measurements to probe the surface structure during overlayer growth was presented in Chapters 4 and 5. The basic principles of the technique were introduced in Chapter 2. The preparation of the clean substrate surface and the Co deposition source was discussed in Chapter 2 as well. Similar procedures

were followed to prepare both the crystals and to deposit films. A chamber base pressure of 1.2×10^{-10} Torr was obtained after baking the system. After every experiment, and before the Co deposition, the samples were sputter-cleaned, annealed, and realigned with the ion beam. During Co deposition, channeling measurements, with the ion beam incident along the [110] direction (Al(110) surface) and [001] direction (Al(001) surface) were performed. The standard dose of incident He^+ ions for one spectrum was 1.6×10^{15} ions/cm^2. A solid-state detector was used to collect the backscattered He^+ ions at a scattering angle of 105°. The Co coverage was determined by rotating the sample out of alignment, but near normal incidence, and then measuring the Co peak area in the backscattering spectrum. Cobalt was vapor-deposited on the Al crystal surfaces from a resistively heated Co wire filament (0.25mm diameter, 3 strands). Typical deposition rates in these experiments were 0.388 x 10^{15} atoms/cm^2/min or 0.45 ML/min for the Al(110) surface, and 0.427 x 10^{15} atoms/cm^2/min or 0.35 ML/min for the Al(001) surface. One monolayer (ML) here is equivalent to 0.8622 x 10^{15} and 1.219 x 10^{15} atoms/cm^2, the atomic density of the Al(110) and Al(001) planes respectively.

The XPS spectra were recorded using a 100 mm hemispherical analyzer (HA) in a fixed-analyzer-transmission (FAT) mode with a pass energy of 50 eV, and a scan rate of 0.1 eV/sec. A Mg K_α (1253.6 eV) x-ray source with 300 W power was used to generate x-rays. For XPS measurements, the sample was kept in the channeling geometry, and the photoelectrons entered the HA with a polar emission angle of 30° from the sample

normal. For the XPS analysis, Al 2p and Co 2p core level spectra were collected in the same manner as described in previous chapters.

Results & Discussion

Al(001) surface

After sputter-cleaning and annealing the sample, it was aligned along the [001] direction using a 1 MeV He^+ ion beam. The measured value for the normalized minimum yield, χ_{min}, was 3.69%, measured just behind the Al surface peak[9]. The calculated value for χ_{min} is 3.6%, obtained using a one dimensional rms atomic vibration amplitude of 0.105 Å at room temperature, and a crystal lattice constant of 4.05Å[10]. The good agreement is important since it serves as a measure of crystal quality. Larger measured values of χ_{min} might indicate, for example, the presence of deeply embedded transition metal atoms remaining from previous experiments, or defects associated with sputtering and sample preparation, all of which could result in increased ion dechanneling. Furthermore, sharp LEED spots in a rectangular pattern were obtained, reflecting the (001) surface symmetry, and also supporting the cleanliness of the Al surface. The low electron beam kinetic energy of 35.7 eV facilitated probing the structure of the topmost layers. Pictures of the LEED spots are shown in Figure 6.1 (a)-(d) for the clean surface for electron energies at 35.7 eV, 41.4 eV, 66.5 eV, and 80.8 eV respectively.

In Fig. 6.2 we show the Al and Co surface peaks before and after deposition of 0.84 ML Co. From Fig. 6.2 it is obvious that the Al surface peak area increases after the

Co deposition. This suggests that more Al atoms are visible to the incident ion beam in the presence of Co atoms at the surface. That means surface Al atoms have moved from their equilibrium positions and reduced the shadowing of substrate Al atoms. If Co atoms formed an ordered overlayer directly above Al atoms, then we would expect to see a reduction in the surface peak area (SPA) of Al due to the Co atoms shadowing the Al atoms from the incident ions. Instead the increase in the SPA of Al indicates that Co atoms are causing the Al atoms to be displaced from their equilibrium positions.

In Fig. 6.3 we plot the number of visible Al atoms (Al-SPA) as a function of Co coverage (Co-SPA), as determined from channeling spectra similar to those shown in Fig. 6.2. Such plots are very useful for developing models for mixed interfaces[11]. A triangular background subtraction method[12] was used to subtract the background associated with the Al surface peak. The surface peak areas of both Al and Co are used to calculate the number of Al and Co atoms visible to the ion beam. The Co SPA in the random geometry gives a direct measure of the surface Co coverage throughout the experiment. From this figure we can immediately see that more and more Al atoms become visible to the incident ion beam as the Co coverage increases up to about 3 ML (3.657×10^{15} atoms/cm^2). There are two main regions to identify here. In the first region the number of visible Al atoms increases sharply with the Co coverage up to about 3 ML. The slope of the curve in this region is equal to 1.98. In the second region the slope is almost zero which indicates that pure Co metal has started to grow on top of the mixed interface. Furthermore the low energy tail of the Co surface peak does not have any broadening,

even at 9 ML of Co coverage, ruling out the possibility of any diffusion of Co atoms deep into the bulk. The presence of the Co atoms on the surface apparently caused the minimum yield behind the Al surface peak to increase gradually. This was due to the slight deflections of some He^+ ions as they traversed through the mixed surface. We infer that the deposited Co atoms are staying near to the surface region.

The large increase in the number of Al atoms visible to the incident ion beam, measured as a function of Co coverage and shown in Fig. 6.3, indicates that there is a strong Co-Al mixing at the interface. In a conventional interpretation[13] of the results in Fig. 6.3, the slope for ion scattering yield versus Co coverage is used to determine the average stoichiometry of the mixed interface region. In the present case, a slope of 1.98:1 in region one would indicate that we are forming a $CoAl_2$ phase. However, there is no stable Co-Al compound with this stoichiometry in the Co-Al bulk phase diagram[6]. Instead based on the XPS and Volmer-Weber growth model analysis discussed below, we conclude that a CoAl-like compound is formed. Furthermore, as we mentioned in the introduction, CoAl has the highest heat of formation and is the most stable phase in the Co-Al phase diagram, so we might expect it to form first. A similar behavior was observed in the case of Ni on Al(110)[14] and Embedded Atom Method (EAM) simulations were used to show that the additional slope of 1 was added due to a phenomenon called *"near surface dechanneling effect"*[15].

A plot of the number of Co atoms visible to the incident ion beam in the channeling direction versus the actual Co coverage, obtained from the random direction,

is shown in Fig. 6.4. We did not see any reduction in the number of Co atoms visible to the ion beam along the channeling direction, as seen in Fig. 6.4. This indicates that there is no shadowing of Co atoms for coverage up to 7.6 ML.

Figure 6.5 displays the LEED patterns observed at various Co coverages. The initial sharp Al(001) LEED pattern (Fig. 6.5(a)) completely disappears by 0.5 ML Co coverage (Fig. 6.5(b)). This rapid obliteration in LEED spot intensity indicates that a rapid loss of long-range order in the entire near surface region is occurring. Furthermore we speculate that the Co atoms mix with the Al atoms very rapidly and form an amorphous alloy layer on the surface of the substrate since only 0.5 ML of disordered Co itself is not likely to be solely responsible for the above behavior. As Co deposition continues (Fig. 6.5(c)), a fuzzy, square LEED pattern with very broad spots was observed for 7.6 ML Co coverage. This indicates that, although the initial LEED pattern disappears at low coverage, the overlayer pattern is oriented to some extent relative to the Al(001) substrate at higher Co coverages. That is, the overlayer still retains memory of the substrate orientation even though it has lost the long-range order completely in the early stages of Co deposition.

Now we will turn our attention to the XPS results. XPS is a technique that gives information about the chemical bonding and structure of the interface, since we can accurately measure the change in binding energy due to the metal and its aluminides. This has been demonstrated successfully in the case of Pd on Al(001)[16] and Al(110)[17] surfaces. In Fig. 6.6 we plot the normalized XPS intensity for the Co $2p_{3/2}$ photopeak

(binding energy 777.9 eV) as a function of Co coverage. The Co intensity was normalized to its value at the maximum coverage in our experiment (7.6 ML). The intensity of the Co $2p_{3/2}$ peak (Fig. 6.6) shows a change in slope at around 3 ML of Co coverage. This in good agreement with the channeling results, suggesting that there is a change in film composition occurring at around 3 ML of Co coverage. Since the experiment was not continued until the Co XPS signal reached saturation, in region 2, the Co $2p_{3/2}$ signal is still going up but at a lower rate than in region 1. In other words, proper normalization of the Co XPS signal was not possible in this case.

Figure 6.7 shows the normalized Al 2p photopeak area as a function of Co coverage. The Al intensity was normalized to the intensity of the clean surface. It also shows two different regions. There is an initial 15% drop in the Al 2p intensity up to about 3.5 ML of Co coverage. Thereafter, the intensity decreases at a faster rate as the Co coverage increases. As one can see the intensity is still about 60% of the clean value even after the deposition of 7.6 ML of Co which is about 10 Å thick. This can be attributed to the long mean free path of Al photoelectrons which is 18.56 Å[18] for this kinetic energy. As in the case of Fe on Al(001)[19], a further attempt was made to characterize the interface structure using the XPS intensity data and following the analysis by Ossicini et. al[20] on the growth of thin metal films on metal substrates. We assumed that the deposited Co atoms aggregate to form three-dimensional islands on the surface (Volmer-Weber growth). A detailed description of the Volmer-Weber growth model that we used in this chapter can be found in Chapter 4. We will only present the values of the parameters

used in the calculation. The values of λ for Al and Co are 18.56 Å and 11.78 Å, respectively. Next we assumed an interplanar distance d between the layers of Co atoms to be 2.862 Å[21]. Then, for each Co adlayer, the intensity of the photoelectrons decreases by w = exp (-d/λ cos θ). Here the factor of cos θ corrects for the non-normal emission direction. The attenuation factors w for Al and Co are 0.835 and 0.755, respectively. In region 1, we assumed that we are forming either CoAl (ratio 1:1) or Co_2Al_5 (ratio 1:2.5) since both phases exist in the Co-Al phase diagram. The reason that we chose Co_2Al_5 is because the channeling results gave a slope of 1.98 in region one. The calculated XPS intensities for this VW model are shown (x : CoAl and o : Co_2Al_5) along with the experimental data points (solid circles) in Fig. 6.6. For these results we used the following parameters: region 1 (CoAl) d = 2.862 Å, m = 1.22 x 10^{15} atoms/cm^2 and h = 3 layers, (Co_2Al_5) d = 3.804 Å, m = 0.525 x 10^{15} atoms/cm^2 and h = 3 layers; region 2 (Co) d = 2.035 Å, m = 1.838 x 10^{15} atoms/cm^2 and h = 5 layers. Clearly, the simulated intensities for CoAl show the same behavior as the experiment for region 1, and the Co_2Al_5 overestimates the Co intensity. Therefore we conclude that in region 1 we are forming a mixture of CoAl. A similar analysis was performed for the Al substrate as well. Summing over the number of layers, h, in the CoAl model results in the following equation for Al growth in region 1 of Fig. 6.7

$$I_s(x) = I_o S_s \left[\frac{m_s w_s^h}{(1-w_s)} + \frac{m_a(1-w_a^h)}{(1-w_a)} \right] \qquad (6.1)$$

Here, I_o is the saturation intensity and S_s is a sensitivity factor for Al photoemission. m_s, m_a, w_s and w_a are the number of Al atoms/cm^2 , number of Co atoms/cm^2, attenuation factor of Al and Co respectively. The values used in this model in region 1 are m_s= 1.219 x10^{15} atoms/cm^2, m_a = 1.220 x 10^{15} atoms/cm^2, w_s = 0.882, and w_a = 0.837. The calculated Al XPS intensities for this VW model are shown (solid circles) along with the experimental data points (open circles) in Fig. 6.7. Obviously there is a very good agreement between the simulated and the experimental XPS intensity values when we assume the structure formed in region 1 is CoAl. This further supports our conclusion that we are forming a 1:1 (CoAl) structure and not Co_2Al_5.

In fig. 6.8, we plot the binding energy of the Co 2p line (777.9 eV, left axis) and the Al 2p line (72.65 eV, right axis) as a function of Co coverage. The binding energy position of Co 2p is slowly decreasing, reaching a value of 777.65 as Co deposition increases up to about 3.5 ML. It suggests that there is a chemical shift of 0.25 eV associated with the formation of CoAl at the interface in region 1. After this transition point the Co 2p binding energy position started to increase, slowly reaching the bulk value 777.9 eV at around 7.6 ML of Co coverage. On the other hand, the position of the Al 2p photopeak didn't show an obvious shift at any stage of Co deposition. Chemical shifts of the Al 2p or Co 2p line are not available in the literature, to our knowledge. Hence it is impossible to compare our results with the bulk CoAl binding energy. Furthermore we should point out that the chemical shift that we saw for the Co 2p line is within the experimental resolution of our XPS hemispherical analyzer. Finally, some

cobalt metal was left on the sample holder from previous experiments. Hence the binding energy of Co $2p_{3/2}$ at submonolayer Co coverage (Fig. 6.8) has the pure metal value (777.9 eV) because the sample holder is also seen by the XPS analyzer.

Al(110) surface

Similar analyses were performed as we just did for Al(001) as a function of Co coverage on Al(110) surfaces. For this system, it is again obvious that strong intermixing occurs at the Co-Al interface rather than forming an ordered Co overlayer. As mentioned earlier in the introduction, metals like Ni and Co have a combination of properties which are very similar and are expected to behave similarly. For Ni on the Al(110) surface, Shutthanandan et. al[14] observed a strong intermixing at the interface. In Fig. 6.9 we show the number of Al atoms visible to the incident ion beam plotted as a function of Co coverage on Al(110). We can clearly see that more Al atoms become visible to the incident ion beam as Co deposition continues up to about 5 ML (4.31×10^{15} atoms/cm^2). There are two main regions to identify in figure. In the first region, the number of visible Al atoms increases at a fast rate with the Co coverage up to about 5 ML. The slope of the curve in this region is 2.3 Al atoms per Co atom, suggesting that approximately 2.3 Al atoms are displaced for every Co atom deposited on the surface. This is suggestive of forming a Co_2Al_5-like compound in the first region. Co_2Al_5 is also a stable phase in the Co-Al phase diagram, with a formation energy of -41 kJ/mol[6]. However, we have seen for Co on Al(001) and for Ni on Al(110)[14] that the actual stoichiometry of an alloy should

not be assigned based only on the slope of the ion scattering yields. Near surface dechanneling can occur as a result of ion beam defocussing by surface Co atoms and there may be some displacements of Al atoms just below the alloy surface. Both factors may result in misleading yield curves. After 5 ML of Co coverage the curve seems to saturate with a zero slope. In other words, the displacement of Al atoms has stopped after a coverage of 5 ML, and a pure Co metal overlayer starts to form on top of the mixed interface. From the above observations we can conclude that Co atoms are mixing with Al atoms on the Al(110) surface at one rate, forming a surface alloy at the interface, until a Co metal film ultimately covers the mixed interface.

Similar to the results in the previous section (Fig. 6.4), we did not observe any reduction in the number of Co atoms visible to the ion beam along the channeling direction for Co on Al(110). The same behavior was observed in the case of Ni on Al(110)[14]. However, different behavior was seen for Pd on these two Al surfaces[16,17]. Also we did not see any evidence for diffusion of Co atoms into the Al(110) substrate.

In Fig. 6.10, results from the LEED experiment are shown. Sharp spots were obtained prior to any evaporation on the Al(110) surface (Fig. 6.10a). As soon as a small amount of Co was deposited on to the surface the LEED spots completely disappeared. This suggests that the surface has lost long range order, probably associated with alloy formation. Even after 15 ML of Co deposition, the LEED pattern never returned suggesting that there is no long range order present at the interface (Fig. 6.10b).

We performed an XPS photopeak intensity analysis of the Co $2p_{3/2}$ and Al 2p photopeak similar to that discussed for the Al(001) surface in the previous section. We again assumed that we have a simple Volmer-Weber type growth mode in the corresponding two regions. As suggested by the slope in the channeling spectrum (Fig. 6.9), we modeled the growth assuming Co_2Al_5 island growth up to about 5 ML of Co coverage, followed by the growth of Co islands to the final coverage of the experiment. Again, the interplanar distances and adatom planar densities were based on the values of the corresponding assumed compounds, and the island height was determined by forcing the Co coverage to agree with that measured by ion scattering at the break point in Fig. 8. The results of the model calculation are shown in Fig. 6.11 for both the Co $2p_{3/2}$ and Al 2p photopeak lines. The data sets have been normalized to unity intensity at the start (Al) and conclusion (Co) of the experiment.

The experimental curve for Co (open circles) shows a gradual transition throughout the experiment while the experimental curve for Al (closed triangles) shows an abrupt change at about 5 ML of Co coverage. In our model we assumed in region 1 that we are forming a Co_2Al_5-like compound. The Co_2Al_5 has a hexagonal unit cell with dimensions a = 7.656 Å and c = 7.593 Å[22]. There are 28 atoms per unit cell of which 8 are cobalt atoms. The structural parameters used for the fit in Fig. 6.11 are: region 1 (Co_2Al_5) d = 3.804 Å, m = 0.263 x 10^{15} atoms/cm^2 and h = 5 layers; region 2 (Co) d = 2.035 Å, m = 1.838 x 10^{15} atoms/cm^2 and h = 10 layers. But as we can clearly see from Fig. 6.11, the model doesn't agree with the Co experimental curve. The corresponding Al

calculations are not shown. We conclude that we are not forming a structure similar to Co_2Al_5. We also tried a model for CoAl in this region. The parameters that we used for CoAl are d = 2.024 Å, m = 0.863 x 10^{15} atoms/cm^2 and h = 5 layers. The fit is in very good agreement with the experimental curve for both Co and Al, suggesting that the compound formed in region 1 is indeed CoAl as in the case for Al(001). Hence we can conclude that on both Al surfaces, we see similar growth behavior of CoAl films while the HEIS yields suggest a more Al-rich stoichiometry. On the Al(110) surface, the displacement of Al atoms continues up to about 5 ML of Co coverage whereas it stops after about 3 ML on the Al(001) surface. This may be attributed to the fact that the Al(110) surface is relatively more open than the Al(001) surface so that there is a higher probability of Co-Al atom intermixing to occur. Finally, binding energy positions of the Co $2p_{3/2}$ and Al 2p photopeak lines versus Co coverage did not show any observable shift with the limited energy resolution of our analyzer.

Conclusions

In summary, we have performed a high-energy ion scattering/channeling investigation, combined with XPS and LEED, of thin Co films deposited on Al(001) and Al(110) surfaces at room temperature. Deposited Co atoms continuously displaced the substrate atoms for up to about 3 ML of Co deposition on the Al(001) surface and up to 5 ML on the Al(110) surface, indicating that there is some intermixing between the Co and Al atoms occurring at the interface. Based on XPS intensity analysis we conclude that the

CoAl phase formed at the interface with "surface" dechanneling at the interface apparently leading to a higher slope in the ion scattering results. In both cases, after formation of a CoAl-like compound, a pure Co metal film started to cover the interface. Sharp LEED patterns of both clean surfaces disappeared soon after a small amount of Co was deposited. This is an indication of the loss of long range order. On the Al(001) surface, a very diffuse LEED pattern with high background was observed after a deposition of 7.6 ML of Co coverage. On the other hand, the LEED pattern never came back on the Al(110) surface, even after 15 ML of Co deposition. Since there was no significant chemical shift for the Co 2p core level for Co aluminides, we used a Volmer-Weber type growth model for these interfaces, consisting of the initial growth of a thin layer of CoAl alloy, followed by the growth of Co metal. Even though the ion scattering results gave different slopes on the two surfaces, the Volmer-Weber model for the XPS intensity supports the formation of a CoAl like compound at the interface. As we mentioned before the discrepancy in slope is apparently due to the "dechanneling" effect that was shown for the case of Ni on Al(110).[14] In neither case was Co diffusion into the bulk Al substrate observed at room temperature.

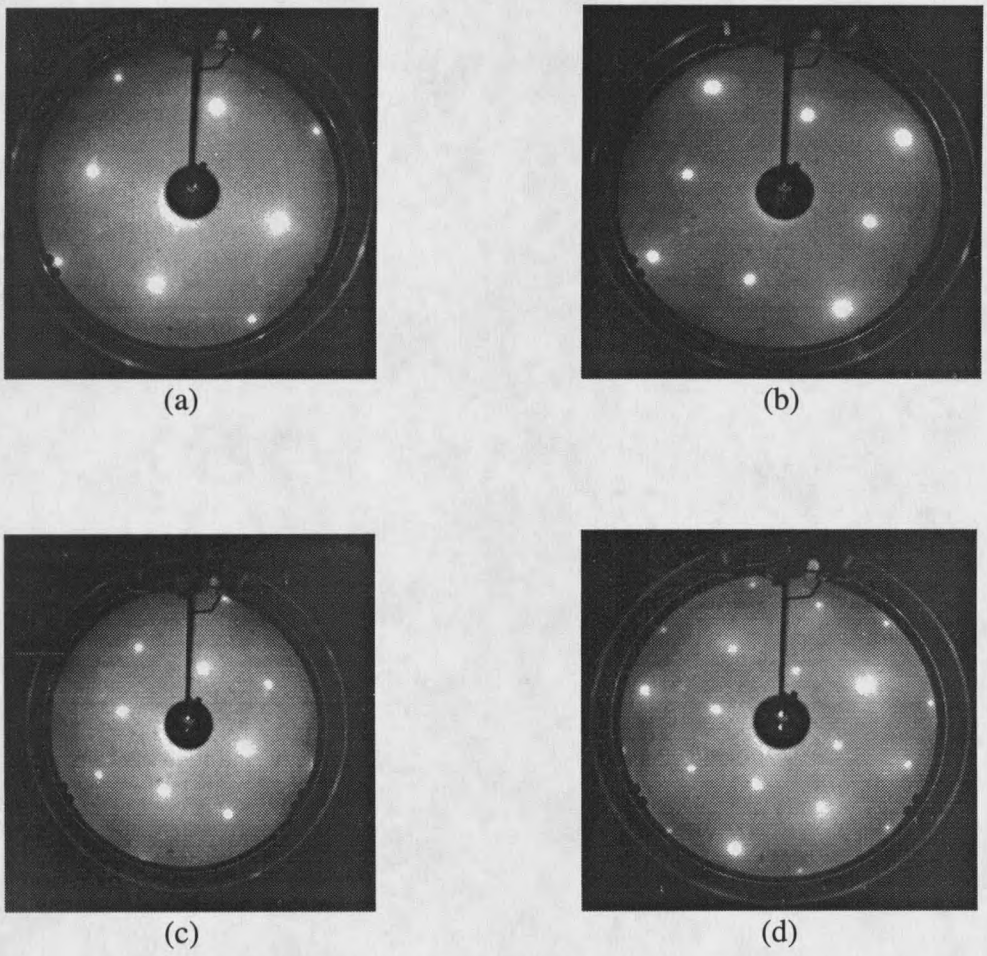

Figure 6.1. LEED patterns for clean Al(001) surface at (a) 35.7 eV (b) 41.4 eV (c) 66.5 eV and (d) 80.8 eV.

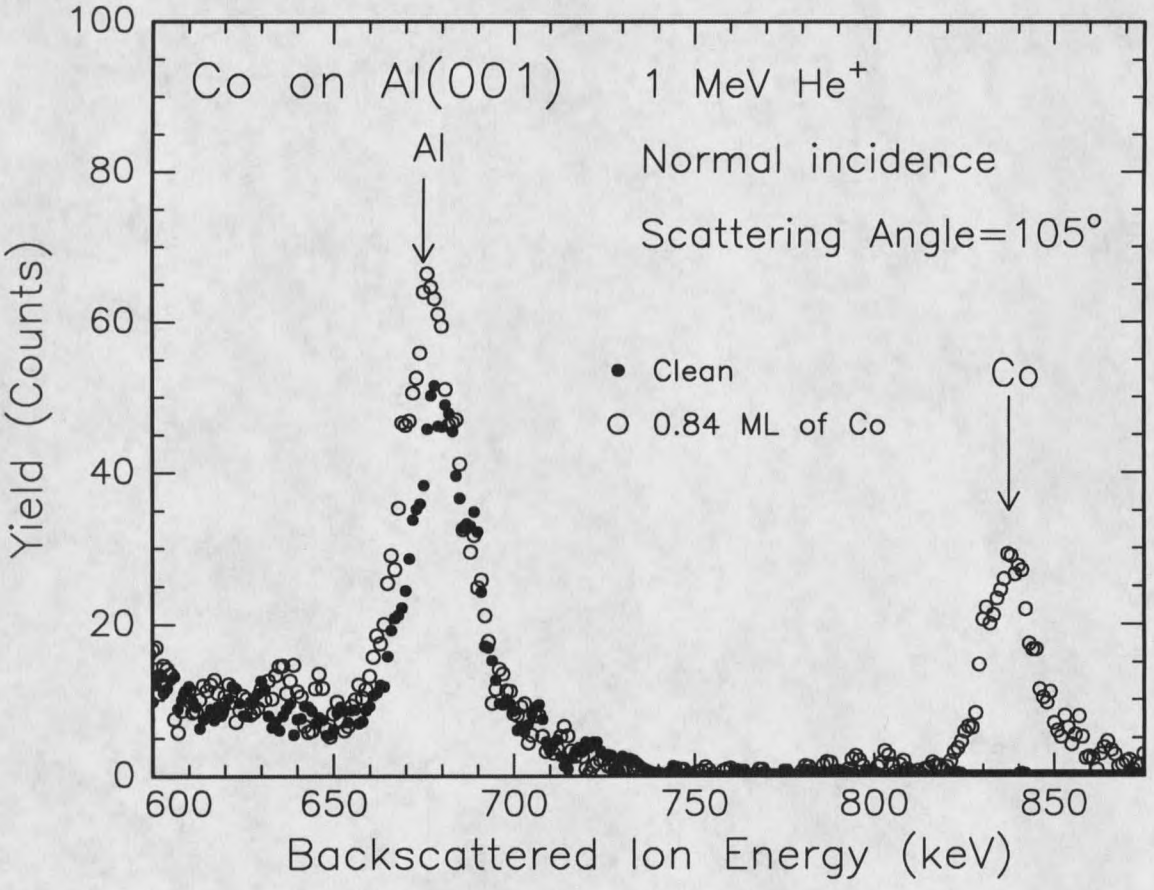

Figure 6.2. Ion scattering spectra for the clean Al(001) surface (solid circles) and for 0.84 ML Co deposited on the Al(001) surface (open circles). The energies for backscattering from Al and Co surface atoms are indicated by the arrows.

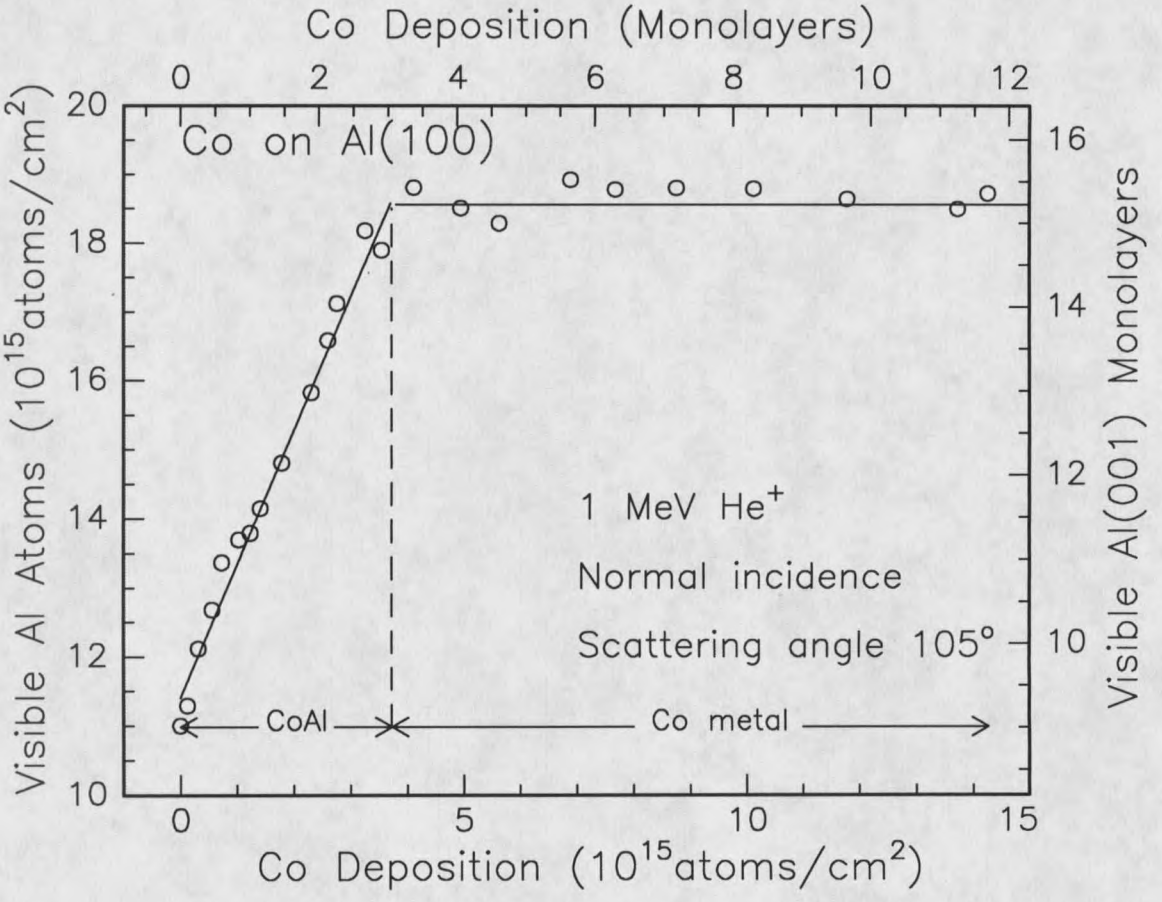

Figure 6.3. Visible Al atoms at 1 MeV incident ion energy, as a function of Co coverage deposited at room temperature on Al(001). Two regions of film growth are indicated. The solid lines are linear fits to the data in the two regions.

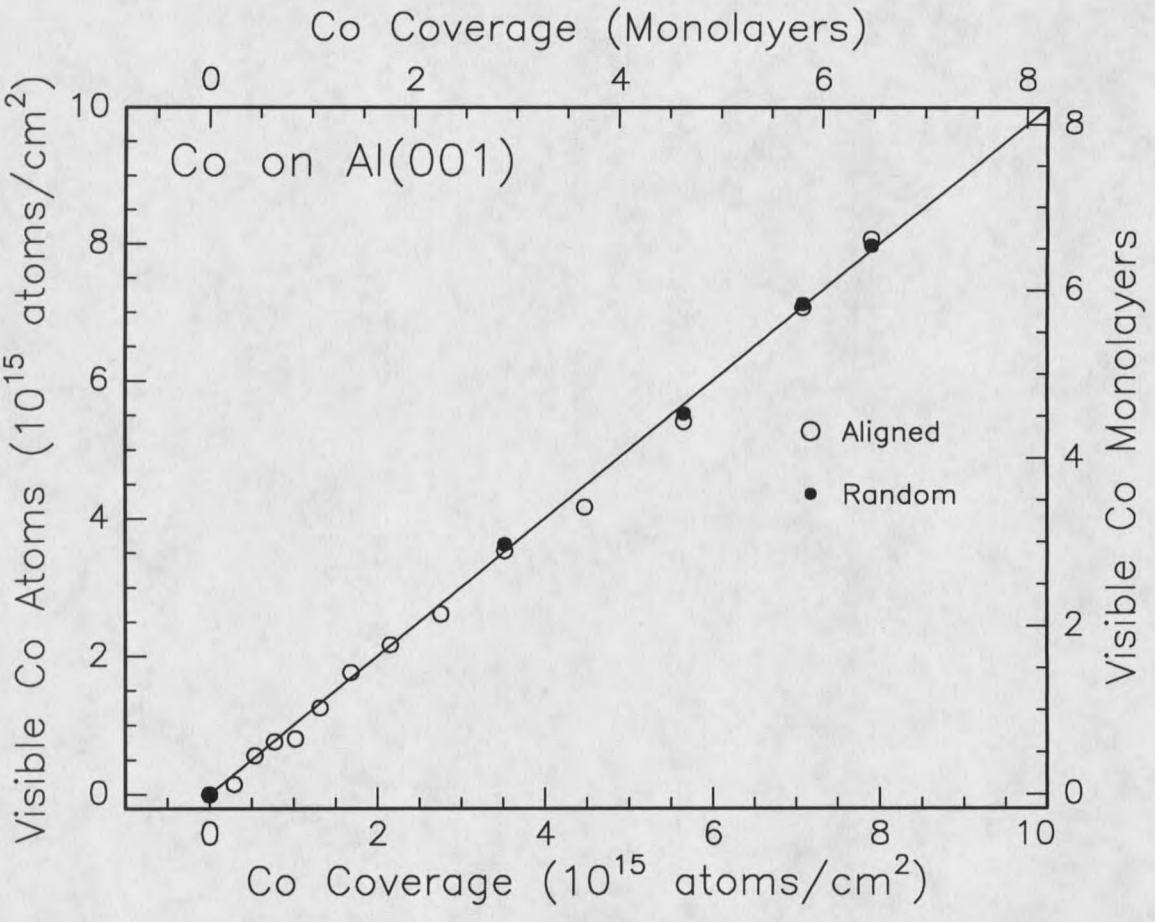

Figure 6.4. Visible Co atoms, at 1 MeV incident ion energy, as a function of Co overlayer coverage. The open circles show the data obtained with the ion beam incident along the [001] direction, and no evidence of shadowing is observed. The solid circles and solid line show the yield from Co atoms measured for the ion beam incident in a random direction.

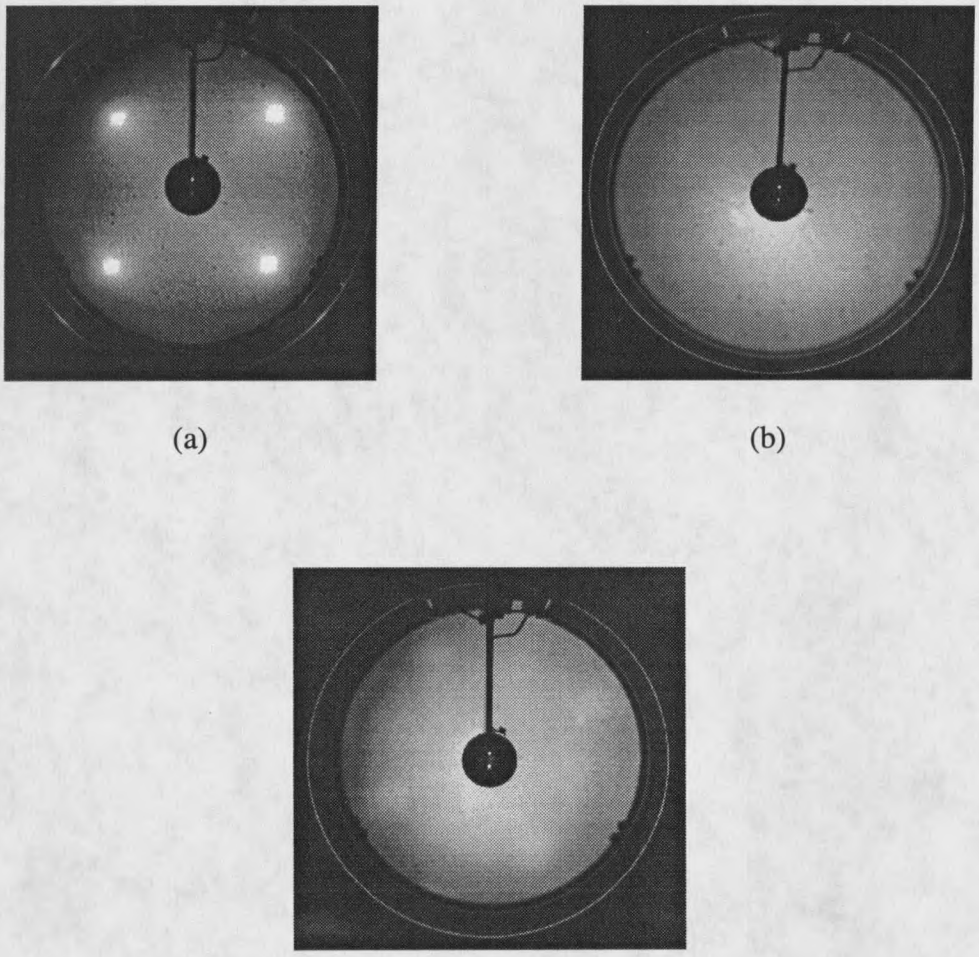

(a) (b)

(c)

Figure 6.5. LEED patterns of the Co/Al(001) system for Co coverages of a) 0, b) 0.5 ML and c) 7.6 ML. The LEED experiments were performed using a 42.8 eV incident electron beam.

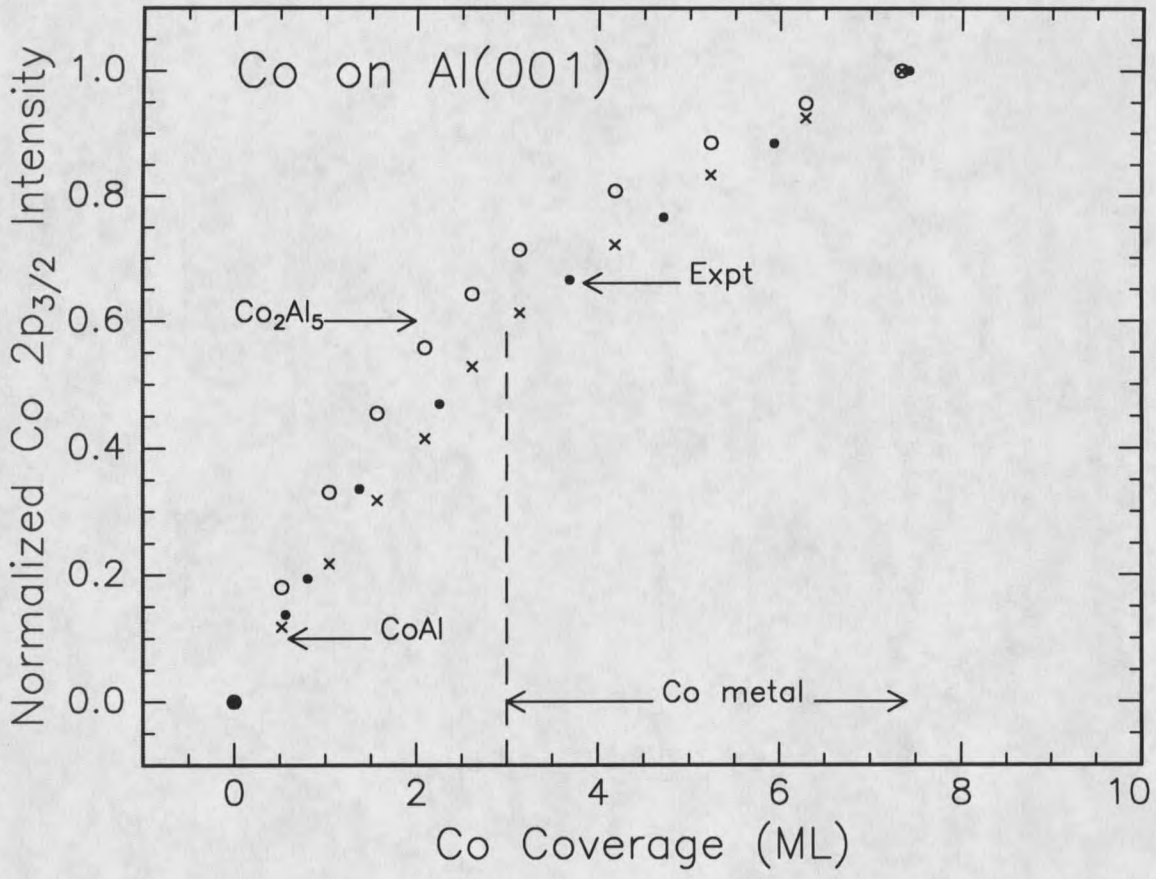

Figure 6.6. Measured XPS intensity for the Co $2p_{3/2}$ photopeak (closed circles) as a function of Co coverage. The Co $2p_{3/2}$ intensity has been normalized to its value at the maximum coverage of our experiment (7.6 ML). The cross (CoAl) and open circles (Co_2Al_5) symbols are the calculated emission intensity for the Volmer-Weber growth model described in the text. Two regions of growth are evident, with a change in film structure around 3.5 ML of Co coverage.

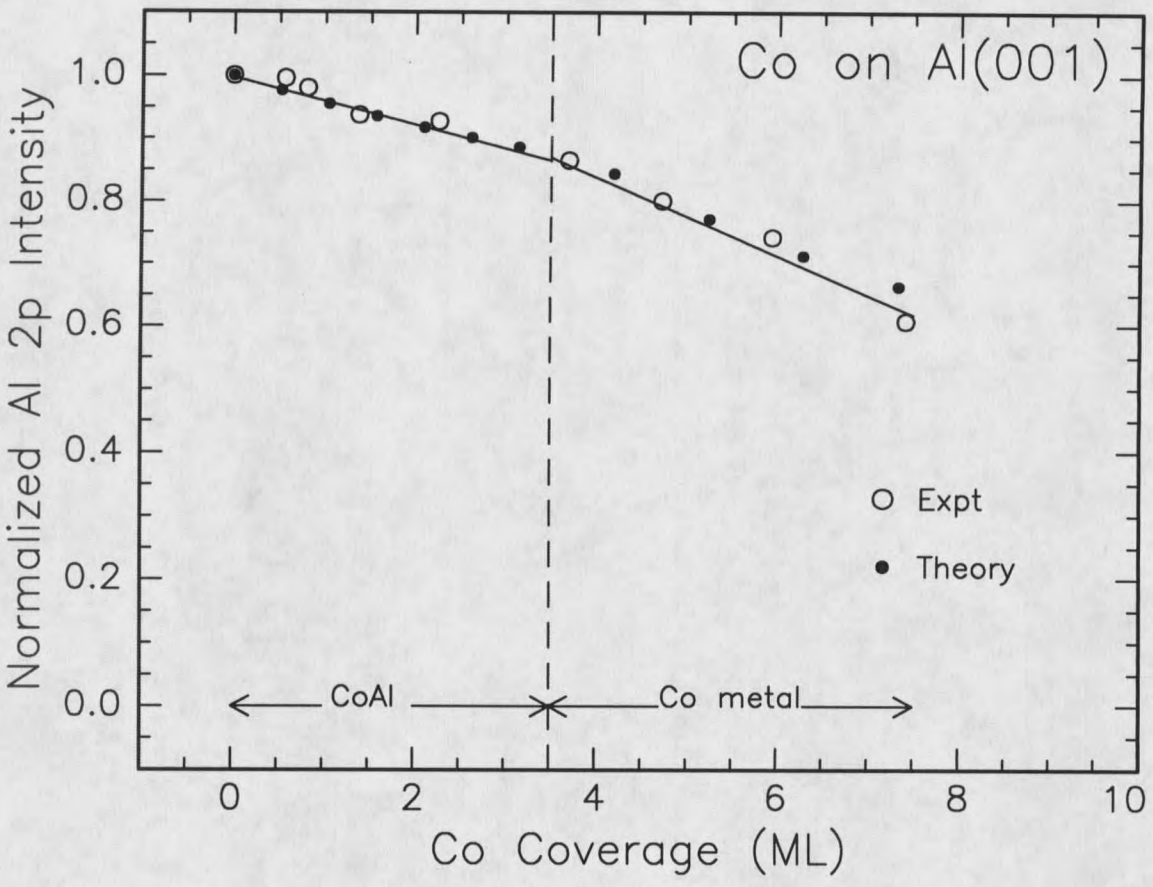

Figure 6.7. Measured XPS intensity of Al 2p photopeak (open circles) as a function of Co coverage. The Al 2p intensity is normalized to the value for the clean surface. Solid lines are provided to guide the eye. The solid circles are the calculated emission intensity for the Volmer-Weber model described in the text. A transition point for the film growth is occurring at around 3.5 ML of Co coverage similar to the Co $2p_{3/2}$ intensity curve.

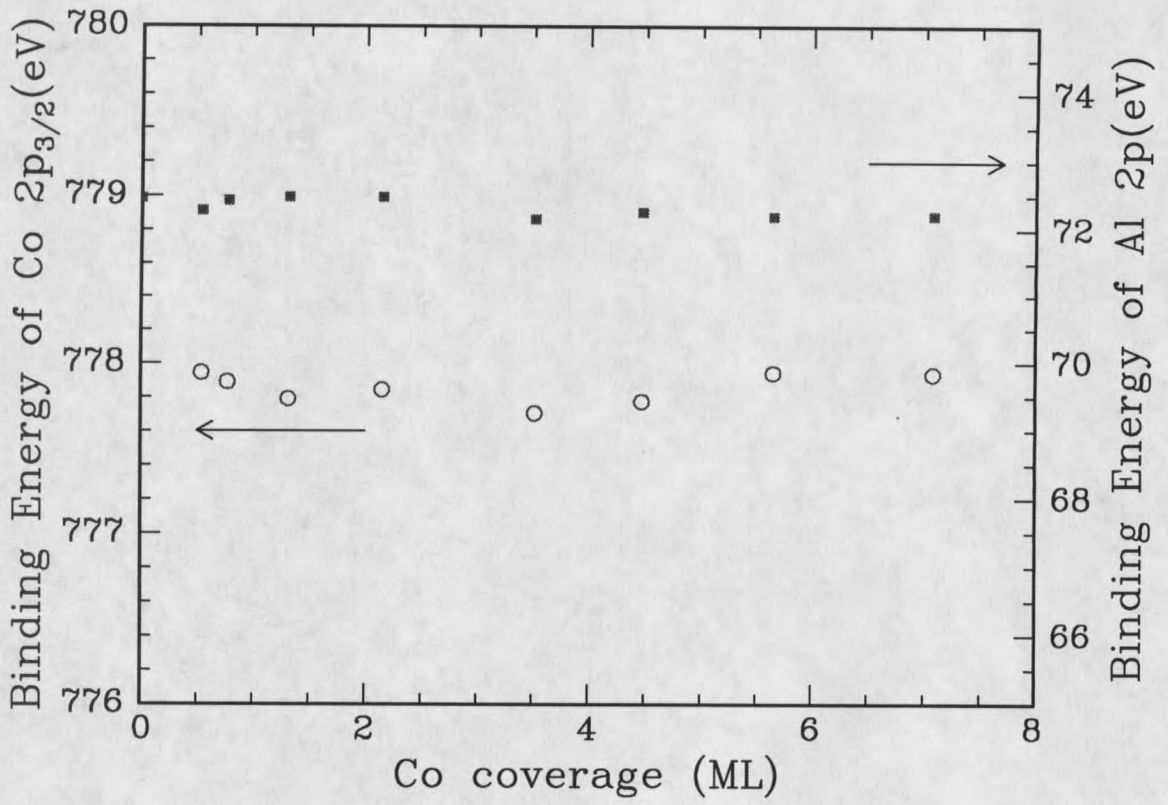

Figure 6.8. The position of binding energies of Co $2p_{3/2}$ line (left axis - open circles) and Al 2p line (right axis - solid circles), plotted as a function of Co coverage. There is a small shift of about 0.25 eV in the Co $2p_{3/2}$ peak position around 3.5 ML of Co coverage whereas Al 2p line position has no significant change at any point during Co deposition.

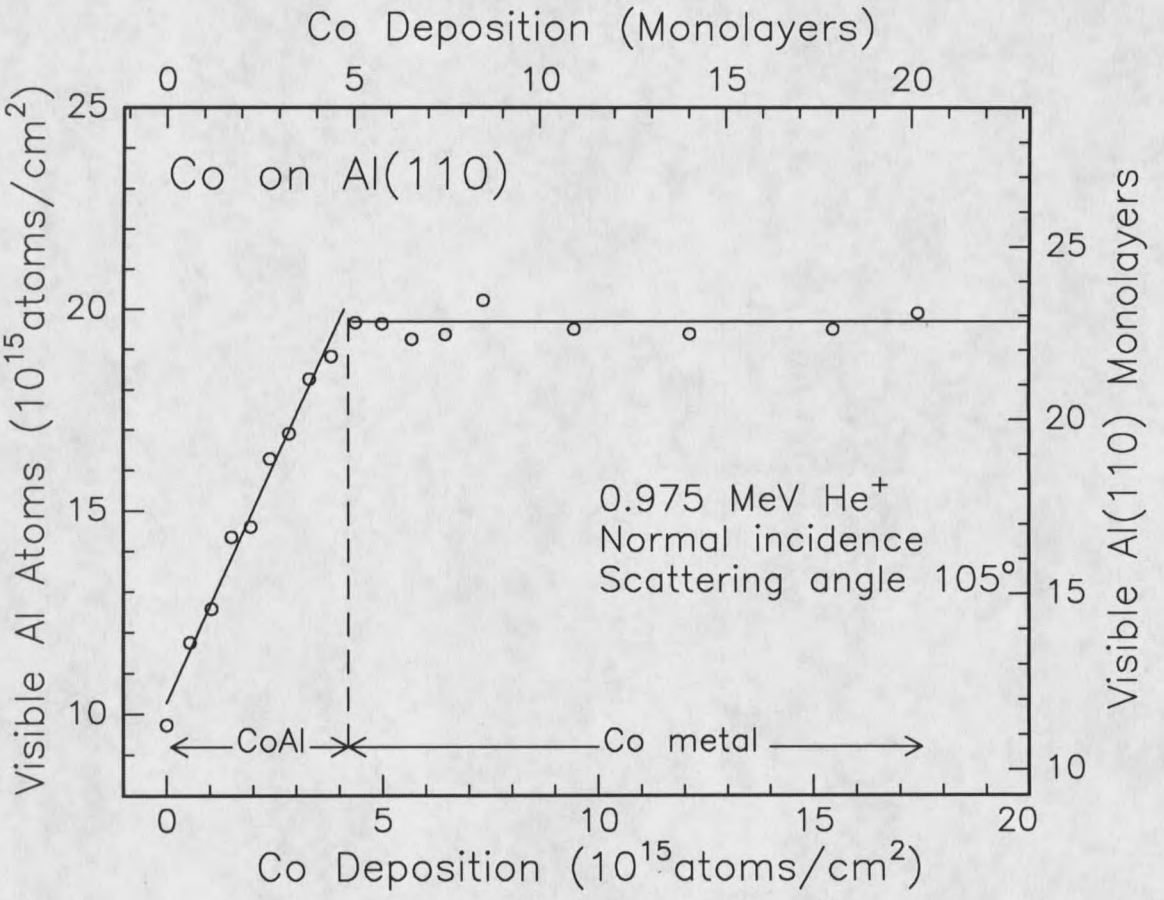

Figure 6.9. Visible Al atoms, at 0.975 MeV incident ion energy, as a function of Co coverage deposited at room temperature on the Al(110) surface. There are two regions of film growth. The solid straight lines are linear fit to the data within the two coverage regimes indicated by the vertical line.

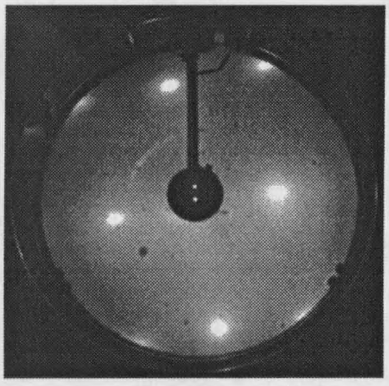

(a)

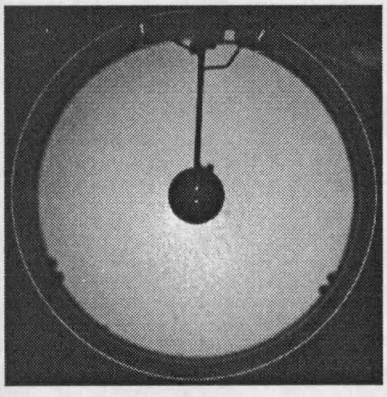

(b)

Figure 6.10. LEED pattern observed for Co on Al(110): a) clean Al with 45.8 eV incident electron energy, and b) Co deposition of 17.39 x 10^{15} atoms/cm^2, 46.2 eV.

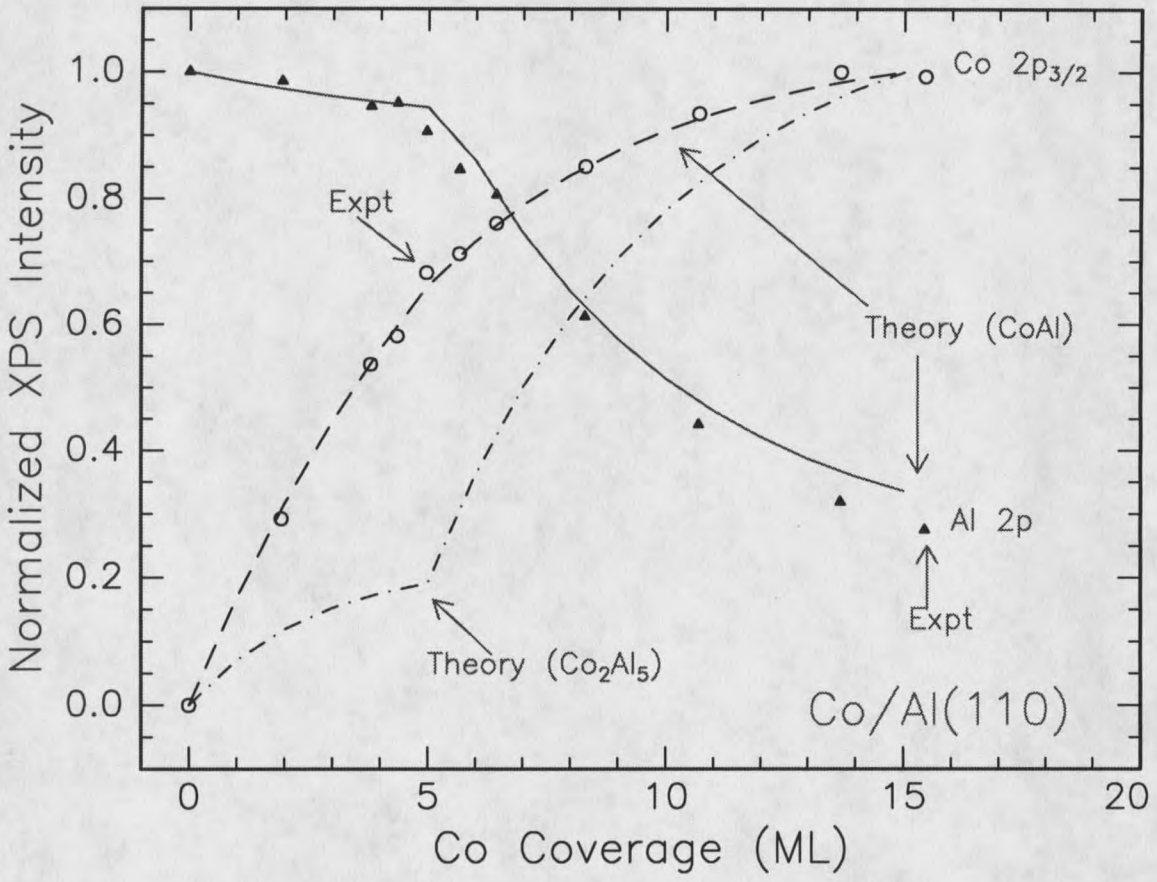

Figure 6.11. Measured (open circles: Co $2p_{3/2}$, solid triangles: Al 2p) and calculated (dotted lines: Co_2Al_5 and CoAl) XPS intensities of both Co and Al 2p lines as a function of Co coverage. The theoretical points were calculated using a Volmer-Weber growth model discussed in the text with two different growth regimes. In region 1, either CoAl or Co_2Al_5 like compounds were assumed to grow separately.

REFERENCES

1. E. G. Bauer et. al, J. Mater. Res., Vol5, No. 4, (1990) 852.
2. Jan H. Van der Merwe and E. Bauer, Phys. Rev. B39, (1989) 3632.
3. See, for example, *Epitaxial Growth*, edited by J. W. Matthews (Academic Press, New York, 1975).
4. L. Z. Mezey and J. Giber, Jpn. J. Appl. Phys. 21, (1982) 1569.
5. V. Shutthanandan, Ph.D Thesis, Montana State University, 1994.
6. M. Hansen, *Constitution of Binary Alloys*, edited by K. Anderko, (McGraw-Hill, New York, 1958).
7. F. Z. Cui, J. F. Wang, Y. D. Fan and H. D. Li, J. Appl. Phys., 70, 3379(1991).
8. Hong Li and B. P. Tonner, Phys. Rev. B, 40, 10241(1989).
9. J. W. Mayer and E. Rimini, *Ion Beam Handbook for Material Analysis*, Academic Press, New York, 1977.
10. D. S. Gemmel, Rev. Mod. Phys. 46, (1974) 129.
11. E. J. Van Loenen, M. Iwami, R. M. Tromp and J. F. W. van der Veen, Surf. Sci. 137, (1984) 1.
12. L. Stensgaard, L. C. Feldman and P. J. Silverman, Surf. Sci. 77 (1978) 513.
13. L. C. Feldman and J. W. Mayer, *Fundamentals of Surface and Thin Films Analysis*, North-Holland, Amsterdam (1986).
14. V. Shutthanandan, Adli A. Saleh and R. J. Smith, J. Vac. Sci. & Tech. **A11** (1993) 1780.

15. V.Shutthanandan, Adli A. Saleh, A. W. Denier van der Gon and R. J. Smith, Phys. Rev B 48, (1993) 18292.

16. V. Shutthanandan, Adli A. Saleh, N. R. Shivaparan and R. J. Smith, Surf. Sci. 350, (1996) 11.

17. N. R.Shivaparan, V. Shutthanandan, V.Krasemann and R. J. Smith, Surf. Sci. (in press).

18. M. Vos, S. G. Anderson and J. H. Weaver, Phys. Rev. B39 (1989) 3274.

19. N. R. Shivaparan, V. Krasemann, V.Shutthanandan and R. J. Smith, Surf. Sci. 365 (1996) 78.

20. S. Ossicini, R. Memeo and F. Ciccacci, J. Vac. Sci. Technol. A 3 (1985) 387.

21. P. A. Schultz and J. Davenport, Scrip. Met. 27 (1992) 629.

22. Newkirk, P. J. Black, and A. Damjanovic, Acta Cryst. 14 (1961) 532.

CHAPTER 7

EPITAXIAL GROWTH OF THIN Ag FILMS ON Al(001) AND Al(110) SURFACES

Introduction

Experimental results concerning the structure, growth, and properties of transition-metal thin films have proliferated in recent years[1]. These thin-film-substrate systems are often found to exhibit transformations in their properties as a function of both coverage and temperature. Aluminum is frequently used in metallizations for integrated circuits. There have been many investigations of the interdiffusion and intermetallic phase formation process between Al and metals. In previous chapters we investigated the phase formation and the growth in the Pd-Al (Chapter 4), Fe-Al (Chapter 5), and Co-Al (Chapter 6) thin-film systems. In all the above systems, the deposited metal atoms seem to mix and displace the substrate Al atoms from their equilibrium positions up to a certain coverage at room temperature. The object of this chapter is to extend our work to the Ag-Al thin-film system and investigate the phase formation and film growth. Furthermore, Smith[2] et. al. have shown that neither the aluminide formation energy, nor the lattice mismatch alone serve as useful parameters to predict epitaxial growth. Instead they found that the relative size of the adatoms correlates well with the growth behavior for transition metals (Ti, Pd, Ni and Fe) on Al surfaces. Atoms with radii larger than that of Al form

overlayers while atoms smaller than Al atoms form surface alloys. Hence we chose Ag, which has a larger atomic diameter than the Al substrate atom, to test the model. Previous studies by Frick and Jacobi using AES, LEED and angle-resolved UPS to study the growth and electronic structure of ultrathin Ag films on Al(111)[3] suggest that at room temperature Ag grows in the Stranski-Krastonov mode, whereas at 520 K substrate temperature, Ag grows epitaxially. On the other hand Egelhoff has studied thin Ag films on Al(001) using XPS[4,5]. In this case, silver was observed to produce a (5 x 1) LEED pattern at submonolayer coverages, to exhibit a disordered phase between 2 and 10 ML, and to order into a (1 x 1) epitaxial structure around 10 to 20 ML. The electronic structure, as determined by the 4d band width and the core level binding energies, does not converge to that of bulk Ag until about 20 ML coverage. Furthermore, prior to the onset of epitaxy the Ag was in the form of small. closely packed clusters which are quasi-equilibrium structures with a diameter that depends on the amount of silver metal on the Al(001) surface. As a final example, thin silver films deposited onto an InP(001) - p(2 x 4) surface at room temperature were found to grow epitaxially in the Stranski-Krastanov (SK) mode along the (110) direction on the InP(001) surface[6]. In the above study, AES analysis indicates that the surface composition of Ag increases gradually, while that of In and P decrease gradually as the Ag film thickness increases. It is found that the LEED patterns for the Ag surface show faint p(1 x 1) spots at an areal density of $4.8 \times 10^{15}/cm^2$ and no spots at larger thickness. In addition, RBS-channeling experiments using 1.5 MeV He^+ ions show that the minimum yield for the Ag films incident along the [100]

direction of the InP substrate decreases down to 36% and then increases up to 73% as the thickness of the Ag films increases. In this chapter we report the results of a characterization of Ag layers deposited onto Al(001) and Al(110) surfaces at room temperature using high energy ion scattering/channeling (HEIS), x-ray photoelectron spectroscopy (XPS) and low energy electron diffraction (LEED). It is found that Ag layers grow epitaxially on both surfaces.

Experimental setup

A conventional UHV system, described in previous chapters, was used in this work. Its base pressure is 1.2×10^{-10} Torr. This apparatus was equipped with high energy ion scattering/channeling, x-ray photoelectron spectroscopy (XPS), and low energy electron diffraction (LEED). The Al single crystals used in these experiments were cut and oriented to within 0.5° of the desired surface orientation. The surfaces were mechanically polished with additional chemical etching prior to loading them into the UHV chamber. They were cleaned (sputter-anneal cycles) until the aluminum oxide associated with the Al 2p peak in XPS was completely removed from the spectrum. The Ag metal was deposited by heating a 0.25mm W filament wrapped with 0.25mm high purity Ag wire. During the metal deposition the sample temperature did not rise above room temperature. The Al SP areas were monitored during the Ag deposition. Silver (3d) and Al core levels and Ag valence photopeaks were also monitored during the film growth. A beam of Al-K_{α} x-rays was used as the excitation source in the photoemission

experiments. A fixed pass energy of 50 eV, and a scanning rate of 0.1 eV/sec were used. The angle between the sample normal and the electrostatic analyzer was fixed at $\theta = 30^{\circ}$. Film deposition, channeling measurements, and XPS measurements were all performed without moving the sample. Occasionally the sample was rotated slightly to measure random spectra. This arrangement helped in maintaining the sample alignment with the ion beam. LEED was performed during film deposition at various stages and was used to complement the channeling and XPS peak intensity measurements.

Results and discussion

Al(001) surface

HEIS-channeling measurements:

After sputter cleaning and annealing the Al(001) crystal, it was oriented such that the ion beam was normal to the surface, i.e., the beam was incident in the [001] direction. The crystal was aligned by minimizing the integrated backscattering yield in an energy window behind the surface peak. The angular yield curve shown in Fig. 7.1 is obtained by plotting the counts in the energy window as a function of tilt angle for the clean Al(001) surface. The energy of the incident helium ions was 1 MeV. The experimental value for the half-width or angle, $\psi_{1/2}$, is 0.52° as compared to the theoretical value of 0.48°, calculated using equation 2.12. The measured value for the normalized, minimum yield, χ_{min}, was 3.65%. The calculated value for χ_{min} is 3.70%, using a one dimensional thermal vibration amplitude of 0.105 Å and a crystal lattice constant of 4.05 Å[7]. The good

agreement between the experimental and calculated values for $\psi_{1/2}$ and χ_{min} confirms the presence of good crystalline order in subsurface crystal planes.

In Fig 7.2 we show HEIS channeling spectra of backscattered ions in the regions of the Al and Ag surface peaks before and after a deposition of 4.6 ML Ag on the Al(001) surface. Here 1 ML of Al(001) corresponds to a surface density of 1.219 x 10^{15} atoms/cm^2. From Fig. 7.2 we can see that the Al surface peak has decreased after the Ag deposition on the surface, indicating that Ag surface atoms are shadowing Al atoms at the interface. That is, deposited Ag atoms are sitting on top of substrate Al atoms causing shadowing from the incident He^+ ions. In other words, fewer Al atoms are visible to the incident ion beam in the presence of Ag atoms at the surface, and the Ag atoms are forming an epitaxial overlayer.

Figure 7.3 illustrates the basic growth characteristics of the Ag film on the Al(001) surface, as measured using ion channeling. The open circles in the figure represent the experimental data. For the first monolayer of Ag coverage, the trend in the surface peak area (SPA) is not very clear, and may be assumed to be constant to within the experimental uncertainty. Similar results are observed for Ti on the Al(001)[9] surface, where we believe Al-Ti site exchange may occur for the first monolayer on that surface. A decrease in the Al SPA was observed up to about 7 ML of Ag coverage, where the number of visible Al atoms reaches a minimum value of 3 ML. The Al SPA has totally disappeared after this point. The solid squares in Fig. 7.3 show the results of computer simulations[8] for the scattering yield from a Ag layer which grows layer-by-layer. The

Al(001) interplanar distance of 2.025 Å was used in simulating the overlayer along with a vibrational amplitude of 0.105 Å. The disagreement with the experiment at the early stages of growth supports the previous results by Egelhoff[4] suggesting that the growth of Ag films on the Al(001) surface is not purely layer-by-layer but may be an intermediate case between agglomeration into very large clusters (which occurs when the bonding between overlayer and substrate is weak) and a layer-by-layer growth mode (which occurs when the overlayer is strongly bonded to the substrate).

A similar plot of visible Ag atoms as a function of Ag coverage gives additional insight about the overlayer formation. In Fig. 7.4 we plot the number of Ag atoms visible to the incident ion beam in the normal channeling direction as a function of Ag coverage, determined by the Ag coverage measured in the random direction. The solid line in Fig. 7.4 is drawn through the solid circles showing the Ag yield measured in the random direction. Evidence of significant Ag shadowing is observed for coverages greater than 5 ML, where the Ag yield in the aligned direction falls well below that measured in a random direction. The closed triangles indicate the yield expected for a layer-by-layer growth of a Ag film as calculated using the VEGAS[8] simulation code. The agreement is quite good, supporting the interpretation of epitaxial growth.

LEED and XPS measurements:

The evolution of a LEED pattern in the different stages of deposition of foreign atoms on a clean substrate surface can sometimes provide valuable information about the

growth mode. In the present study, the LEED patterns were used to explore the growth morphology. Fig. 7.5(a) shows the LEED pattern obtained from the clean Al(001) surface. The sharp LEED spots in a square pattern reflect the (001) symmetry, and also support the cleanliness of the Al surface. The low electron beam kinetic energy of 51.6 eV was used. Pictures of the LEED spots are shown in Figures 7.5 (b)-(f) for Ag coverages of 0.2, 2.5, 4 and 30 ML and after heating the sample at 200° C respectively. The (5x1) LEED pattern in Fig. 7.5 (b) appears to be at its maximum intensity at sub-monolayer coverages of Ag. It could result from a Ag overlayer with every fifth row of Ag atoms missing (0.8 ML). The decline in (5x1) intensity above 1 ML suggests that Ag atoms adsorb in random sites not ordered with respect to the substrate (Fig. 7.5 (c)). After about 2.5 ML of Ag deposition, the LEED pattern has completely disappeared, indicating that the long range order is completely disrupted. The Ag deposits begin to reorder around 4 ML (Fig. 7.5 (d)) and by 30 ML exhibit good epitaxy in registry with the Al(001) surface (Fig. 7.5 (e)). In this region, the overlayer pattern was always oriented in the same manner as the substrate LEED pattern, despite the fact that from 1.3 ML to 3.6 ML no LEED pattern was detectable. The overlayer still retains memory of the substrate orientation even though it has lost the long range order between 1.3 and 3.5 ML of Ag coverage. This may be due to the preservation of short range order during the Ag deposition, which serves as a seed for the growth of the ordered overlayer at higher coverages. Finally, no change in the LEED pattern was observed upon heating the sample at 100° C, indicating that diffusion of Ag atoms into the bulk substrate did not

start to occur. But when the sample was heated at about 200°, the LEED pattern was (Fig. 7.5 (f)) completely obliterated. Furthermore 7.5% of the total Ag atoms were seen to diffuse into the Al substrate after annealing at 200° C. Finally it should be emphasized that all LEED patterns were acquired using slightly different electron beam energies in order to accentuate the intensity contrast.

Fig. 7.6 displays the angular yield curves for clean Al, 9 ML and 30 ML of Ag coverages respectively. It is very clear that the Ag overlayer after 9 and 30 ML of deposition is in perfect registry with the substrate and hence supports the LEED observations.

XPS measurements were utilized to examine the chemical bonding and structure of the interface during the deposition of Ag on the Al(001) surface. Figures 7.7(a) and (b) show Al and Ag photopeaks respectively. These two XPS spectra were taken after the deposition of 2.8 ML of Ag on the surface. These figures illustrate the XPS peak fitting and the Shirley background subtraction method used to extract the net areas in both cases. This non-linear least-squares fitting of the yield is explained in detail in Appendix. The Al 2p photopeak (72.65 eV) was fit using one Gaussian component plus an error function background. Similarly, the Ag $3d_{5/2}$ and $3d_{3/2}$ peaks were each fit to a Gaussian component and an error function background. The separation between the two Ag peaks (6 eV) was fixed using the known spin-orbit splitting[10]. The centroids, amplitudes and the full-widths at half maximum were allowed to vary during the nonlinear least-squares fitting procedures. The amplitudes of the error functions representing the background

were also allowed to vary, while their positions were set to be identical with the Gaussian peak centroids.

Figure 7.8 presents the change in the Al 2p (open triangles) and Ag $3d_{5/2}$ (open circles) core level intensities as a function of Ag coverage. The Al 2p XPS intensity was normalized to the intensity of the clean surface, while the Ag intensity was normalized to its value at the maximum coverage in our experiment (30 ML). The smooth exponential changes of Al 2p and Ag $3d_{5/2}$ XPS intensity suggest that the deposited Ag atoms are not agglomerating to leave areas of uncovered Al. This would imply that the growth mode could be more close to the Frank-van der Merwe (FM growth) where the deposited Ag atoms grow layer-by-layer. Furthermore these data rule out the possibility of a Volmer-Weber type growth where one assumes that the Ag atoms aggregate to form three-dimensional islands on the surface. However, it is clear from channeling and LEED results that the situation is more complex than a simple layer-by-layer growth mode. A further attempt was made to consider other possible growth modes of Ag atoms on the Al(001) surface at the early stages. We assumed an exponential decay for the intensity of the photoelectrons passing through the successive layers of the substrate-adsorbate system, with a mean attenuation length λ, calculated using the formula $\lambda=1430E^{-2}+0.54E^{1/2}$, where E is the kinetic energy of the electrons in eV[11]. The values of λ for Al and Ag are 20.3 Å and 18.1 Å, respectively. Next we assumed a uniform and homogeneous substrate, not modified by the deposition of Ag atoms. This means that no interdiffusion between adsorbate and substrate atoms takes place. In FM growth, the

deposited Ag film will be composed of h complete layers plus the topmost one filled by a fraction x, with $0 \leq x \leq 1$. The attenuation of the Al 2p and the growth of the Ag $3d_{5/2}$ photopeak intensity after the completion of h monolayers, plus an additional partial coverage x, of the topmost layer, are given by[12]

$$I_{Al}(h,x) = \frac{w_{Al}^{h}(1-x+xw_{Al})}{(1-w_{Al})}; \qquad I_{Ag}(h,x) = \frac{(1-w_{Ag}^{h})(1-x+xw_{Ag})}{(1-w_{Ag})} + x$$

Here, I_{Al} and I_{Ag} are the Al and Ag photopeak intensities, normalized to unity intensity at the start (Al) and conclusion (Ag) of the experiment; w_{Al} and w_{Ag} are attenuation factors expressed as $\exp(-d/\lambda \cos\theta)$ to represent the decrease in intensity of photoelectrons where d is the interplanar distance and the factor $\cos\theta$ corrects for the non-normal emission direction. The values of w are 0.891 (Al) and 0.877 (Ag). The calculated XPS intensities for this FM model are shown for both Al and Ag (dotted lines) in Fig. 7.8. Clearly, the simulated Al intensities do not follow the experimental XPS intensity curves up to about 10 ML of Ag coverage indicating that the growth of Ag atoms is not layer-by-layer on the Al(001) surface. Furthermore an important point in such models of photoemission intensity is that a flat film gives the greatest possible attenuation of the substrate photopeak intensity. Any combination of islands or disordered structure will lead to a larger value of Al intensity than that calculated for a layer-by-layer growth. Even though the disagreement between the experimental and theoretical values is small, the FM growth model calculation results do fall below the experimental points up to about 10 ML of Ag coverage.

Fig. 7.9 shows the valence band X-ray photoelectron spectra (XPS) for different coverages of Ag on Al(001) at room temperature. The peaks may be taken to derive exclusively from the Ag 4d bands, since the Al valence band is very weak and flat over this energy range and only noticeable in the lowest coverage spectra . Below about 3 ML of Ag coverage the d-band is roughly symmetrical. Between 7 and 12 ML the peak splitting begins to start. Between 12 and 30 ML the d-band converges slowly on its bulk character. The spectra in Fig. 7.9 indicate clearly that the full bulk Ag band structure has developed at around 24 ML of Ag coverage and certainly not at low coverages as predicted by theoretical calculations. In other words, the band width of various metals as a function of the number of layers , which usually show convergence occurring around 4 monolayers of thickness using theoretical calculations, is inconsistent with this slow transformation process. One example is Ag on Al(110) which will be discussed in the next section. Furthermore, Ag on Si[13], Au on Ni[14], and Cu on Ni[15] experimental data are good examples of this case and show convergence on the bulk valence band width around 4 monolayers thickness.

Fig. 7.10 is a plot of the full width at half maximum (FWHM) of the Ag 4d valence band as a function of Ag coverage. The FWHM values were calculated after subtracting the background. Also they were allowed to vary during the fitting procedure. From Fig 7.10 we can clearly see that the FWHM does not converge on its bulk value until about 20 ML of Ag coverage.

In Fig 7.11, the binding energy of the Ag 4d valence band centroid is plotted as a function of Ag coverage. The bulk value for the Ag valence band energy (about 5.4 eV) is reached only after 15 ML of Ag coverage which emphasizes again that the growth mode of Ag layers on Al(001) is not layer-by-layer. A total shift of about 0.80 eV is measured for the 4d centroid which is in good agreement with Egelhoff's[4] value of 0.75 eV. Similar behavior is also seen in the binding energy of the Ag core levels, which is shown in Fig. 7.12. The total shift in binding energy is about 0.75 eV which is very close to the Ag 4d valence band shift. In other words, the shift in the core level binding energies of Ag is almost exactly equal to the shift in the binding energy of the centroid of the d-band. In fact, other noble metals such as Au and Cu have shown similar behavior on the Al(001) surface[5]. A more convincing model for the Ag core level shift is that the Ag is clustering on the Al(001) surface. The support for the model of clustering by Ag atoms comes not only from the significant shift in core level binding energy (0.75 eV) in the present study but also from the work of Roulet, et. al.[16]. They used XPS and transmission electron microscopy to correlate the magnitude of the splitting in the Au valence band with cluster diameter. Although their work was done on a NaCl substrate, the Au valence band splitting depends primarily on the average environment of the Au atoms, and should be influenced by the substrate a relatively little amount. In addition, there is a strong similarity in behavior for other noble metals like Au and Cu on the Al(001) surface[5] suggesting that Ag atoms are clustering. Furthermore, metal clusters are well known to display larger core binding energies than the bulk metal[16,17] and granular

films of one metal on another are well-known in epitaxial studies[18]. Diffusion of Ag atoms into the Al substrate is extremely slow at room temperature. However, Ag atoms diffused readily into bulk Al above about 200° C. The disappearance of the LEED pattern (Fig. 7.5 (f)) after heating the sample at 200°C confirms the diffusion of Ag atoms into the bulk and hence the loss of long range order. In summary, all the above observations from HEIS (disagreement between the experiment and Monte Carlo simulation), XPS (experimental intensity points do not follow layer-by-layer model growth curves) and LEED (initial (5x1) pattern and the disappearance of pattern between 1.3 and 3.5 ML of Ag) strongly support the idea that the growth characteristics of Ag atoms on the Al(001) surface can not be simply layer-by-layer (at least up to about 10 ML) but a formation of clusters of Ag atoms which agglomerates into large clusters as deposition of Ag continues.

Al(110) surface

We performed analyses similar to those just described for the Al(001) surface as a function of Ag coverage on Al(110) surfaces. This particular system has not been previously studied to our knowledge. For this system, the growth behavior of Ag atoms seems to be layer-by-layer (FM growth) rather than forming clusters which was observed for the Al(001) surface at the early stages of growth. A similar layer-by-layer growth was observed for Ti on Al(110) surfaces[19]. In that case a flat, pseudomorphic Ti film forms initially on the Al(110) surface up to a critical thickness of 5 ML. The Ti-Al interface is abrupt and no evidence for displacement of Al atoms is observed. As we pointed out

earlier, both Ti and Ag have atomic radii bigger than that for Al and it is expected that they will not intermix with the substrate atoms on Al(110) surfaces[2]. Indeed this was observed in the Ag case as presented in the next section.

Fig 7.13 presents He^+ ion scattering spectra at 0.86 MeV incident ion energy after the deposition of Ag on the Al(110) surface. The open circles represent the spectrum taken at random incidence while the closed circles represent that for incidence along the [110] direction. It is clear that a smaller Ag surface peak area is seen in the aligned geometry. This difference in the hitting probability is characteristic of Ag shadowing and thus indicative of the growth of an ordered overlayer. No Ag shadowing was observed for coverages less than 4 ML. After the completion of the fourth layer, shadowing is observed and this difference increased as a function of coverage throughout the experiment where more than two Ag atoms were completely shadowed at a coverage of 13 ML (Fig 7.13).

In Fig. 7.14, we plot the Al surface peak area (visible Al atoms) as a function of Ag coverage on Al(110), determined by the Ag surface peak area. The Al SP area decreased sharply with Ag deposition, indicating a lower Al hitting probability. This is attributed to the shadowing of the surface Al atoms by Ag atoms. The decrease in the SP area continues for coverages up to about 9 ML when the Al hitting probability reaches a minimum value of about 2 ML. The Al(110) surface density of 0.862×10^{15} atoms/cm^2 per monolayer was used to convert the Ag coverage into equivalent Al(110) monolayers. The solid circles in Fig. 7.14 show the results of computer simulations for the scattering

yield from a Ag layer. In these simulations, the Ag atoms were placed on Al lattice sites above the surface, in a layer-by-layer fashion, with the Al(110) interplanar distance of 1.432Å. The results of these simulations at various Ag coverages are in reasonable agreement with the measured yields, supporting our interpretation of an epitaxial overlayer.

Even though the ion scattering results strongly suggested the growth of an ordered Ag surface layer, we monitored any variations in the LEED pattern to verify the nature of this growth. Fig. 7.15 displays the LEED patterns observed at various Ag coverages. Sharp spots in a rectangular pattern were obtained, reflecting the (110) surface symmetry, before any Ag evaporation (Fig. 7.15a). The low electron beam kinetic energy of 47.3 eV was used to probe the structure of the topmost surface layer. Ag deposition did not induce any significant changes in the LEED pattern up to the maximum coverage of about 9 ML, indicating the formation of an ordered layer at the interface. It also confirms that the formed Ag-Al surface layer has a rectangular symmetry similar to that the substrate.

As we saw in the previous section, the variation in the XPS photopeak intensities can also be used to help understand the structure of the overlayer. Hence we performed an XPS photopeak intensity analysis of the Al 2p and Ag $3d_{5/2}$ photopeaks similar to that discussed for the Al(001) surface. Open circles and triangles in Fig. 7.16 represent the variation of Al 2p and Ag $3d_{5/2}$ intensities as a function of Ag coverage respectively. The intensity of the Al 2p photoelectrons decreased by a factor of 40% after the deposition of about 5 ML of Ag. After this point the smooth drop in intensity reaches the minimum

value of 10% when the deposition reaches 25 ML. On the other hand the Ag $3d_{5/2}$ photopeak intensity shows a smooth exponential variation as a function of Ag coverage. The data sets have been normalized to unity intensity at the start (Al) and conclusion (Ag) of the experiment. We again assumed that we have a simple Frank van der Merwe type growth model in this case. The results of model calculation for both the Al 2p and Ag $3d_{5/2}$ (dashed lines) are shown in Fig. 7.16. This model calculation seems to agree quite well with the data, supporting the layer-by-layer growth mode suggested by the ion scattering and LEED results. The structural parameters used for the fit in Fig. 7.16 are: d_{Al}=2.025 Å., w_{Al}= 0 .922, d_{Ag}=2.045 Å and w_{Ag}=0.877. The mean attenuation length of Al and Ag are the same as before in the case of Al(001).

Supplement

Zr on Al(110) surfaces

Prior to the Ag experiments on Al(110) surfaces, we chose Zr as a candidate material to test the model where we assumed that the relative size of the adatoms correlates with the growth behavior for transition metals on Al surfaces. That is atoms that are smaller than Al atoms tend to form surface alloys and adatoms larger than Al do not displace the substrate Al atoms but instead grow as an overlayer on the surface. An Omicron EFM 3 model UHV evaporator was used to evaporate Zr onto the Al(110) surface. A rod of Zr (diameter 2mm) was used. Evaporation is achieved by electron bombardment heating. The bombarding electron beam induces a temperature rise at the

tip of the evaporant, causing evaporation. All the rest of the experimental set up was the same as before.

In Fig. 7.17 we plot the Al surface peak area as a function of Zr coverage at 0.97 MeV He^+ incident ion energy. Due to the difficulties in evaporating Zr, we could not go above 1.4 ML. However, it is clear that the substrate Al atoms are not displaced by the incoming Zr atoms to form a mixture of Al and Zr as observed in previous chapters. The scatter in the Al surface peak area can be associated more with the background subtraction procedure rather than with the reproducibility of the spectra. These results are in good agreement with our model that a bigger atom like Zr prefers not to displace the Al atoms. LEED patterns also show that the long range order is not disrupted up to the maximum coverage of Zr. The rectangular LEED pattern is sustained throughout the Zr evaporation, indicating that the deposited Zr atoms are in good registry with the substrate. Similar results were observed in the case of Ni films on W(110) surfaces[20]. No significant change in the visible W atoms was observed as a function of Ni coverage up to about 12 ML. Finally Zr XPS intensities did not show any significant shift in their position.

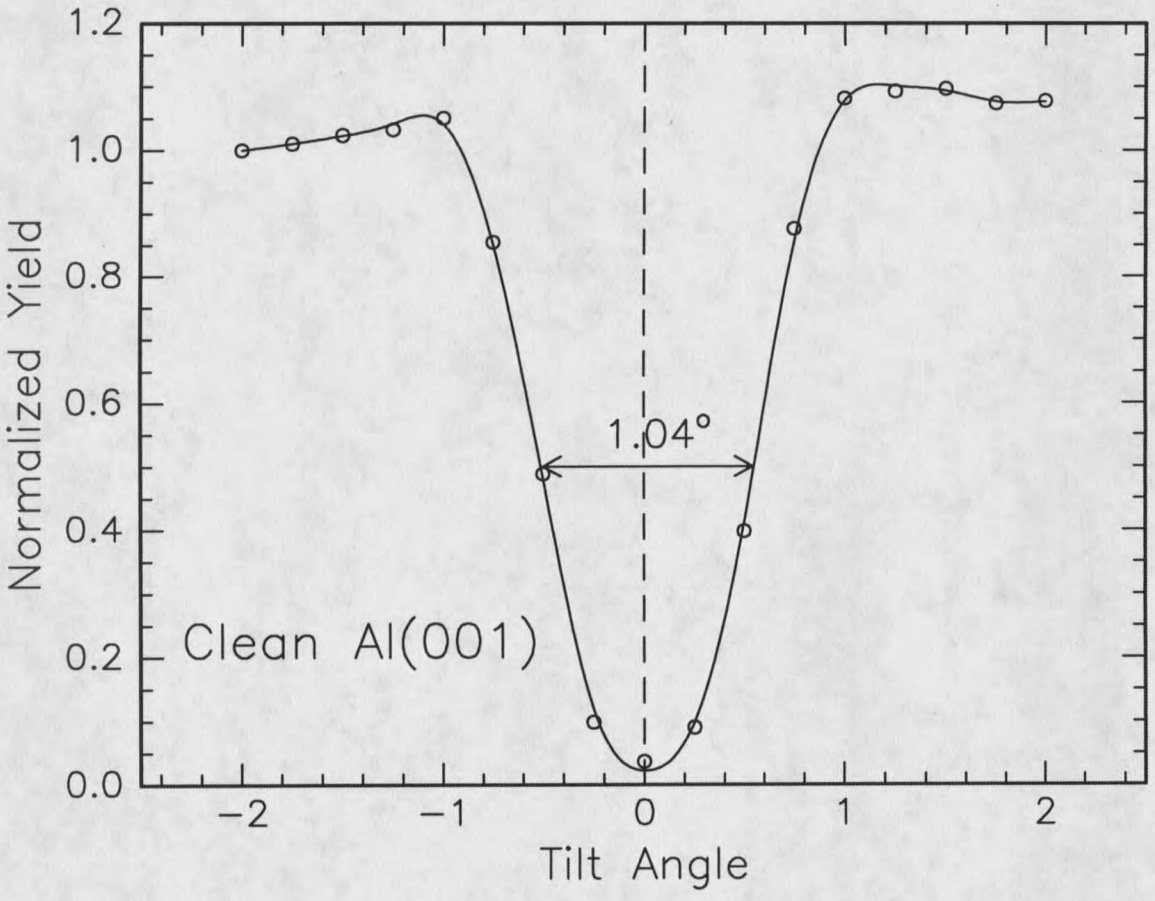

Figure 7.1. A plot of the ratio of the channeled to random RBS yield (angular yield curve) for clean Al(001) as the crystal is tilted relative to the channeling axis.

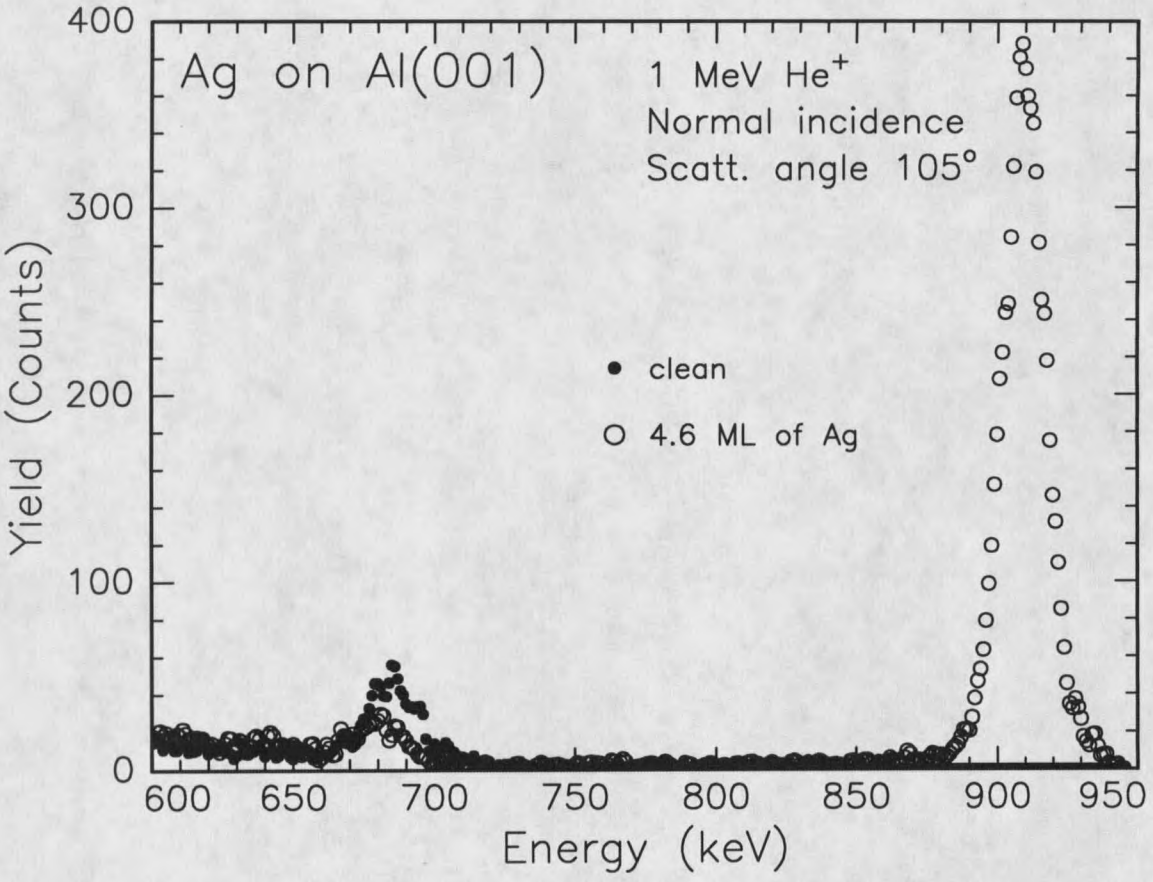

Figure 7.2. Backscattered ion energy spectra for 1 MeV incident He^+ ions on Al(001), clean and with 4.6 ML of Ag.

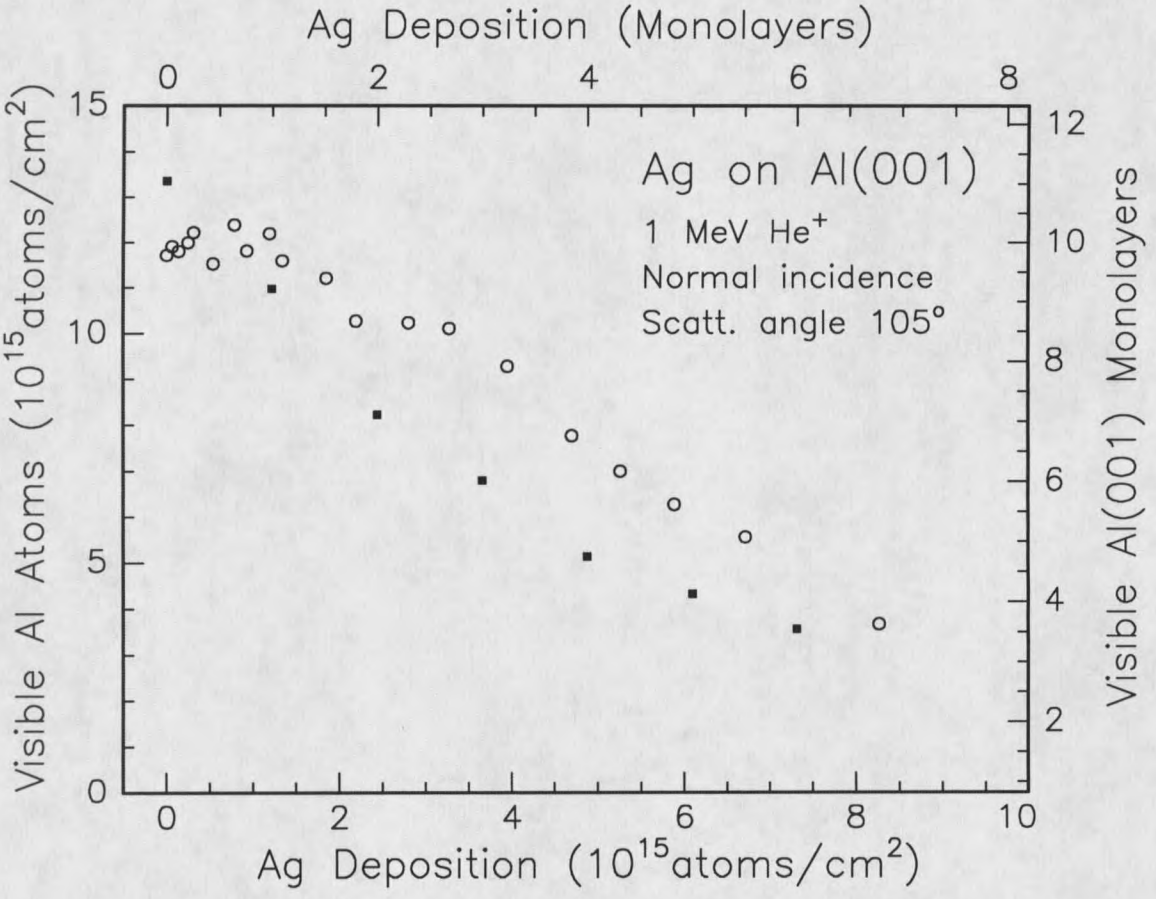

Figure 7.3. Visible Al atoms, at 1 MeV incident ion energy, as a function of Ag coverage deposited at room temperature on the Al(001) surface. The solid squares indicate the expected yield for a layer-by-layer grown Ag film calculated using the VEGAS simulation code.

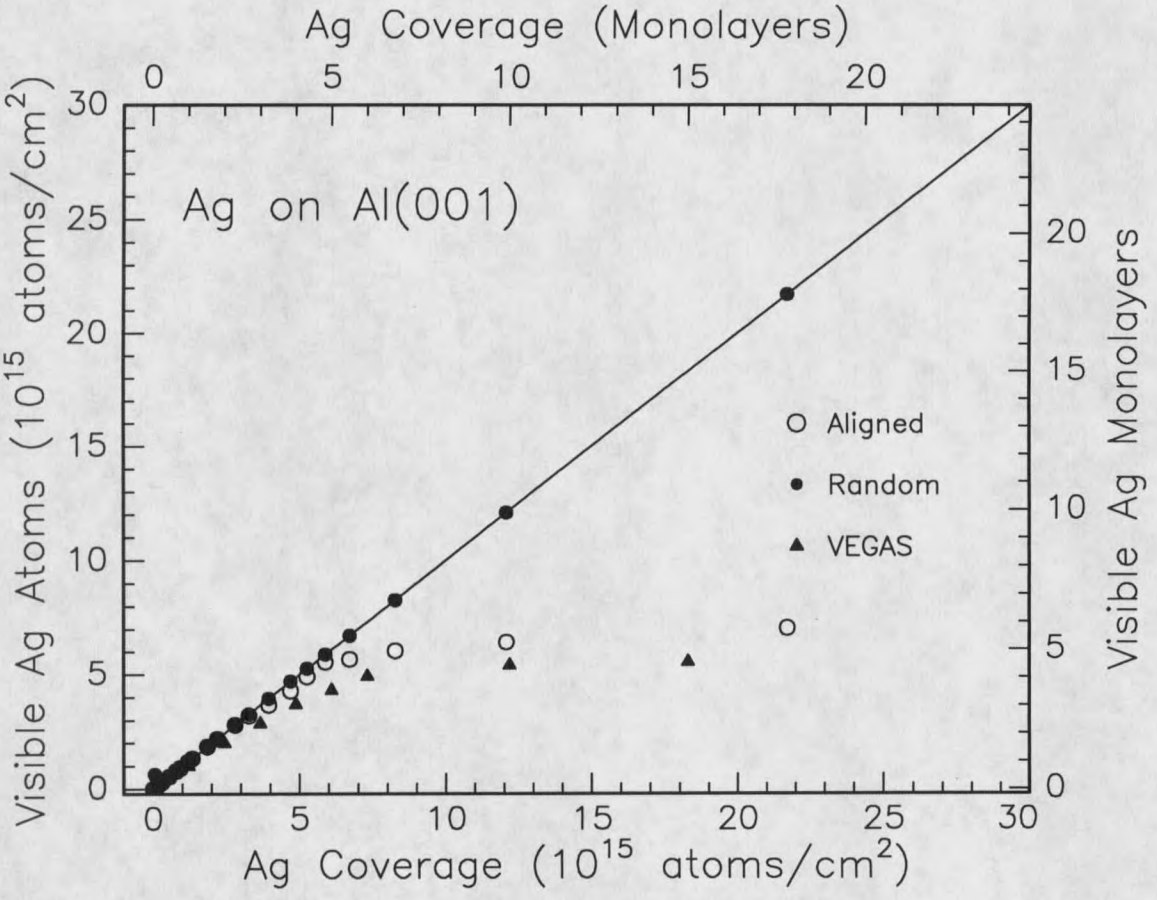

Figure 7.4. Number of Ag atoms visible to the 1 MeV He^+ ion beam as a function of Ag coverage. Solid circles are for a random direction while open circles are for the channeling direction. The solid line is the least-squares fit to the random data. The '▲'s indicate the yield expected for a layer-by-layer growth of a Ag film as calculated using the VEGAS simulation code.

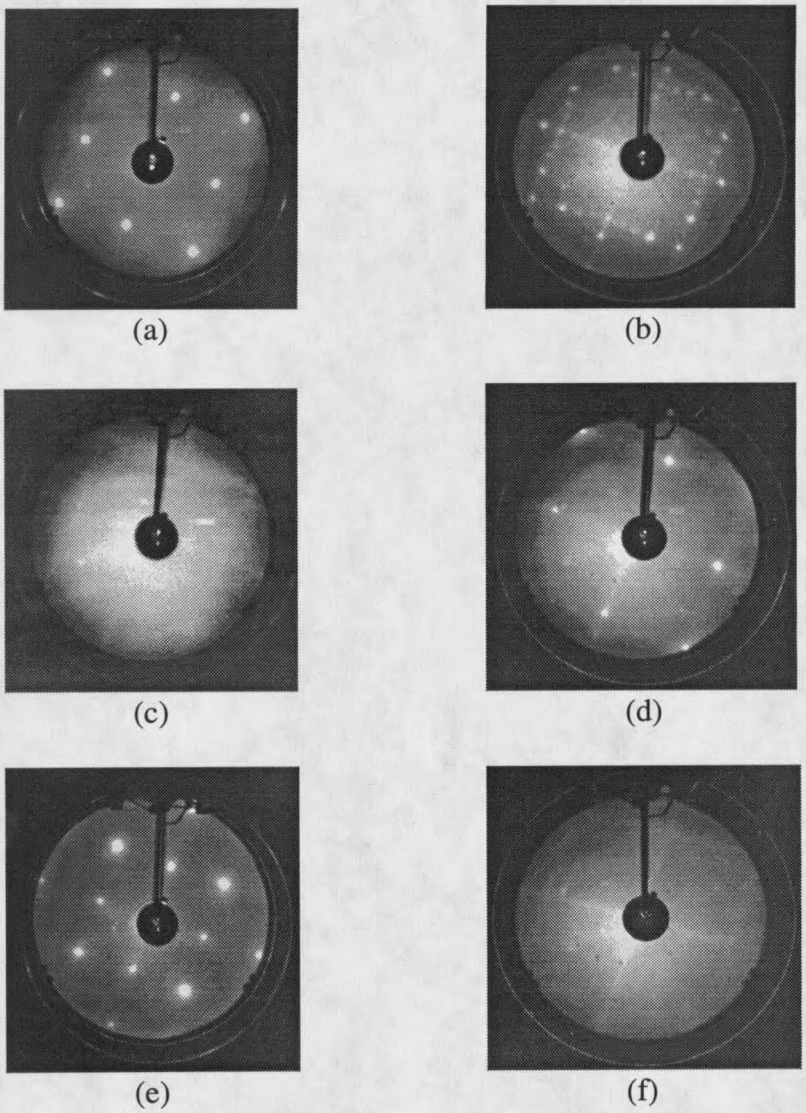

Figure 7.5. LEED patterns observed for Ag on Al(001): (a) clean Al(001) with 51.6 eV incident energy; (b) Ag deposition of 0.5 ML, 51.7 eV; (c) Ag deposition of 2.5 ML, 51.6 eV; (d) Ag deposition of 3.6 ML, 52.1 eV; (e) thick Ag film (30 ML), 55 eV; (f) after annealing at 200°C, 52 eV.

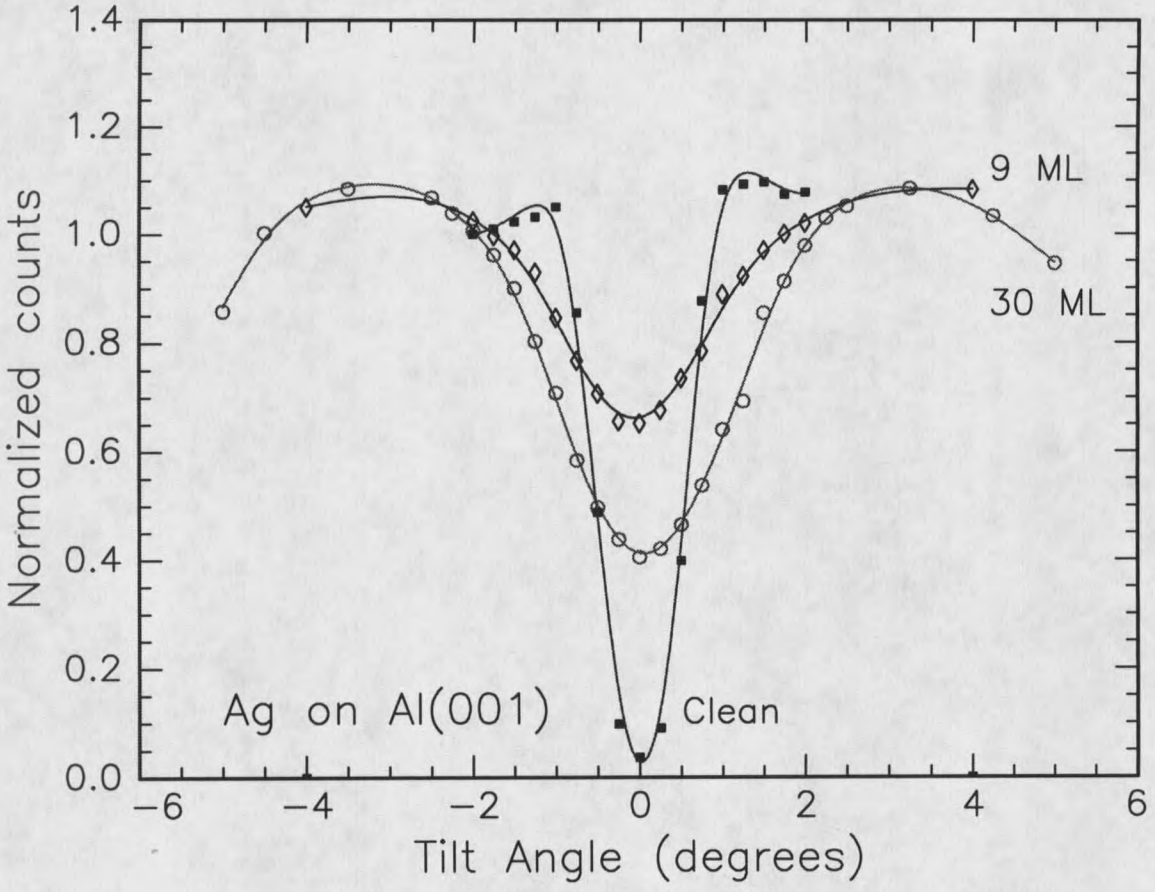

Figure 7.6. The angular yield curves for the 0, 9 and 30 ML of Ag on Al(001) substrate.

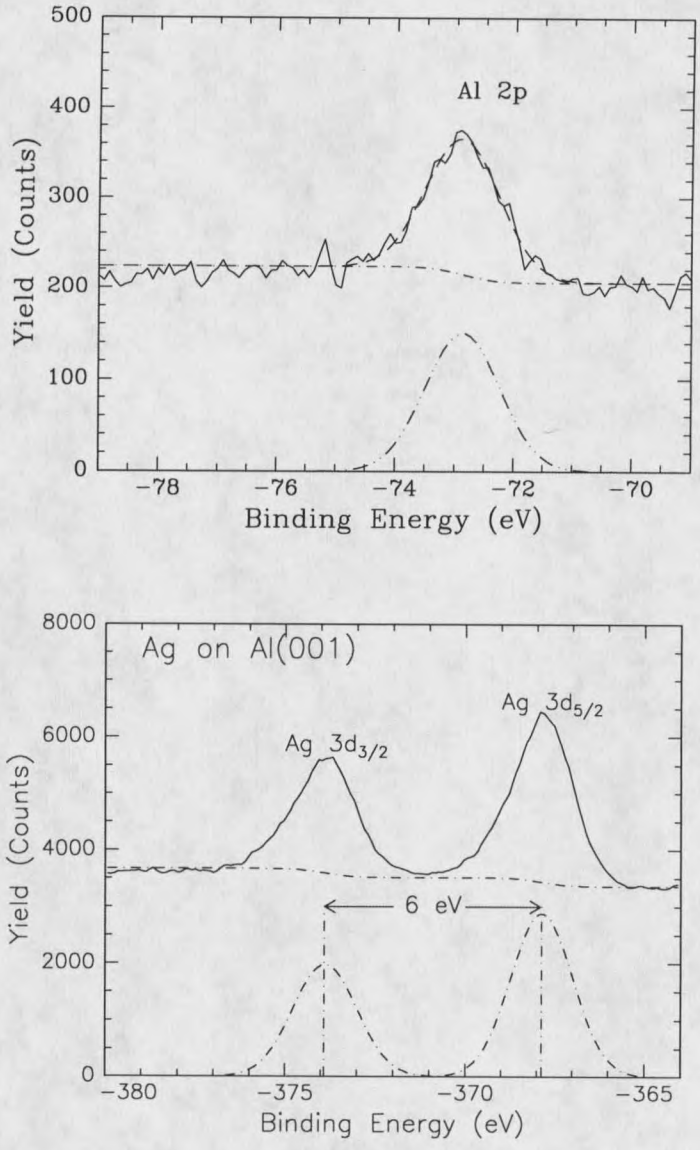

Figure 7.7. Al 2p (a) and Ag 3d (b) X-ray photoemission peaks. The peak in each case is fit to a superposition of a Gaussian component and an error function.

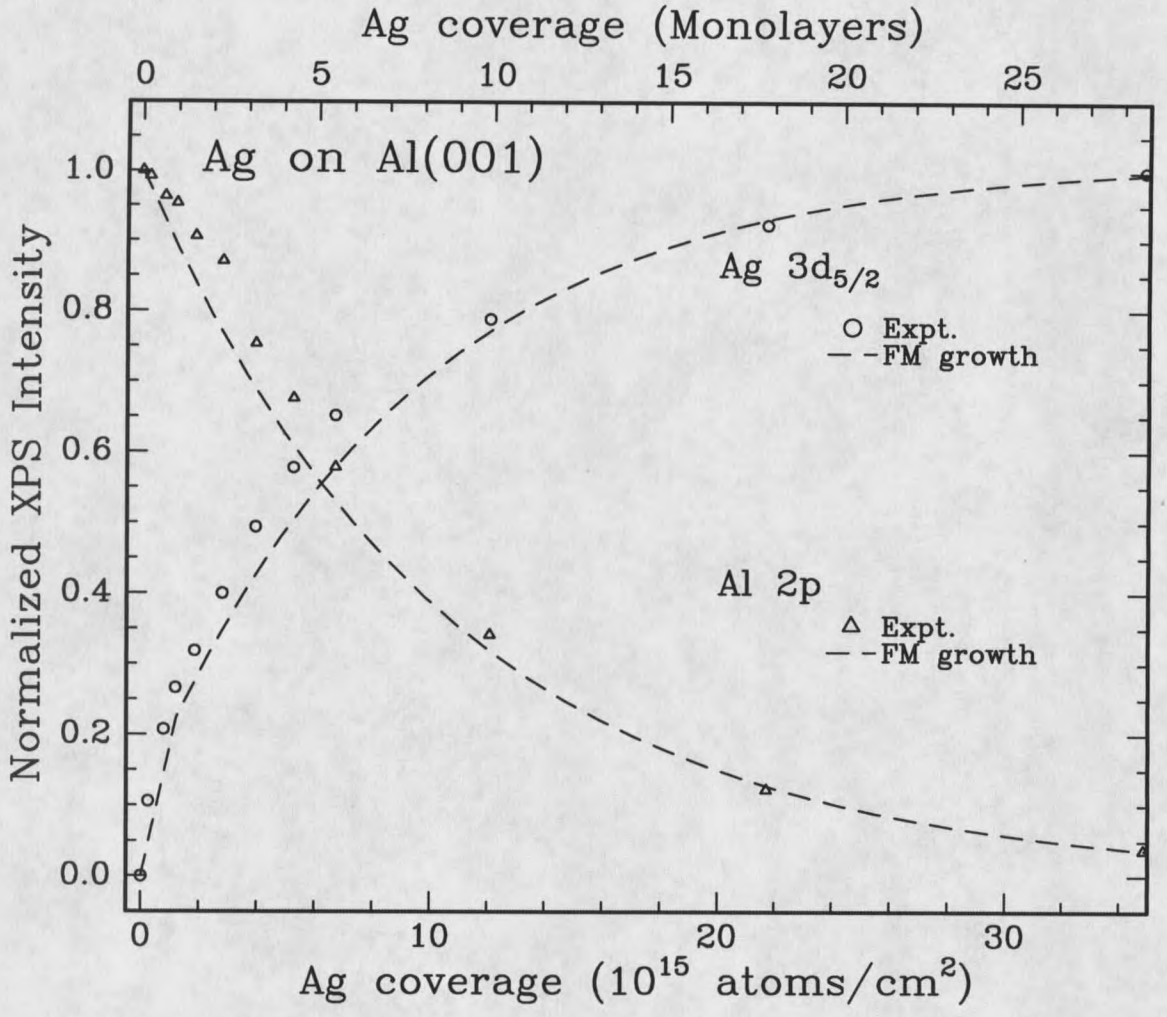

Figure 7.8. Measured Ag $3d_{5/2}$ (open circles) and Al 2p (closed circles) photopeak intensities as a function of Ag coverage. The Ag $3d_{5/2}$ and Al 2p intensity has been normalized to its value at the maximum coverage (30 ML) of the experiment and clean value at the beginning of the experiment respectively. The dotted lines are the calculated emission intensity for the layer-by-layer growth model described in the text.

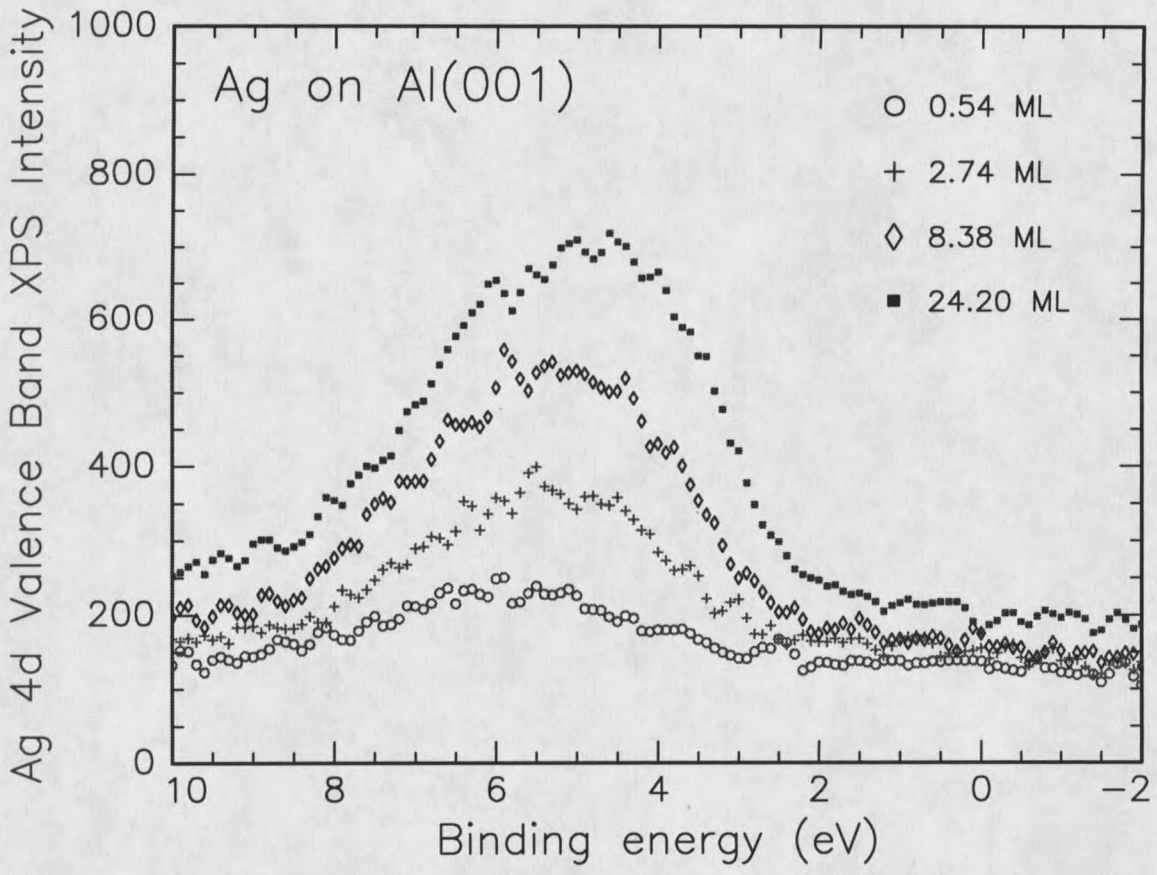

Figure 7.9. Valence band XPS spectra for Ag on Al(001) at the indicated Ag overlayer thicknesses (ML ≡ Ag(001) monolayer equivalent).

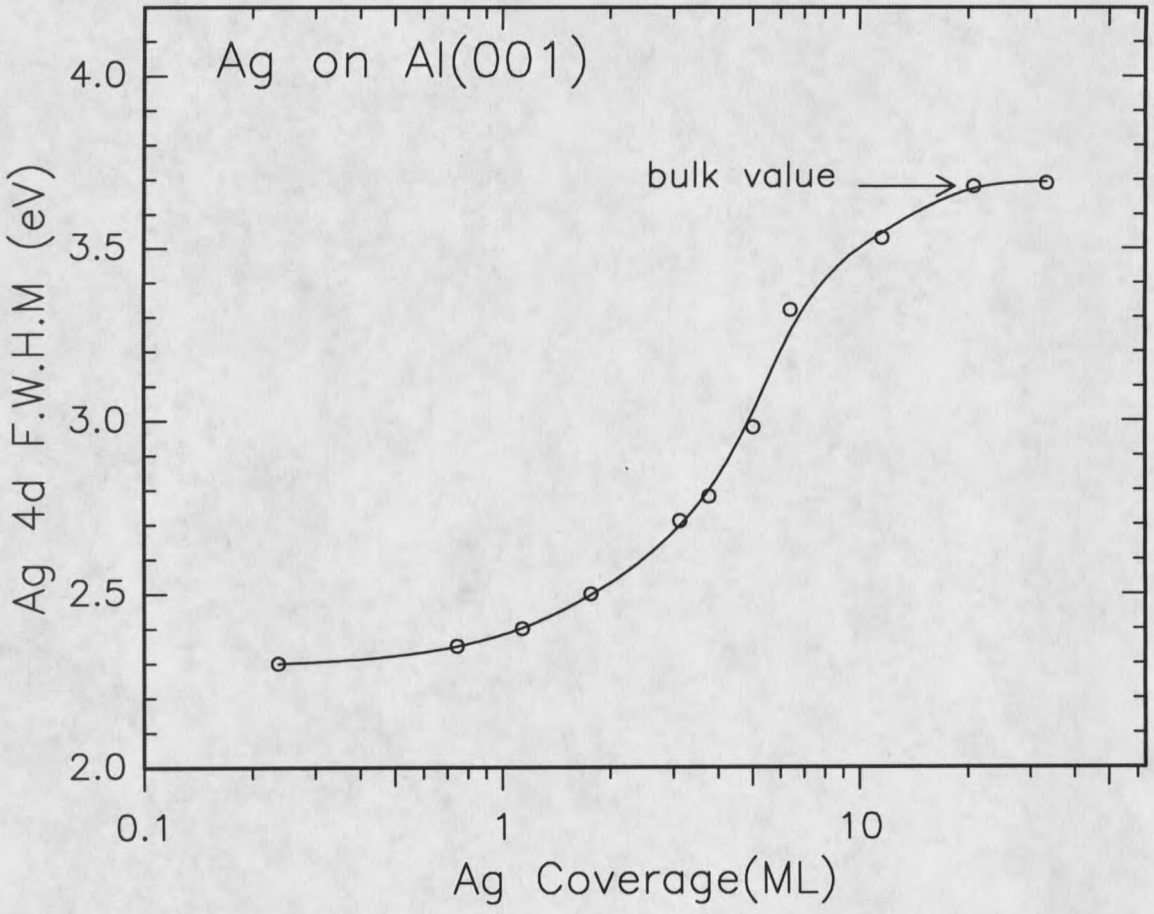

Figure 7.10. A plot of the full width at half maximum (FWHM) of the Ag 4d band versus Ag coverage, taken from data such as Fig 7.9.

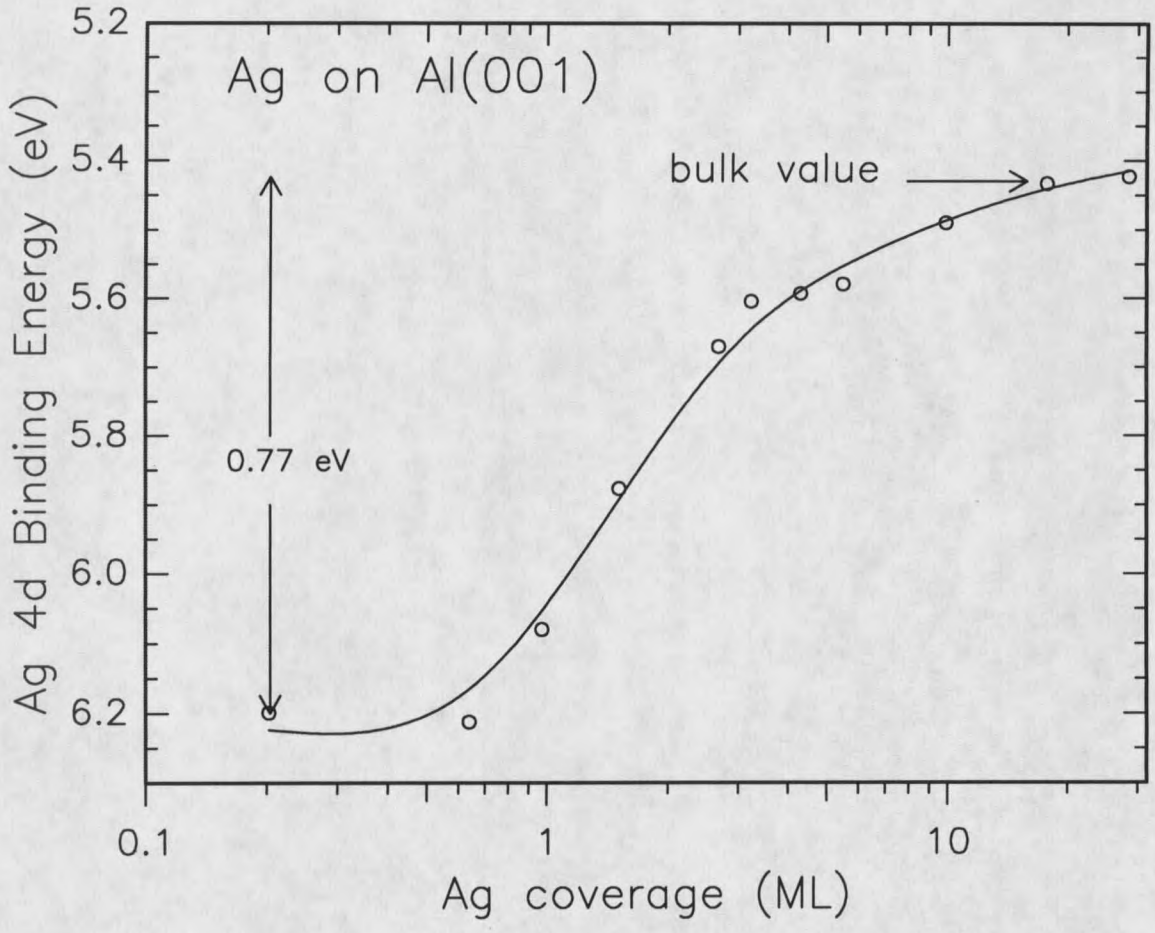

Figure 7.11. A plot of the binding energy of the centroid of the 4d band versus Ag coverage.

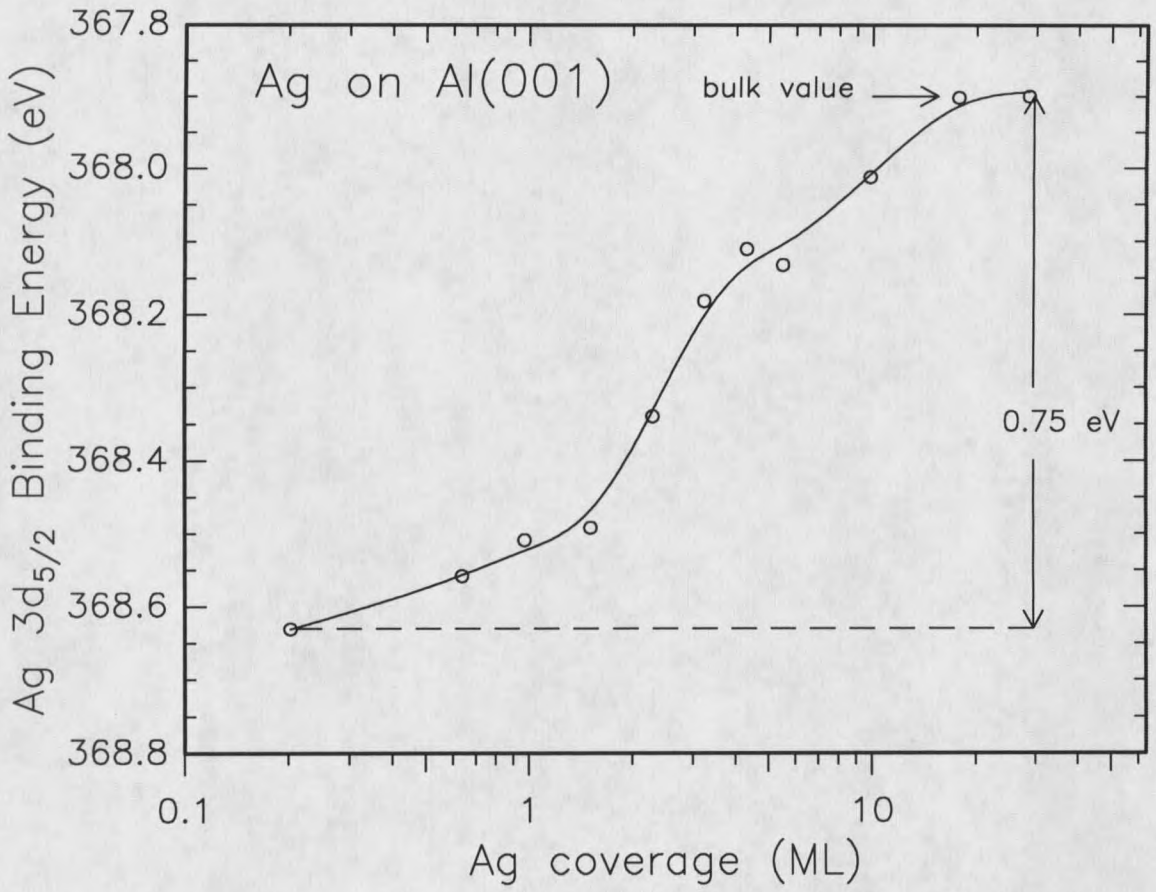

Figure 7.12. A plot of the binding energy of the $3d_{5/2}$ level versus Ag coverage.

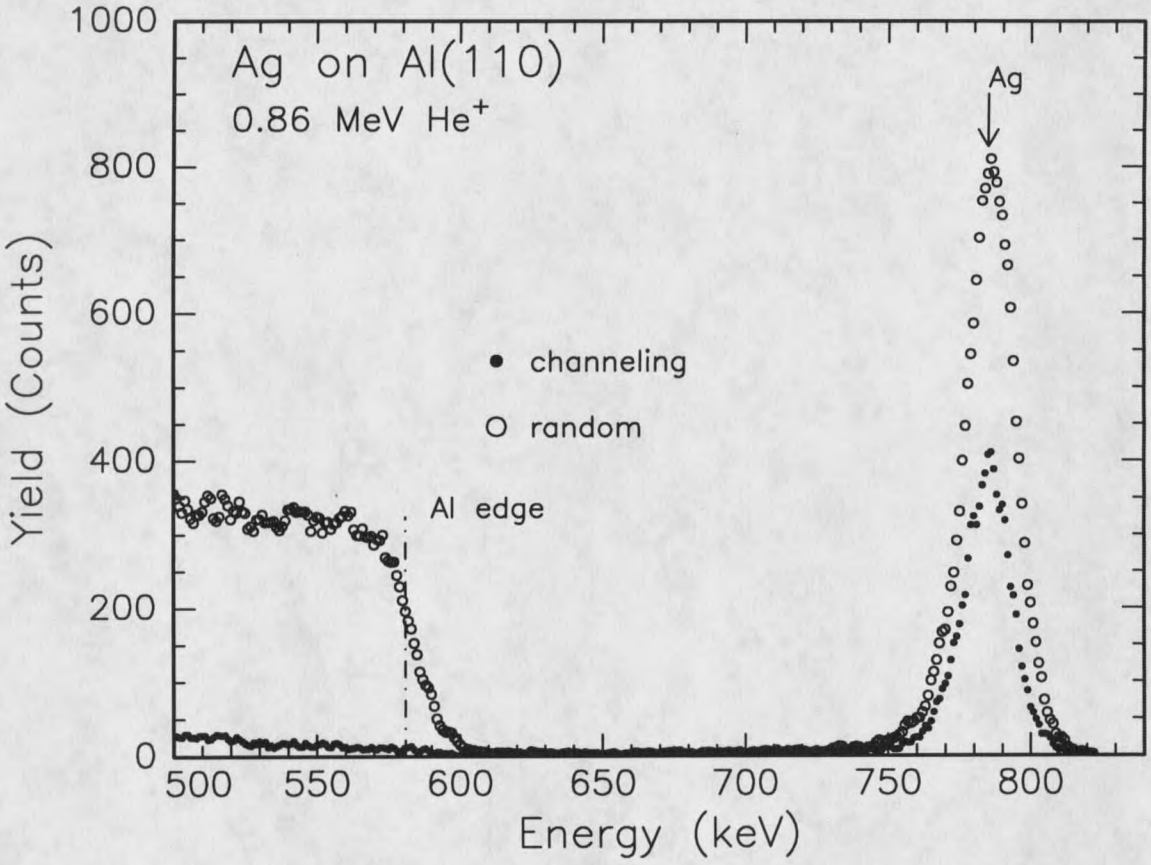

Figure 7.13. He^+ ion scattering spectra at 0.86 MeV incident ion energy after the deposition of 13 ML of Ag on the Al(110) surface. The open circles represent the spectrum taken at random incidence while the closed circles represent that for incidence along the [110] direction. The shadowing effect can easily be seen in this figure.

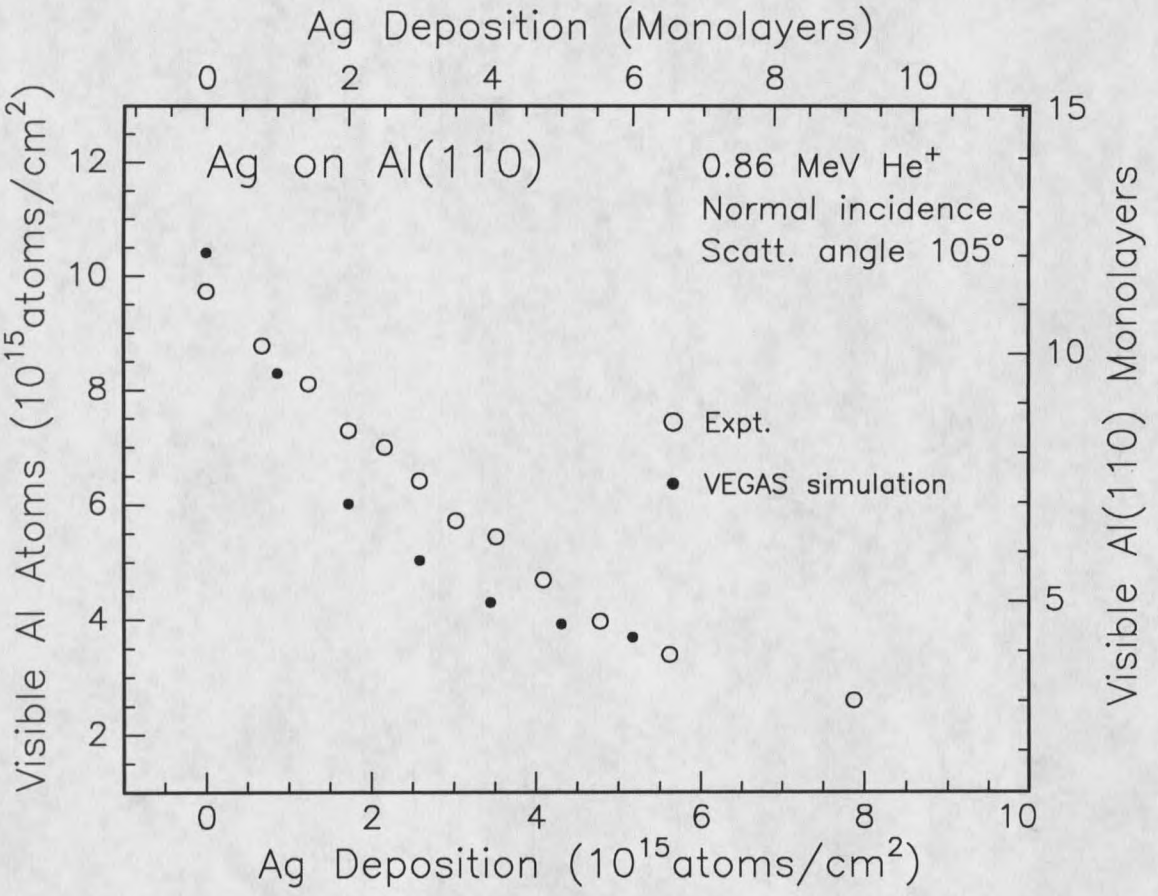

Figure 7.14. Visible Al atoms (open circles), at 0.86 MeV incident ion energy, as a function of Ag coverage deposited at room temperature on Al(110). The closed circles indicate the expected yield for a layer-by-layer Ag film as calculated using the VEGAS simulation code.

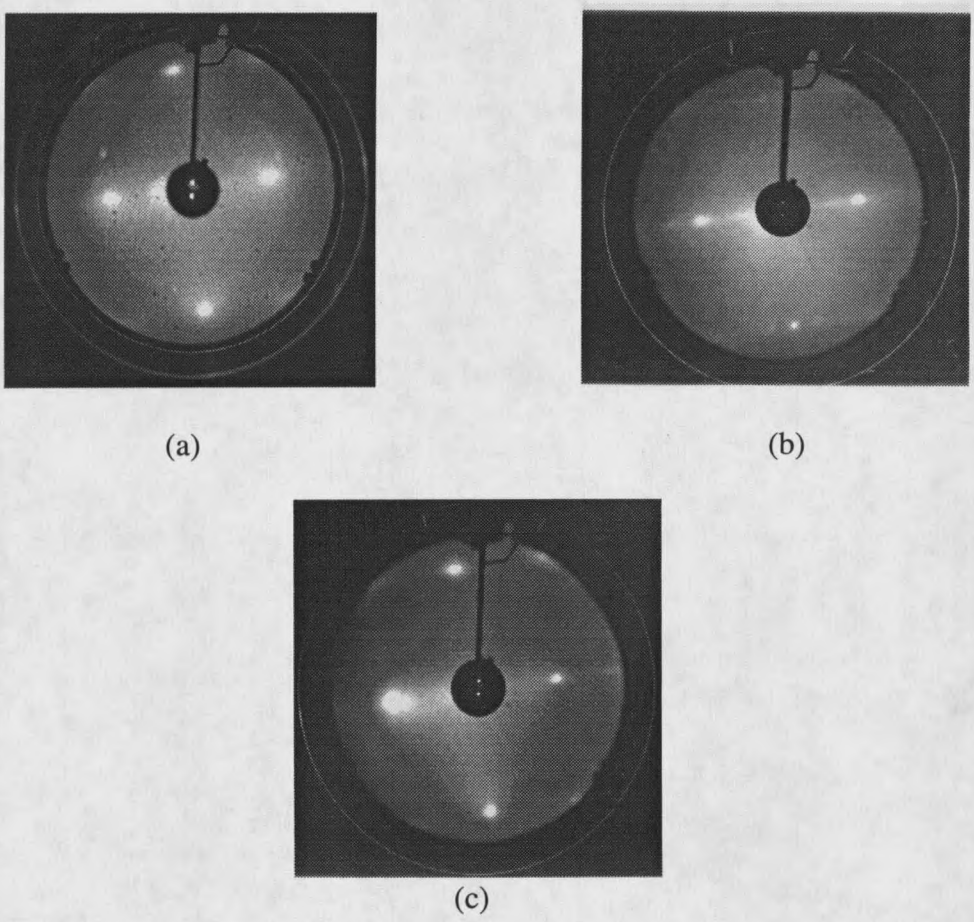

Figure 7.15. LEED patterns for Ag on Al(110). The patterns are for (a) clean and for Ag coverages of (b) 4.6 ML and (c) 25 ML.

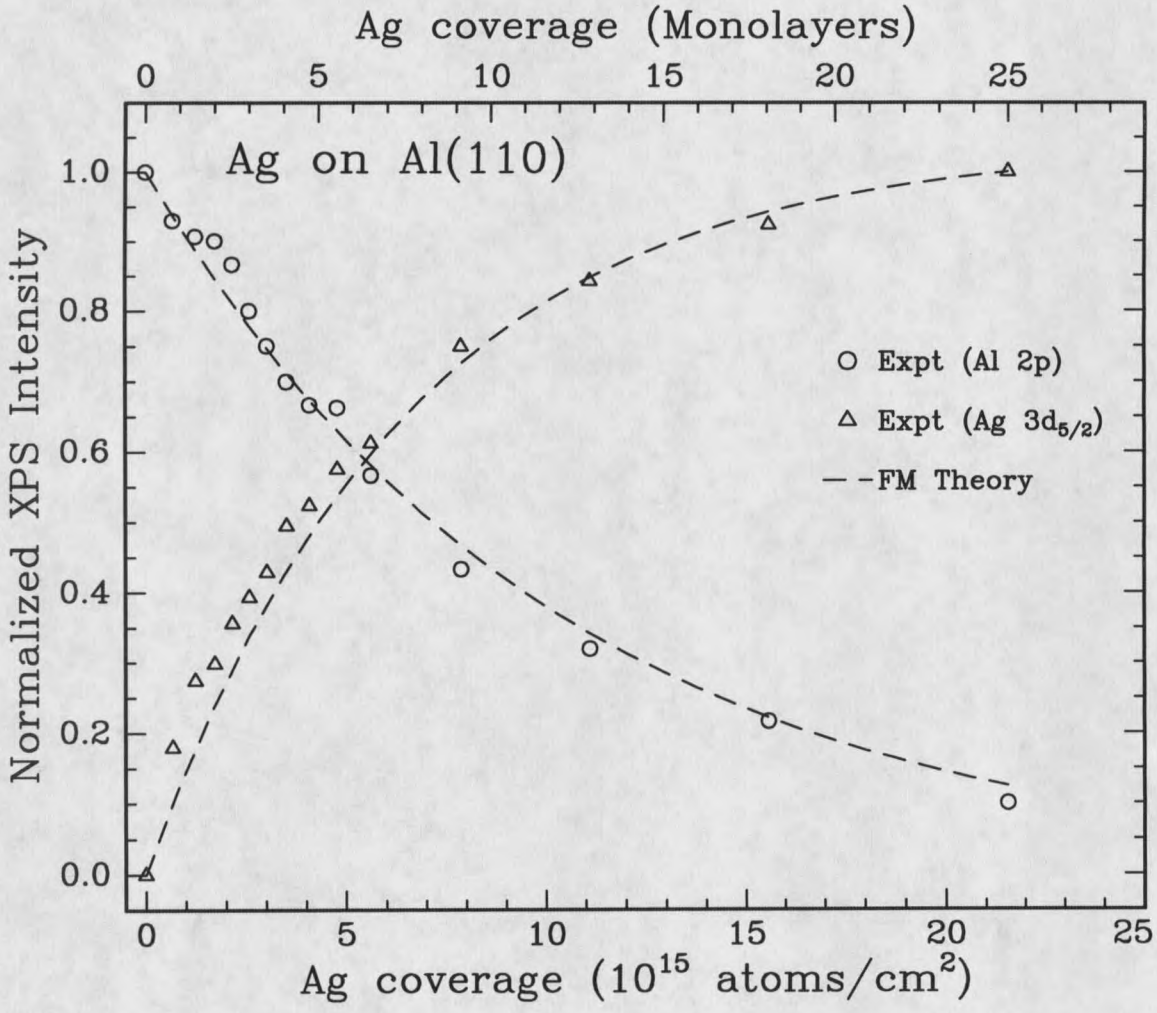

Figure 7.16. Measured Al 2p (open circles) and Ag $3d_{5/2}$ (open triangles) XPS intensities as a function of Ag coverage. The dashed lines were calculated using layer-by-layer growth model discussed in the text.

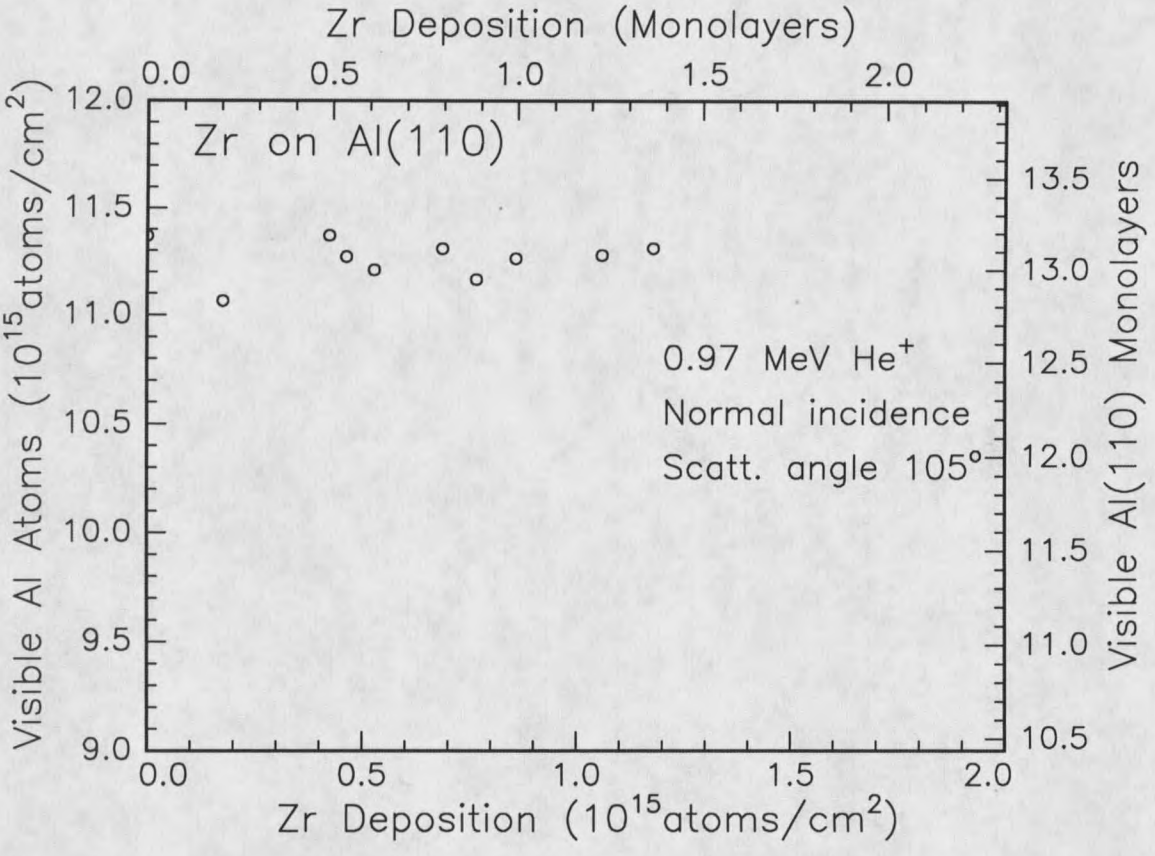

Fig. 7.17. Measured ion scattering yield from Al atoms as a function of Zr coverage on the Al(110) surface using a normally incident 0.97 MeV He^+ ion beam.

REFERENCES

1. Barry C. Bolding and E.A. Carter, Phys. Rev. 44 (1991) 3251.
2. R. J. Smith, Adli A. Saleh, V.Shutthanandan, N. R. Shivaparan and V. Krasemann, Mat. Res. Soc. Symp. Proc. Vol. 399, Materials Research Society.
3. B. Frick and K. Jacobi, Surf. Sci. 178, (1986) 907.
4. W. F. Egelhoff, Jr., Surf. Sci. 11/12, (1982) 761.
5. W. F. Egelhoff, Jr., J. Vac. Sci. Tech. 20, (1982) 668.
6. M. Hancbuchi, T. Katoh and K. Monta, Appl. Surf. Sci. 89, (1995) 113.
7. D. S Gemmel, Rev. Mod. Phys. 46, (1974) 129.
8. J. W. Frenken, R. M. Tromp and J. F. van der Veen, Nucl. Instr. Meth. In Phys. Res. B17, 334(1986).
9. Ti on Al(001) paper.
10. C. D. Wagner, W. M. Riggs, L. E. Davis, J. F. Moulder and G. E. Muilenberg, *Handbook of X-ray Photoemission Spectroscopy* (Perkin-Elmer Corporation, Eden Prairie, 1979).
11. M. P. Seah and W. A. Dench, Sur. Anal. 1, 2 (1979).
12. S. Ossicini, R. Memeo and F. Ciccacci, J. Vac. Sci. Technol. A3, 387 (1985).
13. A. McKinley, R. H. Williams and A. W. Parke, J. Phys. C12 (1979) 2447.
14. P. Steiner and S. Hufner, Solid State Commun. **37** (1981) 279.

15. L. Abbati, L. Braicovich, A. Fasana, C. M. Bertoni, F. Manghi and C. Calandra, Phys. Rev. B23 (1981) 6448.

16. H. Roulet, J. M. Marriot, G. Dufour and C. F. Hague, J. Phys. F10, (1980) 1025.

17. W. E. Egelhoff, Jr. And C. G. Tibbetts, Solid State Commun. 29 (1979) 53.

18. See, for example, J. W. Matthews, Ed. *Epitaxial Growth* (Academic Press, New York 1975).

19. Adli A. Saleh, V. Shutthanandan and R. J. Smith, Phys. Rev. B49 (1994) 4908.

20. Xu Mingde and R. J. Smith, J. Vac. Sci. Tech., 9, (1991) 1828.

DISCUSSION

The chemical and physical changes are particularly interesting for systems in which a late transition metal is deposited on an aluminum single crystal surface. It is very important to find out whether the effects are due to charge-transfer-induced changes in the nature of the adlayer or whether the effects are simply the result of lattice strain and phase transitions within the thin film. Considerable uncertainty also exists as to the mode of film growth, especially on different orientations of the substrate surfaces. In this thesis work, we have investigated the growth of Pd, Fe, Co and Ag films on Al(001) and Al(110) surfaces. The results are summarized in Table 2.

Table 2

Metal	Al(001) surface	Al(110) surface
Ti[1]	Epitaxial	Epitaxial
Ni[2]	Mixing	Mixing up to 8ML
Pd	Mixing up to 5 ML	Mixing up to 10 ML
Fe	Mixing up to 5 ML	Mixing up to 9 ML
Co	Mixing up to 3 ML	Mixing up to 5 ML
Ag	Epitaxial	Epitaxial

The results of Chapters 4, 5, 6 and 7 suggest that Pd, Fe and Co deposition on Al surfaces leads to surface alloy formation, while Ag deposition results in the formation of an

epitaxial Ag overlayer. In order to understand the growth mode of these metal films on Al single crystal surfaces, let us focus on properties of the different TM-Al compounds which might explain the tendency to surface alloy formation or overlayer formation. The parameters which we have considered for this purpose are: the surface free energies, formation energies, lattice mismatch, atomic sizes and the crystal structures of the alloys.

We first note that the surface energies of the transition metals[3] under investigation here range from 2.05 to 2.50 J/m^2 while that for Al is 1.1 J/m^2. Thus we expect that none of the transition metals should wet the Al surface. Rather, there will be a tendency toward island formation or alloy formation depending on other factors. Some of the other factors which we have considered are listed in Table 3.

Table 3

Element	γ_S (J/m^2)	lattice mismatch	H_{for} (kJ/mol)	a_{nn} (Å)*	Strain	Strain Energy.(kJ/mol)
Al	1.10	----	----	2.48	----	----
Pd	2.05	-4%	-184	2.63	6%	41.7
Ni	2.45	-15%	-118	2.50	1%	0.6
Co	2.55	-12%	-108	2.48	0%	0
Ti	2.10	+3%	-76	2.85	13%	448
Fe	2.48	+0.1%	-50	2.52	2%	3.2
Ag♦	1.25	+1	0	2.89	14%	>400

* For Al, the entry is half the distance along the [112] direction, that is, the location where the TM atom would be placed to form the (110) plane of the TM-aluminide.

◊ In the Ag-Al phase diagram, AgAl compound does not exist. Therefore we used pure Ag metal for analysis.

As we discussed in Chapter 1, epitaxial growth requires a good lattice match between the overlayer and the substrate. But all the metals in Table 2 have smaller than 15% lattice mismatch (column 3) and did not grow epitaxially except Ti and Ag. Furthermore, in the case of Fe even though the lattice match was almost perfect, a mixing was observed between the Fe atoms and Al substrate. The heat of formation per TM-Al pair is given in the fourth column of the Table 2[3]. Since all of these values are negative except Ag, formation of the alloy is energetically favorable, although kinetic factors may limit alloy formation at room temperature. We note that PdAl has the most negative formation energy while FeAl has the smallest. If heat of formation was the deciding factor for alloy formation, the observation of epitaxial growth for Ti on Al[1] would suggest that Fe might also grow as an overlayer, contrary to our results. Also the lattice matching between Fe and Al is nearly perfect as we discussed in Chapter 5. Therefore it appears that neither the aluminide formation energy, nor the lattice mismatch alone serve as reliable parameters to predict epitaxial growth. Hence we looked at the atomic size of the TM's and noted that of the six metals studied, only Ti and Ag have an atomic radius that exceeds that for Al[3]. This led us to consider models based on surface strain. An examination of the simplest crystal structures of the transition metal aluminides provides

the equilibrium values for the TM-Al nearest neighbor distance listed in column five of Table 2. The elements Pd, Ni, Fe and Co all form a CsCl structure with the formation energies listed in Table 2[4]. The (110) planes of these aluminides have a relatively small lattice mismatch with the Al(110) plane, and are replicated with small lattice strain simply by placing a TM atom at the hollow site in the Al(110) plane, directly above a second layer Al atom, and coplanar with the surface Al atoms. At this location the TM atom would be 2.48 Å from the four nearest Al atoms in the (110) plane. The associated strains imposed by forcing registry with the unreconstructed Al substrate, relative to the equilibrium spacings of the aluminide, are given in column six of Table 2, and range from about 6% for PdAl to zero for CoAl. On the other hand, the structure of TiAl is face-centered tetragonal, with alternating (001) planes of Ti and Al. The Ti-Al interatomic distance is considerably larger than that for the other metals. The (110) plane of TiAl also has a very small lattice mismatch with the Al(110), only 3%, but the Ti atoms in the equilibrium structure are about 1.4 Å above the hollow site of the surface Al(110) plane. Thus, to move the Ti atom down into the surface leads to a surface strain of about 13% when the Ti and Al atoms are co-planar. We believe that the large strain associated with Ti indiffusion prevents mixing at room temperature and leads to overlayer formation. This model was tested successfully using Ag and Zr atoms deposited on Al surfaces as discussed in detail in Chapter 7. The last column in Table II shows the values of the strain energies for each TM-Al pair relative to the minimum energy at the equilibrium spacing calculated using the following model[6].

The model used is essentially a band-energy model constructed using the cohesive energies of the metals distributed over the number of nearest neighbors for each atom. In this model an average of the cohesive energies of Al and the transition metal are used to estimate the energy per TM-Al bond. A Lennard-Jones (6-12) potential is used to calculate the strain energy, using the estimated bond energy and the departure from the equilibrium spacing[7]. From these data we see that the negative formation energies are more than sufficient to offset the small amount of strain energy for Pd, Ni, Fe and Co. However, the energy to move a Ti atom through the Al(110) plane is much larger than any of the other cases considered here. We believe that these considerations completely explain our observations on the Al(110) surface.

The results on the Al(001) surface are not trivial to understand and to explain by just using a single model. Ti[1] and Ag (Chapter 7) behaved in a similar fashion up to about 5 ML of coverage. The behavior of deposited atoms in the first monolayer regime was not very clear in both cases as discussed in Ref. 2 and Chapter 7. But just as we predicted in the case for the Al(110) surface, both Ti and Ag atoms do eventually grow epitaxially on the Al(001) surface. The case of Ni on Al(001)[3] is especially interesting. The results up to about 5 ML of Ni coverage were interpreted as indicating a Ni film in a metastable *body-centered-cubic* structure in a Stranski-Krastanov (SK) mode. After 5 ML of coverage, the *bcc* islands coalesce to cover the surface. The other metals Pd, Fe and Co, seem to behave the same way on both the Al(001) surface and the Al(110) surface, but the mixing of the deposited atoms and the substrate Al atoms stop at lower

metal coverages, as shown in Table 1. This can be attributed to the fact that the Al(110) surface is relatively open as compared to the Al(001) surface, and has the largest surface energy among the three low-index surfaces of Al. Finally, the bond energy model using the surface strain associated with aluminide formation for the Al(110) surface may be sufficient to predict the growth behavior of transition metals on Al(001) surfaces, but further analyses is required. Additional experiments to further characterize the structure of the initial monolayer may also be useful.

As a final point, it is important to continue the experiments on Al(111) surfaces to look at the behavior of these thin metal films, since the results obtained from these experiments can give us more insight into the growth modes observed in the cases that we studied in this thesis.

REFERENCES

1. Adli A. Saleh, Ph. D Thesis, Montana State University, 1994.
2. V. Shutthanandan, Ph. D Thesis, Montana State University, 1994.
3. Cohesion in Metals: Transition Metal Alloys, F. R. De Boer, R. Boom, W. C. M. Mattens, A. R. Miedema and A. K. Niessen (North-Holland, Amsterdam, 1988).
4. C. Kittel, Introduction to Solid State (Wiley, New York, 1968).
5. M. Hansen, Constitution of Binary Alloys, edited by K. Anderko (McGraw-Hill, new York, 1958).
6. R. J. Smith, N.R.Shivaparan, V. Krasemann, V. Shutthanandan and Adli A.Saleh, Mat. Res. Soc. Symp. Proc. Vol 399, 1996.
7. A. D. van Langeveld and V. Ponec, Appl. Surf. Sci. 16, (1983) 405.

APPENDIX

XPS CURVE FITTING

In XPS, when one element is present in different chemical states or two or more peaks are very close to each other, it is necessary to resolve XPS peaks into different components by means of a non-linear least-squares method. In order to perform these fits, first we should know the exact line shapes of these peaks. The measured line shape of a core-level photopeak is a complex function, and can be represented in terms of a convolution of the natural line shape and the instrument response function[1].

The natural line shape is usually expressed as a Lorentzian shape, and it is given by

$$L(E) = \frac{1}{1 + 4\left(\frac{E - E_L}{W_L}\right)^2}$$

where E is the electron energy, E_L is the centroid, and W_L is the FWHM.

The instrument response function can be represented by a Gaussian shape, and it is given by

$$G(E) = \exp\left(-4\ln(2)\left[\frac{E - E_G}{W_G}\right]^2\right)$$

where E_G is the centroid, and W_G is the FWHM.

Thus, the function we must give the computer to represent our core-level line shape is

$$I(E_G) = \int_{-4\sigma}^{+4\sigma} G(E)L(E)dE_G$$

We have to perform this calculation at each data point for each iteration of the minimization routine.

However, in metals, creation of long-lived low energy electron-hole pairs near EF leads to a skewing of the symmetric line shape towards the low kinetic energy side. Doniach and Sunjic show that the natural line shape of metals can be represented by the following expression[2]

$$L(E) = \frac{\cos\left(\frac{\alpha\pi}{2} + (1-\alpha)\tan^{-1}\left[2\frac{E-E_L}{W_L}\right]\right)}{\left[(E-E_L)^2 + 4W_L^2\right]^{\frac{1-\alpha}{2}}}$$

where α is the asymmetry parameters.

A typical XPS spectrum will have a background which arises from those photoelectrons that have lost energy when traveling through the solid. Thus, some form of background function has to be included in our fitting routine. Shirley[3] proposed that the increased background be correlated with the peak area. The inelastic scattering energy distribution at kinetic energy E_k is proportional to the number of electrons having energy higher than E_k. We have used this background subtraction method in our fitting routine. In most cases, we have used a Lorentzian line shape and a Shirley background, except in the Pd case (Chapter 4) we used a Gaussian line shape.

REFERENCES

1. J. J. Joyce, M. Del Giudice and J. H. Weaver, J. Elec. Spec. Phe., 49 (1989) 32.

2. G. Mattogno and G. Rigini, Surf. Inter. Anal., 17 (1991) 689.

3. M. Goleotti et. al, Surf. Sci., 297 (1993) 202.